UNIVERSITY OF SOUTHAMPTON

FACULTY OF NATURAL AND ENVIRONMENTAL SCIENCES

School Of Chemistry

Volume One of One

Transition Metal Nitride Materials
For Supercapacitor Applications

by

Benjamin Matthew Gray

Thesis for the degree of Doctor of Philosophy

July 2015

UNIVERSITY OF SOUTHAMPTON

ABSTRACT.

FACULTY OF NATURAL AND ENVIRONMENTAL SCIENCES

Chemistry

Thesis for the degree of Doctor of Philosophy

TRANSITION METAL NITRIDES FOR SUPERCAPACITOR APPLICATIONS

Benjamin Matthew Gray

There is a pressing need to develop more environmentally friendly ways to generate and store electrical energy. Current technology for this is limited by the speed at which power storage can absorb and store the energy generated. To this end, transition metal nitride materials have been investigated with the aim of creating a nitride based supercapacitor.

$Ti(NEt_2)_4$ and $V(NEt_2)_4$ were prepared and there, and $Ta(NMe_2)_5$'s, sol-gel chemistry was explored. These sols were infiltrated into multilayer templates, composed of hexagonally close packed opalescent crystals of DVB crosslinked amidine capped polystyrene spheres and heated under flowing ammonia to give metal nitride inverse opals exhibiting long range order and specific capacitances of upto 2 F g^{-1}. Solid (Ti,V)N solutions were also synthesised and tested electrochemically as supercapacitor electrode materials.

TiN and VN foils were prepared and subjected to a range of surface treatments. Their specific capacitances at a range of scan rates were measured to ascertain which surface treatment gave the highest capacitive performance.

Table of contents.

List of tables.

List of figures.

DECLARATION OF AUTHORSHIP.

I, ...

declare that this thesis and the work presented in it are my own and has been generated by me as the result of my own original research.

Transition Metal Nitrides for Supercapacitor Applications

I confirm that:

1. This work was done wholly or mainly while in candidature for a research degree at this University;
2. Where any part of this thesis has previously been submitted for a degree or any other qualification at this University or any other institution, this has been clearly stated;
3. Where I have consulted the published work of others, this is always clearly attributed;
4. Where I have quoted from the work of others, the source is always given. With the exception of such quotations, this thesis is entirely my own work;
5. I have acknowledged all main sources of help;
6. Where the thesis is based on work done by myself jointly with others, I have made clear exactly what was done by others and what I have contributed myself;
7. Parts of this work have been published as: [please list references below]:

Templated Non-Oxide Sol-Gel Preparation of Well-Ordered Macroporous (inverse opal) Ta_3N_5 Films. . *Inorg. Chem.*, 2013, 52 (17), pp 9994-9999

Signed:.....

Date:.....

Acknowledgements.

Many individuals deserve a huge thank you for aiding me in the completion of this work. From those project students who I had the pleasure of supervising and helping through their undergraduate research projects: Chris Mallinson, Joseph Plumber, John Hunter, Jack Smith, Mike Palmer, Grazvidas Jeglevicius and Graham Hayes. To my lab colleagues who I learnt so much from, be that as an introduction to the world of inert atmosphere chemistry, to doing the ground work for this project all the way to helping me fine tune my ability to offer and receive advice and assistance carefully across language and experience barriers: Shereen Hassan, Baishakhi Mazumder, Imran Shah, Mahboba Hasan, Wafa Al-Arjan, Moritz Foelsing, Calum Robertson, Michael Palmer Alex Madsen and Matt Roberts.

A wide variety of individuals have aided my analysis of a variety of samples, being instrumental in allowing me access to the instruments necessary for the work and helping me to analyse the data obtained from them. Daniel Law from NCESS, Marek Jura from ISIS, Chris Spindlow from RAL, William Levason, Neil Wells, John Langley, Julie Herniman, Chris Baker, John Owen, David Pugh and Wenjian Zhang from the University of Southampton and Edward Milton from Advanced Chemistry Development.

Two individuals deserve special thanks for being instrumental in me finishing this work, for stepping in to tie up loose ends when I was no longer physically able to. Without these individuals' time and commitment this project would have been left at the 99% mark, Tom 'Spud' Hitch and Xianji 'Lee' Li.

The last and most important thank you should go to my Supervisor, without whom a nervous third year undergraduate would never have developed an interest in metal nitrides and sol-gel chemistry, and never pursued a PhD project in the area. This gentleman has inspired me with his patience and reassurance for many long years, through the toughest scenario anybody ever has to face and is still willing to help me write a thesis. Andrew Hector, this project would not have been possible without you and for giving me the opportunity to do this I am truly grateful. You have set the bar for any future supervisors almost unobtainably high. Long may you continue to be such a fantastic role model and mentor to those who have the good fortune to follow in my footsteps…just perhaps not too closely in them.

Definitions and abbreviations.

Abbreviation	Meaning
THF	Tetrahydrofuran
IPA	Isopropyl alcohol, propan-2-ol
PS	Polystyrene
IR	Infra-red spectroscopy
NMR	Nuclear magnetic resonance spectroscopy
XRD	X-ray diffraction spectrometry
PXD	Powder X-ray diffraction spectrometry
MN	Metal nitride
TMN	Transition metal nitride
CVD	Chemical vapour deposition
ALD	Atomic layer deposition
Me	Methyl
Et	Ethyl
iPr	Iso-propyl
Pr	Propyl
EDX	Energy dispersive X-ray analysis
XPS	X ray photoelectron spectroscopy
DI	Deionised water
MA	Micro analysis
SEI	Secondary electron imaging
VNR	Vanadium amide sols/gels
TiNR	Titanium amide sols/gels
TaNR	Tantalum amide sols/gels
TGA	Thermogravimetric analysis
TDMAT	Tetrakis dimethylamino titanium(IV)
TDEAT	Tetrakis diethylamino titanium(IV)
TDMAV	Tetrakis dimethylamino vanadium(IV)
TDEAV	Tetrakis diethylamino vanadium(IV)
PDMAT	Pentakis dimethylamino tantalum(V)
EDLC	Electronic double layer capacitor3

Compound names are often referred to using combinations of these abbreviations for more complex organic structures.

Chapter 1: Introduction.

1.1 Motivation.

This project stems from the pressing need to lower reliance on fossil fuels as an energy source. This requires the development of more sustainable sources of energy and the ability to efficiently capture and store the energy that is produced. Current energy storage technologies can, either, quickly capture energy in capacitors or store large amounts of charge in batteries. In theory, these two can be used to complement each other, however, in cases where the amount of charge needing to be captured is large, for example, in regenerative breaking systems or where space is at a premium in portable electronics, the coupling of these devices can be inefficient or impractical. What is desirable is a device that combines the fast charge rates of capacitors with the power density of a battery. These devices are known as supercapacitors.

1.2 Capacitors.

In order to understand supercapacitors, an understanding of conventional capacitors is necessary. Capacitors are electrical components present in most electrical devices.[1] They can fulfil a variety of different functions in a circuit including, for example, a temporary power source,[1] DC filtering and to provide high load currents/voltages to components such as the starter motor in cars. In simple terms, a capacitor works by storing energy as a potential difference between two conducting layers, separated by a dielectric or insulating layer, normally consisting of one of the following; a vacuum, a ceramic, a paper or plastic film or a solvent. The amount of charge stored can be increased by enlarging the area of the conducting layers, decreasing the distance between them or improving the charge shielding properties of the dielectric layer as per Equation 1. Conventional methods of increasing the energy density of capacitors have involved improvements in the dielectric material (to increase ε_r) and methods to make the dielectric as thin as possible (to decrease d). A modern capacitor is typically made of two electrode materials rolled round tightly around each other to increase the surface area in a given volume. The dielectric is printed on to one of the electrode surfaces before they are sandwiched together and rolled (Figure 1).

$$C = \frac{\varepsilon_o \varepsilon_r A}{d}$$

Equation 1

Equation 1. The equation for calculating the capacitance of a system using the overlapping area of the layers and the separation between them.[2] C is the capacitance in Farads, ε_o is the electrical permittivity of free space (8.854 x 10^{-12} F m^{-1}), ε_r is the relative electrical permittivity of the dielectric material between the layers (for a vacuum this value is 1 and for water at 20 ºC is approximately 80), A is the overlapping solvent/ion accessible surface areas of the conducting layers and d is the distance between the layers. This is idealised for a parallel plate capacitor where the plate separation (d) is small relative to the plate size (A).

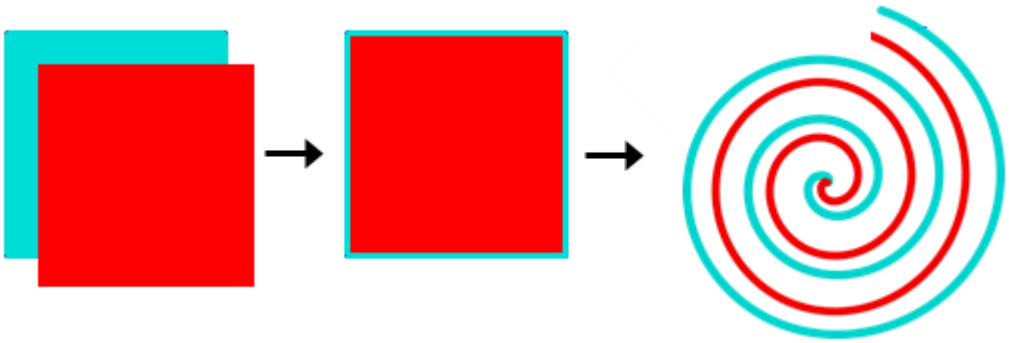

Figure 1: A basic schematic for how a capacitor is constructed.

The positive (red) side of the capacitor and negative (blue) side are layered together and the sheet formed rolled around itself. The dielectric layer between the two layers can be air as shown in this figure or any non-conductive material.

1.3 Electrochemical double-layer capacitors.

In order to increase the power density of capacitors beyond that available using a physical separator or vacuum, a layer of ions can replace one of the parallel plates. This effectively reduces the 'plate separation' ('d' from Equation 1 above) to the Van der Waals radii of the ions or the solvated ions in the electrolyte. Devices that make use of this are known as electrochemical

double layer capacitors (EDLC's). The structure of the layer of ions can be described by the Helmholtz and Gouy-Chapman models [2] (Figure 2 below). The dielectric material is formed from molecules of the solvent in which the ions are dissolved in or by free volume in the system. To maintain charge balance in these systems there must be a counter electrode with an analogous but opposite set of processes occurring.

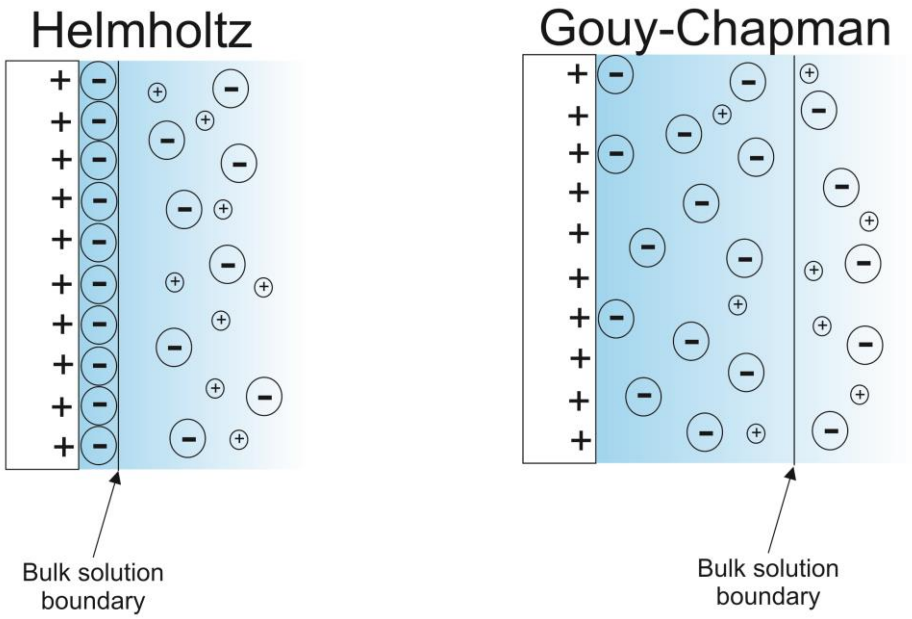

Figure 2: Sketches illustrating the Helmholtz (left) and Gouy-Chapman (right) models of the electrochemical double layer at an electrode/electrolyte interface.

In the Helmholtz model the potential difference between the surface and the electrolyte is dropped linearly across a very short region, approximately the same distance as the Van der Waals radii of the ions in solution, in the immediate vicinity of the interface before returning to zero difference for the bulk solution. In the Gouy-Chapman model the charge is balanced by opposing ions close to, but not all in immediate contact with, the surface. This creates a higher concentration of anions relative to the bulk, to a few nanometres from the surface. In reality a mixture of the two models occurs, with ions being adsorbed to the surface and a concentration gradient present close to the surface. This combination model is known as the Gouy-Chapman-Stern model.

This exchange of a 'near-by' plate for one formed of ions has the effect of making the plate separation as small as possible, potentially down to the Van der Waals radii of the atoms at the surface. This allows better access to rough surfaces, dramatically increasing the surface areas involved and reducing the separation distance as much as possible, resulting in an increase of the capacitance of the system.

1.4 Supercapacitors and redox supercapacitors.

'Supercapacitors' is a term loosely applied to electronic double layer capacitors (EDLCs) formed from high surface area carbons that have a high capacity per unit volume or 'specific capacitance'.[3] Combining this increased surface area with a redox active material that exhibits pseudo-capacitive redox reactions leads to devices known as 'redox supercapacitors'.[3] The terminology used in the field is far from standardised and several terms can apply to the same item, for example super- and ultra-capacitor. These pseudo-capacitative reactions are rapid and reversible reactions between the electrolyte and the surface of the electrode material. Energy is stored in the bonds formed between the electrolyte and electrode species and released when the reaction is reversed and the electrode material and electrolyte restored to their original state.

Redox supercapacitors are currently employed in some specialist applications in some fast charge hand held devices[4] and for recapturing the energy lost in slowing locomotives.[5] They have higher power densities than conventional capacitors by utilising redox reactions of the electrode surface and the electrolyte, and appropriate charge times to recapture a significant portion of the energy lost slowing the locomotive.

1.5 Oxides in redox supercapacitors.

Metal oxides are frequently utilised in research[3] as electrode materials for capacitors and cells for power storage applications. They're attractive targets in that they're usually easy to synthesise and, dependent on the elements in them, can be extremely economical. Their conductivities are generally not high, however, as the oxidising nature of oxygen tends to render metal centres back to their d^0 state, meaning that there are generally few or no electrons in the conduction band of the material to transport charge.

Currently, the best performing redox supercapacitors utilise RuO_2. However, the use of this is not widespread, owing predominantly to the expense of Ru[6] and environmental problems associated with its extraction.[7] A significant proportion of work on electrochemical capacitors has focused on RuO_2 and

$RuO_2.H_2O_x$, [8-11] which have promising redox processes and an ultra-high theoretical specific capacitance of 2000 F g^{-1}.[3]

The search for a cheaper oxide to use for electrochemical applications has been focused towards MnO_2. [12] Mn is a desirable metal to pursue for redox active processes[13] compared to Ru, owing to being comparatively inexpensive and more abundant, as well as possessing a wide range of available oxidation states. Alongside the study of metals for this purpose, high area activated carbons[3] and conductive polymers[14] have also been investigated.

A wide range of other metal oxide systems have been investigated for charge storage applications in addition to MnO_2 including; SnO_2 - Al_2O_3,[15] $Li_4Ti_5O_{12}$[16] and V_2O_5.[17] Study of a number of oxide systems has shown that increasing the solvent accessible surface area, normally by growing nanotubes [18] or rods of the desired material onto a substrate of choice, leads to an increase in the specific capacitance of the material. This is logical as, per Equation 1, increasing the surface area of the capacitor will lead to an increase in the capacitance. This could present a challenge when attempting to utilise a nanostructured electrode, which will be further discussed in 1.10 below.

Complications occur with oxides preference to form d^0 centres, meaning that there are no readily mobile electrons available around the metal centre for the conduction of electrons, leading to higher resistances than d^{1-5} metal centres and semi-conducting behaviours. The increase in resistance slows the rate capability of the material considerably, rendering these materials less applicable to devices that require fast charge and discharge times. This could be remedied by reducing the depth of these materials to an absolute minimum depth over a more conductive material. This will be discussed in more detail in the next section 1.6. Whilst this can be a major problem with electrodes constructed entirely of oxides, a thin surface layer of oxide material, with its short diffusion distance for electrons to the material surface and higher reactivity, can provide a more electroactive electrode material than a purely nitride electrode.

1.6 Band theory.

Band theory is a theoretical model for describing how the possible energy levels of an electron around an atomic nucleus, leads to the atom or material

having certain characteristics, such as conductivity. As the electronic structure around an atom is quantised, these 'bands' have the greatest density of allowed states. Regions of the energy range where a 'band' does not cover are known as band gaps. The Fermi level (E_F) of a material is in the band gap between the bonding and anti-bonding orbitals of the material.

In relation to this work, a material with a band structure typical for a conductor is desirable. These materials have a bonding band lower in energy in their structure that is filled with electrons. Above this there is a 'band gap', where the density of states for electrons to attain is minimal, to another higher energy and partially filled band (see Figure 3, right). This partially filled band allows for electrons to move from state to state with minimal energy, conducting electrical charge with them as they do. This property is typically associated with metals like copper, but a range of ceramics, like TiN and VN, are also conductive. These materials have a high density of states close to the Fermi level of the material, leading to their metallic conductivity.

Insulators, like TiO_2 (Figure 3), have a full bonding band and no free electrons in the higher energy, anti-bonding band. This means that for electrons to be moved between states they need to be promoted over the band gap requiring a large amount of energy to be put into the material. This energy requirement manifests itself as resistance to the movement of electrons, measured in Ohms (Ω). Some materials, such as silicon, have a narrow band gap allowing them to conduct with a small input of energy. This band gap can be narrowed further in these materials by the addition of dopants which can insert an additional energy band around the Fermi level of the material (located in the boundary band gap). In the case of silicon these dopants are most commonly phosphorous and boron.

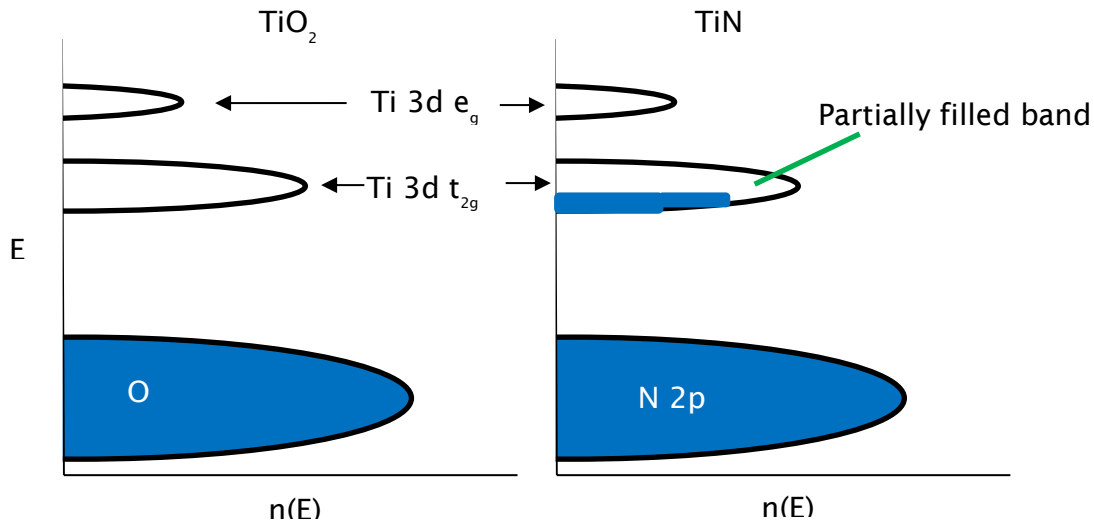

Figure 3: Simplified molecular orbital diagrams of the density of states in TiO_2 (left) and TiN (right).

The diagram shows how a partially filled band in TiN can lead to the movement of electrons with a small input of energy to promote them and how a large input of energy to cross the band gap is required for the same movement in TiO_2.

1.7 Nitrides.

Nitride materials are ceramics, the simplest of which occur as binary mixtures of a metal and nitrogen, such as TiN.[19] These can be employed in a variety of applications owing to a wide range of useful material properties. TiN is used as an abrasion resistant coating on a variety of tools. This abrasion resistance comes from the strong ionic bonding between the metal centre and the N^{3-} anion. Likewise, Si_3N_4 has been investigated in catalytic supports for methane oxidation[20] owing to its high thermal conductivity. Attempts have been made to expand the available range of oxidation states of metals centres within nitrides, with anticipation of accessing more unusual, catalytically active centres.[21]

A range of electrical conductivities exist within the nitrides family, ranging from metallic conductivity exhibited by TiN and VN, through the semiconductor behaviour of Hf_3N_4 and Ta_3N_5 to the insulating behaviour of Si_3N_4.[19] As discussed, these properties can all be exploited in a variety of ways. Materials with high electrical conductivity are of interest in this project to enable the rapid compensation of built up charge at the electrode surface,

allowing the electrode to store charge. Hence nitrides exhibiting good electrical conductivity will be of most interest.

Titanium Nitride (TiN) is a conductive binary nitride material with a range of engineering uses such as low friction dry joints and abrasion resistant coatings applied to drill bits and saw blades[19] (Figure 4); in electronics as a conductive separator between metallic and silicon based components to prevent or reduce diffusion of the metal species into the silicon and applications in costume jewellery owing to its golden appearance, favourable cost and hardwearing nature when compared to Au.

Figure 4: An example of TiN coated tool parts coated by CVD of $TiCl_4$, N_2 and H_2.[22] Reproduced with permission of the publisher.

TiN materials can be synthesised by the nitridation of Ti metal [23] at high temperatures, making a wide variety of substrates unsuitable. The same nitridation effect can be achieved using TiO_2 as the starting material but again, requires high temperatures [24] to fully convert the TiO_2 to TiN. A further prospect is the deposition of an electrode film via CVD from a volatile, nitrogen containing, Ti source.[22] However various problems may be encountered with the complex architecture desired in the project (discussed in sections 1.11 and

1.12 below). A sol-gel route for the potential production of a variety of morphologies was developed in the group recently[25] and will be discussed in more detail in section 1.9 below.

VN is a metallic conductor[19] that shares properties with TiN. When compared to semi-conducting V_2O_5,[19] this property makes VN an immediately more appealing target than the oxides of vanadium for electrochemical applications. Methods for the preparation of VN films include magnetron sputtering [26] and nitridation of V_2O_5.[27]

1.8 Nitrides in charge storage.

Nitrides are generally studied for charge storage applications as powdered samples of the material in a carbon matrix (Figure 9). This arrangement is very easy to fabricate, providing the MN material can be synthesised. However, this arrangement of the electro-active material can hide or suppress some of the properties of the MN being studied by limiting the available surface area of MN exposed to the electrolyte or the potential supply of current to the electroactive portion of the surface. In other words, the activity of the material with respect to its ability to conduct electrons quickly to the surface of the material, the morphology of the electrode and the ability of the electrode surface to react on a suitable time scale with the electrolyte needs to be considered and optimised to provide peak efficiency for the material. This will be explored more in section 1.10 below.

In the last 30 years, nitrides have been under study for power storage applications.[28] This started with a study into Li_3N [28] with the envisaged application as a Li storage material. However, a lack of stability towards anodic decomposition has rendered it to be of little practical use in cells. This led to research into other Li-MN's that may offer appreciable ionic conductivity. Many of these materials are of an antifluorite structure and are related to $Li_{2x-1}MN_x$. However, when M = B, Si or Al are used, the compounds are non-conductive, making them useful as ionic conductors of Li^+ but of little use towards capacitor applications. Switching from P block elements to transition metals yields increased electronic conductivity. TiN has received interest owing to its low cost when compared to a wide range of other materials, high molar density and superior chemical resistance.[29]

CoN has also been pursued as an electrode for Li ion electrode materials[30] giving good performance, comparable with CrN [31] and VN. [26]

NiN and CrN have both received interest with a view towards lithium battery applications as conversion electrodes, theoretically cycling from M + Li_3N to MN + 3Li (M = Ni or Cr).[32] Experimentally this gives stable capacities for these materials of 1200 mA h g^{-1} for CrN. CrN and NiN have reported values of 1800 mA h g^{-1} [33] and 410 mA h g^{-1} [34] respectively. Applications of NiN towards Na-ion battery electrodes have also been studied.[32]

Research with nitrides in the area of capacitors has been limited, owing to the redox active nature of the metal centres involved. When a non-metal has been employed, the nitride has been used as the dielectric layer, for example SiN_x has been researched as the dielectric for microelectronics devices[35] with promising results.

Nitrides have been the subject of significant research in the area of redox supercapacitors, especially TMN's. A range of materials have been investigated, with significant research into MoN based systems.[36] MoN has been shown to have a capacitance of around 220 F g^{-1} [37] as CVD deposited films in acidic electrolytes. Whilst this work has shown that nitrides can exhibit similar behaviour to the current commercially favoured material, the potential range over which MoN will operate is greatly reduced compared to analogous oxides (0.6 V for MoN and 1.4 V for RuO_2). Mo has also been combined with Co to form a CoMoN composite material [38] as a powdered MoN and CoMoN material with carbon electrode, giving a specific capacitance of 109.9 F g^{-1} in acidic aqueous electrolyte. This composite material exhibits a marginally better potential window than MoN.

Work on 3d transition metal nitrides has focused predominantly on TiN powders,[39] owing to their comparative ease of acquisition when compared to other metal nitrides, mainly due to their more widespread use.

These papers [4, 39] report specific capacitances for TiN of up to 240 F g^{-1} at low scan rates. The most promising area of research towards finding a more economical and abundant replacement for RuO_2 has been into VN (Figure 6).

TiN has been combined with VN in various nano-scale forms and morphologies for supercapcitor applications. This has usually been as a 'core-shell'

arrangement of TiN tube [40] or particle [41] core with a VN shell (Figure 5). This presents the interesting prospect of having a more conductive core with a more electroactive shell presented to the electrolyte, and shows comparable performance to the highest documented from TiN (~240 F g^{-1}) with an increase in the rate capability, effectively the length of time taken to charge/discharge the capacitor. As both TiN and VN are conductive, investigating a solid solution of the two materials will be interesting.

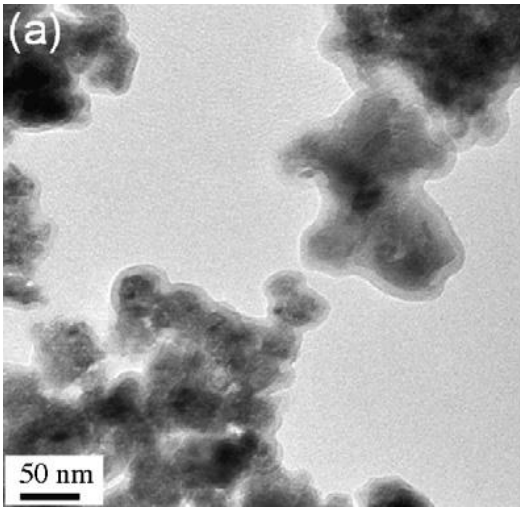

Figure 5: TEM image of a (Ti,V)N core shell nanoparticles.[41]

Reproduced with permission of the publisher.

Vanadium Nitride has a significant amount of interest in the field of EDLC's after reports of VN achieving high specific capacitances of 554 F g^{-1} at 100 mV s^{-1} and 1340 F g^{-1} at 2 mV s^{-1} (Figure 6).[42] These values are thought to be due to VN's high electrical conductivity and the presence of oxide and oxy-nitride species in the top few atomic layers of the VN's surface providing suitably fast redox processes. This value is comparable to some RuO_2 based systems currently in use commercially (~700 F g^{-1}).[8] This previous work has been conducted on powdered samples of VN embedded into a conductive carbon matrix. The use of a film comprised entirely of a metallic conductor provides a more uniform conduction pathway, which could lead to improved performance.

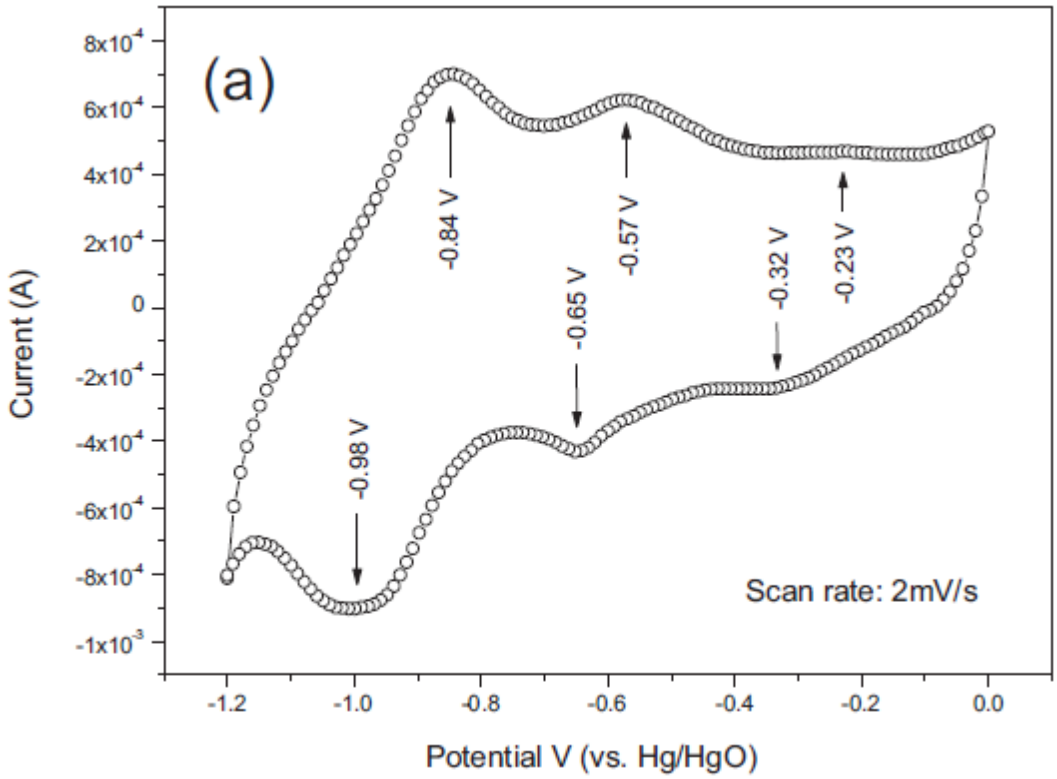

Figure 6: A 2 mV s^{-1} CV of VN synthesised at 600 ˚C in 1 M KOH.[42]

The capacity of the material displayed by this CV is 1340 F g^{-1}. Reproduced with permission of the publisher.

Whilst the above properties are all interesting in their own right, the specific properties that VN and TiN exhibit that are of interest to this project are that they are highly corrosion resistant[25] and conductive.[19] These properties, coupled with recent work[25] shows potential for the construction and synthesis of high surface area films of MN species which can be employed as electrodes in electrochemical capacitors with exceptionally high capacity.

1.9 The sol-gel route.

Sol Gel chemistry offers access to inorganic material morphology types that would otherwise be very difficult to produce[43] as shown in Figure 7. The chemistry of the process involves a series of condensation reactions between metal (or silicon) centres and a bridging agent. The majority of investigation into the mechanism of reaction has been carried out with silicon alkoxides, owing to their ease of handling when compared to the analogous amides.[44] With these and other oxide producing systems, the bridging agent employed is

water. In the system we propose to use, the bridging agent is a primary amine and the metal centre is $V(NMe_2)_4$, which will react together to produce a polymeric vanadium-nitrogen species.

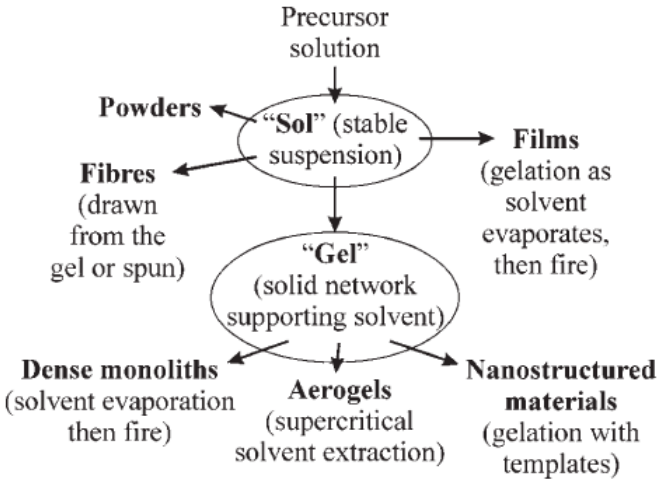

Figure 7: A diagram of the various materials morphologies that can be prepared via sol gel methodology.[43]

Reproduced with permission of the publisher.

The reaction sequence of a species closely related to the proposed vanadium amide starting material, $Ti(NMe_2)_4$, and n-propylamine investigated by Jackson and Hector [45] could proceed as shown below, in a scheme that is analogous to that exhibited by alkoxides and water:

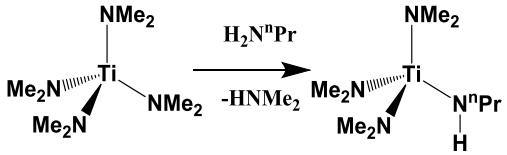

The propylamine displaces one of the dimethylamino groups, via nucleophilic substitution, from the co-ordination sphere of the titanium, losing a proton and displacing a dimethylamino group to maintain overall charge balance:

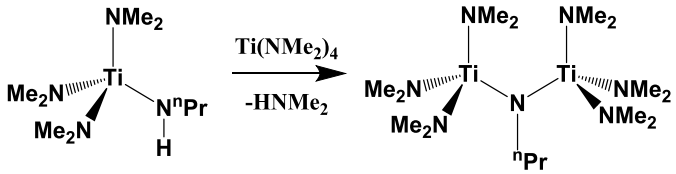

The remaining amine functionality displaces a dimethylamino group from a neighbouring titanium centre, creating a Ti-NR-Ti bridge:

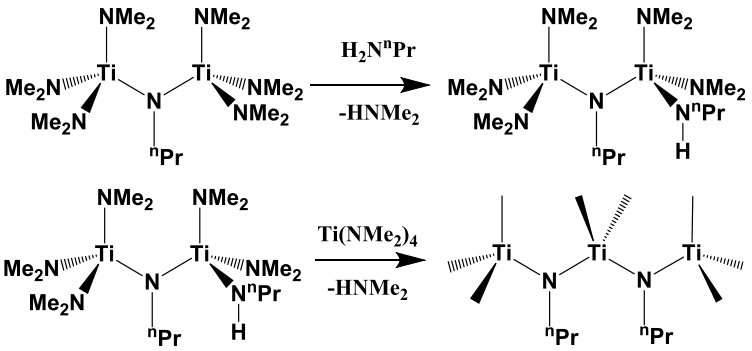

The titanium centres can then undergo further substitution of dimethylamino groups by propylamine followed by linking to further titanium centres, forming a large polymeric $(Ti\text{-}NR)_{\infty}$ structure (-NMe_2 groups omitted for clarity from last molecule). This structure could in theory be branched or linear, depending on the reaction conditions employed.

With alkoxide systems, the structure formed can be directed by the catalyst employed. Acidic catalysts encourage the formation of long polymeric chains, whereas basic conditions encourage the formation of globular poly-substituted particles.[43] Whilst metal centred sol-gel reactions behave similarly to silicon, the speed of the reactions is greatly increased, since the more electropositive metal centre is more susceptible to nucleophilic substitution and the larger metal centre is better able to expand its co-ordination sphere. With alkoxide based systems, the obvious choice of bridging agent is water. With amide systems the chemically analogous bridging agent is ammonia. This proceeds with a similar rate of reaction. However, the reaction of a metal amide directly with ammonia normally results in precipitation [46] of an amorphous solid, rather than sol formation. This is due to the ammonia acting as a tri-directional bridge, producing a species which is not properly solubilised by the aprotic solvents necessary for the amide chemistry. By using a primary amine, e.g. propylamine, the rate of the reaction is slowed and more non-polar regions are integrated into the polymer structure, allowing the formation of a soluble polymeric network.

At this point the reaction, where short oligomeric chains of the monomer have formed, is called a 'sol'. This is because the reaction mixture is still a flowing, though potentially viscous, liquid. At such a point that the polymeric network spans the reaction vessel this solution will appear to set and become more solid, either over time (via Ostwald ripening) or, more usually, as the result of

adding more bridging agent. This point is termed the 'gelation point' and is accompanied by a sharp increase in the viscosity of the solution.

The reaction solution will be used as a sol to infiltrate into templates of ordered 500 nm polystyrene beads, adapting the method previously developed for TiN.[25]

The methodologies employed for the production of VN (see 1.7) have limitations: magnetron sputtering is incompatible with the methods previously developed in the group, and may have complications associated with its application towards structuring the film in the complex manner desired for this project. Nitridation of V_2O_5 could potentially be used but will likely suffer from the change of crystal structure from V_2O_5's orthorhombic to VN's rocksalt, leading to the collapse of the desired inverse opal structure. This has been observed when attempting the nitridation of TiO_2.[25] For these types of films a sol-gel methodology must be pursued.

1.10 Micro versus nano structuring.

The structure of a film can radically alter its surface area, leading to interesting changes in many properties including the specific capacitance of a film. There are a range of methods for achieving an increase in surface area, usually by altering the surface area of the electrode employed to roughen it or reducing the plate separation to as little as possible increasing A and decreasing d from Equation 1 respectively. Generally, as pore size is reduced, the surface area of that surface will increase, logically leading (as per Equation 1) to higher specific capacitances. However, one potential disadvantage of making these nano-structured films for supercapacitor applications is that the electrolyte employed needs to reach the entire surface area for the full capacitance to be observed. If the rate of diffusion to and from the surface is restricted by the distance that the electrolyte and the active ions contained in it must diffuse, then the effective surface area that is being used will drop with every charge/discharge cycle.[47] This effectively reduces the surface area and causes the capacitance of the film to drop. One possible approach to solving this issue is to employ a micro-structured, rather than nano-structured, film. In this project, a large pore inverse opal film will be examined. Such films were produced in TiN as part of my undergraduate research project [25] (Figure 8).

The larger pore sizes and the extensive 3D interconnectivity of the pores should facilitate much easier diffusion of the electrolyte and ions around the film, into and out of the redox active zone close to the interface of the electrode and the electrolyte. Some references in the literature describe a limit to the relationship between increased surface area and increased capacitance.[47] This suggests that below a certain thickness the material forming the walls of the 'pores' is unable to hold or transport as much charge as might be expected. Kotz *et al*[47] predicted that on activated carbon electrodes above 1200 m^2 g^{-1} a plateau in the specific capacitance increase as a result of increasing surface area will be observed, according to their DFT models. They postulate that this could be because the nano-structures necessary for such extremely high surface areas are have insufficient space to balance the charge at the electrolyte-electrode interface. This effect is unlikely to have any discernible effect at the surface areas that could potentially be achieved in this work, as the walls of the pores are far thicker than those of nanostructured materials.

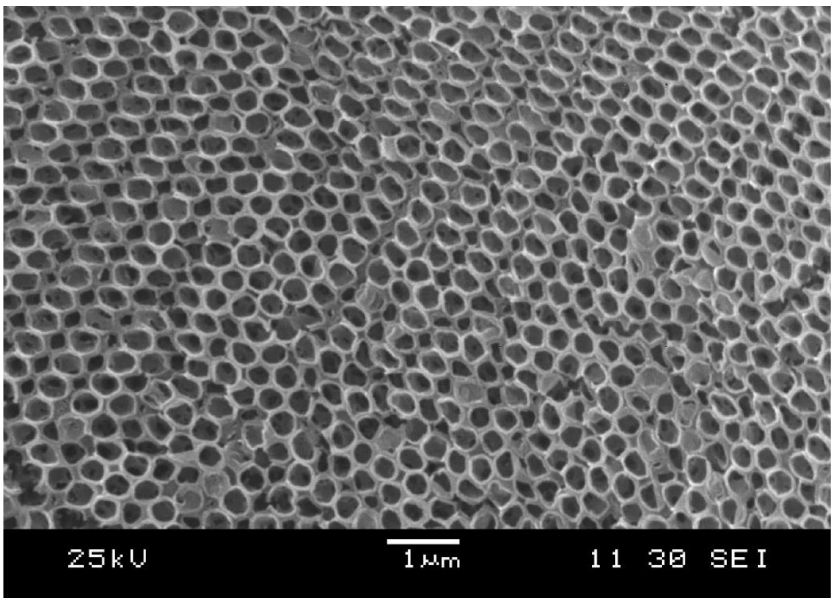

Figure 8: An SEM micrograph of a thin film of ordered macroporous nanocrystalline TiN on a silica substrate.

This image shows the extent of the ordering present in the complete domains. The films were prepared by infiltration of a titanium amide sol precursor into an PS opal of 500 nm polystyrene (PS) beads, followed by ammonolysis at 600 °C [25]

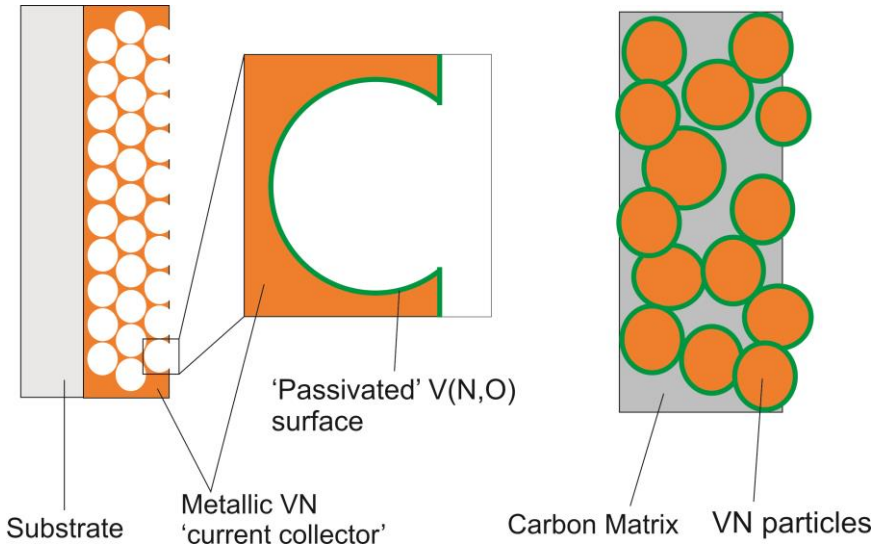

Figure 9: A diagram comparing an inverse opal structured VN film with a pressed VN/carbon pellet.

Current passing through the pellet will encounter several different resistances before reaching the redox active surface of the VN particles. The structured film has a much more uniform conduction pathway to the redox active surface. Additionally, the substrate would, ideally, be conductive to reduce conduction path lengths through the film.

1.11 PS opal synthesis.

The templates into which the sols are infiltrated to produce inverse opal structures (explored more thoroughly in the next section, 1.12), are commonly referred by a variety of terms; opaloids, photonic or colloidal crystals. These opaloid templates, consisting of close-packed spheres of a polymer or glass, may be infiltrated with a sol and then removed to leave an inverse opal structure.[48] A major interest in these structures is the formation of photonic crystals,[48] in which the light wavelength and the periodicity of the structure interact. Potentially, these could be used as optical filters by diffracting light of a specific wavelength away from the rest of the wavelengths.

These can be synthesised by a variety of methods, broadly divided into self-assembly, or 'bottom-up', and etching, or 'top down', techniques. Etching techniques, such as rapid prototyping [49] and focused ion beam etching,[50] offer the highest level of control over the structure produced. However, these methods can be expensive and time consuming. Self-assembly processes are

comparatively simple and inexpensive to perform. These include microphase-separation of block co-polymers [51] and evaporative crystallisation of colloidal particles/emulsions.[52, 53] The crystallisation method will be pursued for this project owing to its inherent simplicity. This method produces crystalline structures by deposition from a colloidal suspension of regularly sized particles, usually made from a polymer or silica. These particles can have a variety of diameters, ranging from 10 nm [48] up to micrometer sizes. This method nominally produces face centred cubic templates with growth proceeding with the (111) face parallel to the substrate. Such colloidal crystallisation to deposit a PS opal film can be directed to grow with the (100) face exposed using a patterned substrate [54] to direct the initial layer of beads to deposit such that the (100) face is parallel to the substrate.

The basic methodology for growing this style of template via a self-assembly method is as follows: A clean substrate tile of a suitable material is placed inside a sample vial, such that it is at a non-horizontal angle, with a fixed volume of the colloidal suspension surrounding it. This set up is then allowed to stand in a thermally stable environment so the solvent can evaporate from the particles. As the liquid level in the sample vial drops the suspended particles are deposited at the meniscus at a rate and depth dependent on a variety of factors.

This apparent simplicity of production has several controlling factors. The hydrophobicity of the substrate surface will determine the effective length of the meniscus between the substrate and the solution and, hence, the area over which deposition is occurring.[55] Other factors affecting deposition rate and depth are the deposition angle, temperature, humidity, and the concentration of suspended particles. By increasing the deposition angle (the angle at which the substrate stands relative to the perpendicular plane of the meniscus) the meniscus of the solution is lengthened along the substrate.[48] A longer meniscus (from a substrate flatter to the surface) should increase the amount of time that the particles have to settle onto a surface, allowing them to better find the most ordered, lowest entropy state. Temperature and relative humidity both effect the rate of solvent evaporation; temperature proportionally and humidity inversely. Rapid evaporation leads to faster deposition with a reduction in the number of defects present. The temperature is controlled by the incubator/oven thermostat. The humidity is adjusted by

the number of PS opal s grown concurrently, as well as, the total volume of liquid present in the system. The concentration is proportional to the number of layers of particles deposited and, hence, the template thickness. In theory, the higher the volume fraction of the particle spheres, the thicker the templates produced. In practice however, thicker templates are less mechanically stable, delaminating or flaking away from the substrate on handling.[52] A 1% solution has been reported[52] to produce the optimum templates in terms of depth and mechanical stability.

These templates can then have the interstitial voids between the spheres filled in a variety of methods. Atomic Layer deposition (ALD) is one method by which this may be achieved.[56] This process is where a single layer of atoms is deposited per cycle, allowing the material to be built up layer by layer over time. This allows a great deal of control over the deposition process as well as the morphology and material produced. However, the drawbacks to this method are the time consuming nature of depositing a single layer of atoms per reaction cycle. Another method used to infiltrate these materials is by electro-deposition and this has been used to great effect for metals[44, 57] and a select group of oxides.[58] However the nature of the chemistry used to prepare the amide precursors and the range of solvents in which these precursors and the beads are stable is limited and so one of the key variables for electrodeposition (the solvent) is essentially removed. The literature on the electro deposition of nitride materials or precursors is also very limited. The most effective method will, therefore, be sol-gel infiltration as described in section 1.9 above.

1.12 Inverse opals.

As with understanding supercapacitors, to understand what inverse opals are we must first understand what opals are. Opals are deposits of silica crystals in silica, similar to a bucket filled with marbles then with sand poured into the void spaces. Opals often find uses in Jewellery owing to the 'Opal fire' diffraction effects/iridescence that can arise when the encased silica crystals are on the same length scale as visible light. The different densities of the two silica phases causes light to diffract when passing between the boundary of these two materials, splitting the light like a prism. The 'opalfire' effect observed in natural opals is caused by the irregular nature of the engulfed

silica particles diffracting a variety of visible wavelengths of light. Opal structures can be made to diffract a single wavelength of light by switching the irregular particles for ones of a uniform size and shape. These can be made by depositing a template structure from controlled size silica beads and infiltrating a silica precursor into the void space, before heating to convert the precursor into the final product.

The silica opal template used in the above synthetic procedure is difficult to remove owing to the relatively unreactive nature of silica, it requires harsh basic or HF washes to be employed, potentially damaging the material produced. However, the use of a more easily removed 'sacrificial' template, such as one made from an easily combustible polymer, means that the preparation of a structure where the 'void' spaces in the template volume are occupied by solid material and the space formerly occupied by the template is vacant creates the inverse of the regular opal structure, an inverse opal.

Inverse opals find use where ever a structure with good diffusion around it is required, for example as a catalytic support for solid-gas and solid-liquid reactions.[59] They are under study with potential uses as a photonic gate or wave guide in optical computing and telecoms applications.[52]

1.13 Project aims.

The principal objective of the project is to synthesise ordered macroporous 'inverse opal' films of transition metal nitride materials, specifically VN and TiN, and to examine their use in electrochemical capacitors. This involves the infiltration of a suitable template[25] with a vanadium amide derived 'sol'. The project will involve the synthesis of a suitable vanadium amide sol precursor and high quality PS opal templates. Following this, the synthesised materials will be characterised by scanning electron microscopy (SEM) and X-ray techniques. As the capacitive properties will be dependent on the surface composition of the films, various treatment methodologies will be explored to optimise the capacity. This project can be separated into several distinct areas: The synthesis of the metal nitride precursor compounds and sols, the preparation of templates and the electrochemical testing and optimisation, demonstrated in Figure 10.

The first area to be explored is the feasibility of producing a 'sol' type material from vanadium amide species. This process has been previously explored and published for Ti,[46] Cr and Ta.[60] There are no published studies towards examining the application of this process with vanadium containing species. This should be possible as the early transition metals behave very similarly to each other. Attempts can then be made to explore the possibility of combining TiN's inherent stability with VN's more desirable electrochemical properties, and examine the potential of this kind of reaction working with other d block metals.

These infiltrated templates will be heated to temperatures above 450 ºC in flowing ammonia. This serves two purposes: Firstly, the hydrocarbon templates are completely removed by the heating process.[25] Secondly, the higher temperatures aid in the formation of the crystalline phases for necessary electronic conductivity. This crystallite formation has the added bonus of increasing the corrosion resistance such that only the surfaces of the metallic crystallites are passivated. This also makes analysis of the films by X-ray diffraction more straight forward. Furthermore, the ammonia aids in the removal of carbon containing species (propyl and methyl groups) from the films and helps to solidify the structure before the template is removed by acting as a tri-directional bridging agent.

The second area for exploration is the improvement and advancement of the methodology used for producing structured films already established within the group (these types of films and the methodology for preparing them are explored in section 1.11). Previously within the group, these have been prepared by a top down evaporative method, which generates films with areas of short range ordering randomly orientated across the substrate, with only a single size of polymer bead. Areas that could be investigated further are: Altering the bead size used for deposition; comparisons of the effect of pore size on electrode capacity; methods to improve the long range ordering of these templates to create a more uniform electrode surface.

The third area for investigation is evaluation and potential optimisation of the electrochemical performance of these structured materials. This optimisation could be performed by modification of the surface of the synthesised structured electrodes (e.g. by heating under air) to increase the amount of

charge it will store. Owing to the difficulty inherent to the synthesis of the structured electrodes, this optimisation will be tested on nitrided metal foils before potentially being applied to the structured electrodes.

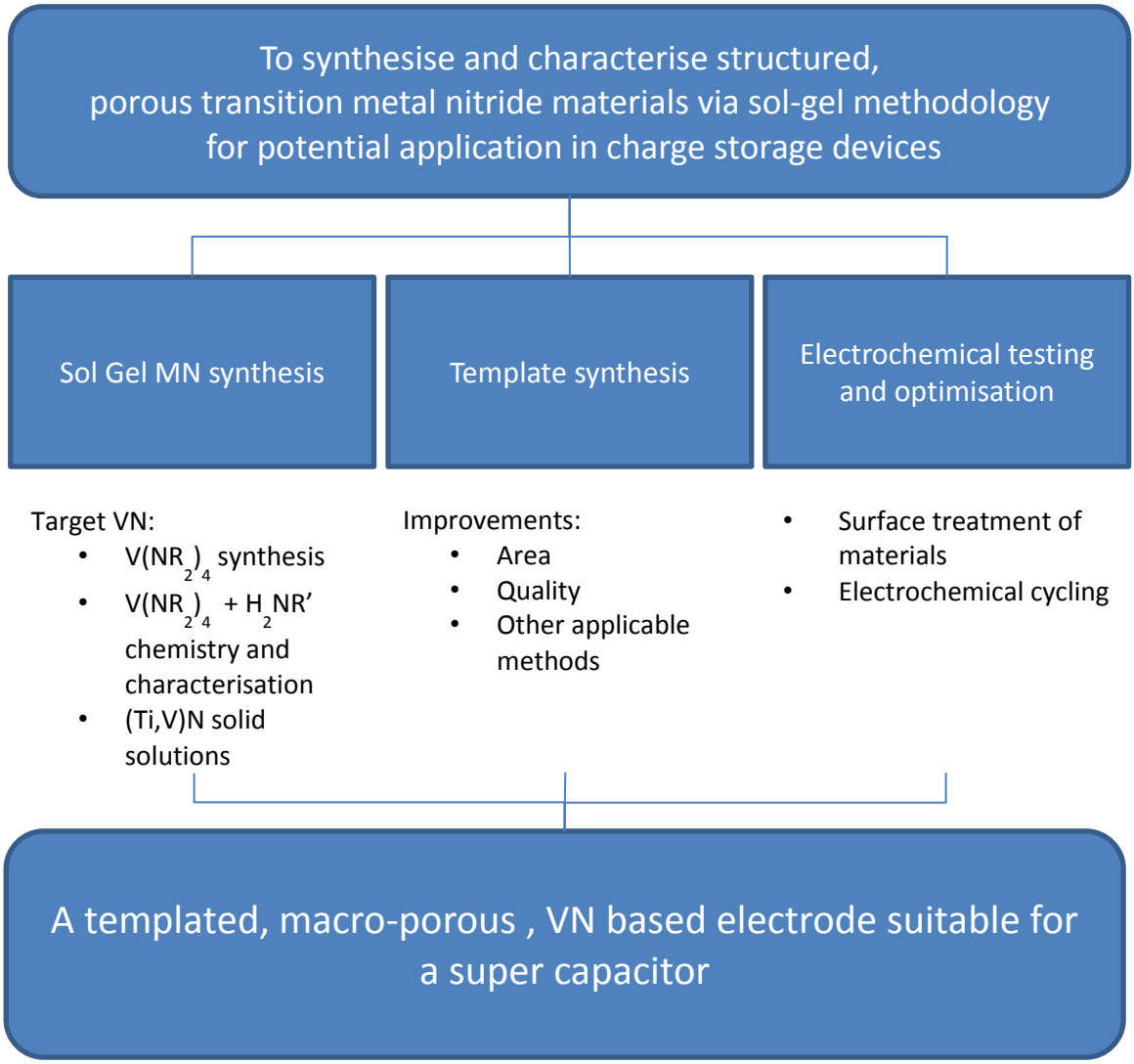

Figure 10: A flow diagram showing the breakdown of areas of study for the PhD project.

Chapter 2: Experimental.

2.1 General.

All reactions were carried out using inert atmosphere techniques with argon or nitrogen atmospheres (specified where Ar was used), using a glovebox and Schlenk line where appropriate. In the Schlenk line, a vacuum pressure was maintained at a maximum of 0.05 mm/Hg, which was checked daily using a Macleod gauge. Whenever possible, previously unpunctured subaseals were also used.

The glovebox used was an N_2 filled MBraun Labmaster and was used only when the H_2O and O_2 content were below 1 ppm and 5 ppm, respectively. Solvents were distilled over, either, sodium/benzophenone or barium oxide, as appropriate, under a dry N_2 atmosphere.

'Deionised' water (DI) was purified by reverse osmosis in an ELGA Purelab option DV35 to 0.1 µSv.

$Ti(NMe_2)_4$ and $Ta(NMe_2)_5$ were supplied by Epichem and used as received. KOH, IPA, acetone, EtOH were supplied by Fisher and used as received. Et_2O, THF, hexane, pentane, benzene and MeOH (Aldrich/Fisher) were dried by distillation over sodium/benzophenone for a minimum of 6 hours. Diethylamine and propylamine (Fisher/Aldrich) were dried over BaO for a minimum of 6 hours. All dried solvents were stored under dry N_2 until required in sealed Youngs tap flasks. Ti metal foil, TiN powder, VCl_4, $VOCl_3$, molecular sieves (3 Å and 4 Å) and BaO powder were supplied by Aldrich and used as received. Na metal was supplied by BDH and used as received. V metal foil was supplied by Goodfellow Cambridge Ltd and was used as received. BuLi was supplied as a 1.6M solution in hexane (Aldrich and Fisher) and was used as received. DVB cross-linked, amidine capped PS beads were supplied by Invitrogen. N_2 and Ar gases were supplied by BOC and used as received. Electronic grade NH_3 and BIP grade N_2 were supplied by Air Products.

Glassware was dried for a minimum of 12 h at 100 °C prior to use.

2.1.1 NH_3 distillation.

NH_3 was distilled from an NH_3 cylinder (electronic grade, Air Products) and stored in a pressurised steel can to provide a ready source of very dry NH_3 gas. Owing to the risks associated with this procedure, it should never be left unattended for any reason and must always be conducted by at least two able individuals. NH_3 gas is toxic by inhalation, corrosive and flammable. As with distilling organic solvents over sodium, extreme care must be taken to exclude moisture to avoid possible explosion and/or fire.

Na metal (~8 cm^3, in ~0.5 cm^3 chunks) was placed into an N_2 flushed, 3 neck round bottom flask (RBF, 1 L) fitted with a subaseal and hose connected to the NH_3 supply, gas outlet connected to a Schlenk line, an inert atmosphere thermometer and a large stirrer bar. The RBF and a custom built NH_3 can with a burst disc and pressure gauge were then chilled in cardice/EtOH baths before NH_3 (~500 ml) was allowed to condense slowly into the RBF over the sodium, giving a dark blue solution. The volume of NH_3 was not directly measured, the 1L RBF was half filled. A bronze gold film was observed above the meniscus of the NH_3 from the presence of NH_3 in the metallic Na.

The flask was then allowed to warm very slowly, such that the ammonia evaporated from the RBF into the chilled can. The temperature of the RBF was held between -20 °C and -30 °C to maintain some control on the rate of transfer from the RBF into the can, by holding the RBF inside a bowl (to exclude the draft from the fume hood airflow) containing a sparing amount of cardice/EtOH. Care was taken to avoid chilling the pipes leading into the can so as to prevent NH_3 condensing in these areas, which would have led to a pressure build up in the system.

Once the majority of the NH_3 had transferred into the can, it was sealed and carefully disconnected from the RBF, before both were allowed to warm to RT. The can was stored at the back of a fumehood and the sodium was disposed of safely using sequential washings with IPA, EtOH and water.

2.1.2 Polystyrene opal template growth and use.

Control of the hydrophobicity of the substrate surface is a key variable for ensuring the growth of the templates. Whilst the conditions detailed may seem

harsh they are the ones that worked, gentler conditions were investigated but gave undesirable results, from no deposition of the colloidal solution to no order in what deposition did occur. Care must be taken to use clean tools, gloves and surfaces when handling the PS opal s. All must be free from dust, grease and oil and at all costs, handling of the substrates must be avoided unless absolutely necessary. Extra care must be taken in the glovebox as the atmosphere and the surfaces inside are far from clean/grease free and the loss of dexterity inherent in using the gloves means that accidents are more frequent.

2.1.2.1 Substrate preparation.

Substrates of an appropriate size and material were prepared with the assistance of a range of support staff.

For normal glass (amorphous silica) substrates, microscope slides (25 x 75 x 1 mm) were trimmed to size (50 x 12.5 mm) using a glass knife

More specific sizes were cut by the in-department glass blowers, as were silica substrates. The specific size of the substrate was calculated using basic trigonometry to create an angle of around 75° to the base of the flat based and non-necked 'specimen tubes' employed.

To remove the various forms of oily residue from manufacture, handling/transportation and preparation, the substrates were rinsed first in DI to remove major deposits of dirt. The substrates were submerged in acidic piranha etch. This was made fresh each time it was required, in quantities of no more than 300 ml at any one time and in glassware that was at least three times this volume (typically a 1 L beaker was used). The piranha was not stirred once it had been prepared and was left undisturbed until cool. It was then diluted with at least twice its volume of DI before the substrates were removed from the piranha beaker.

After the degreasing steps detailed above, the substrates were individually removed from the degreasing media, rinsed with clean DI, blown dry with a stream of dry N_2 and laid out onto a clean piece of tissue in an unoccupied fume cupboard until completely dry. The substrates were inspected and the degreasing procedure repeated if any surface marks from deposited residues

were observed. The clean, dry substrates were stored together in a sealed airtight bottle until required.

If the material grown onto the substrates was eventually intended for electrode testing, then the cleaned substrates were Au coated on a single surface at this stage. This was performed by Alistair Clark.

If the substrates were to be used in a manner that required anhydrous conditions, for example, depositing a flat nitride film, then the sealed jar was transferred to the glassware drying oven in the lab and left unsealed at least 24 hours before the substrates were required. Otherwise the jar was stored safely until the substrates were required.

2.1.2.2 PS opal growth

The following is adapted from a literature procedure[52, 53] previously used with different PS beads and substrates.

Substrates (glass or SiO_2, 1 mm thickness) were cut to the correct size (23.5 mm x 23.5 mm, size determined by the specimen tubes used) then cleaned as detailed above (2.1.2.1), the best results were obtained with substrates cleaned with sequential sonications in solvents (detailed above in section 2.1.2.1).

A 0.1% solution of polystyrene (PS) beads was then prepared by sonication (10 minutes) of the stock solution (4.2 %, Invitrogen) to evenly disperse the PS beads, before a portion was withdrawn and diluted with DI H_2O. The diluted solution was then re-sonicated (10 minutes) before being carefully divided into flat bottomed specimen tubes (6 ml/tube) containing the cleaned substrates, avoiding splashes of any kind. A further tube containing 6 ml of H_2O was prepared and all 8 tubes were placed roughly equidistant from one another and the edges of the tray. These were carefully transferred to a preheated oven (65 °C, preheated for at least 6 hours prior to use, Lenton oven modified such that the fan could be switched off) and left undisturbed for a minimum of 72 hours so that the H_2O could evaporate. The tubes and template PS opal s were removed and visually inspected for obvious defects, such as a lack of deposition and lack of visible iridescence, before being carefully transferred to a desiccator for storage using clean, dry tweezers until infiltration.

2.1.2.3 Infiltration of templates.

This has been shown to work with sols based on Ti, V and Ta amides.

A metal amide containing sol was prepared in hexane and transferred to an ampule so that it could be safely taken in and out of the glovebox. Once transferred and sealed, this sol, PS opal templates, pipettes and clean dry specimen tubes were transferred to the glovebox. The PS opal s were carefully placed sideways into the specimen tubes using tweezers so that any banding on the PS opal ran perpendicular to the sol meniscus. A small volume of the sol was carefully pipetted into the tube, so that the lowest edge of the template was just submerged and the sol made no contact with the PS opal other than this interface. The tubes were then carefully sealed, to protect the glovebox seals from the organic solvent vapour, and allowed to infiltrate for 1 hour. The now infiltrated template was then carefully removed from the tube using tweezers transferred to a clean specimen tube and sealed for 2 hours to 'age' and allow for any cross linking to develop fully. The aged, infiltrated templates were then transferred to a crucible boat and placed into a reactive gas furnace tube, equipped with three Youngs taps to allow the system to be isolated from air throughout the process, sealed with hydrocarbon grease.

Hexane sols must be used as the template beads dissolve or swell and distort in all other tested aprotic organic solvents compatible with the metal amide chemistry. This has been confirmed[25] with THF, Et_2O and toluene, as well as protic $HNEt_2$.

2.1.2.4 Nitridation of infiltrated templates

The PS opal s and furnace tube were transferred under inert atmosphere to the fume cupboard. The tube was connected to the NH_3 supply via a ~60 cm length of 3 Å molecular sieves before the connecting tubing followed by the furnace tube were purged for 15 minutes each with anhydrous NH_3. The flow rate of NH_3 was then adjusted to one bubble/second and the PS opal s heated in a tube furnace to an appropriate temperature for the metal amide sol involved. This was found by experimentation with bulk samples of the material (Ti 600 °C, V 550 °C, Ta 700 °C), to produce the desired metal nitride, at a heating rate of 2.5 °C/min for 10 hours. The furnace was then allowed to cool no faster than 5 °C/min. Once the furnace tube was at a temperature of

less than 150 °C, the tube was removed from the furnace and the ammonia was purged from it with dry N_2 for 10 minutes. The crucible boat was carefully removed and the PS opal s transferred to clean specimen tubes for storage prior to analysis and use.

2.2 Electrochemistry.

All electrochemistry experiments were performed using a Biologic SP150 or a Biologic VMP2 potentiostat, both running ECLab software.

2.2.1 Preparation of a Hg/HgO reference electrode.

Pt wire (10 cm x 0.5 mm) was sealed into a short length of glass tube (7 mm ID) using an epoxy resin filled syringe to deposit resin around the wire inside the tube, such that ~2 cm of the Pt wire extended beyond the resin into the tube. Once set, one drop of $Hg_{(l)}$ was placed into the tube on top of the exposed Pt wire and another drop was ground into a brown powder with HgO (~100 mg). This powder was placed on top of the bead of Hg so as to cover the Pt wire. This was secured with tightly packed glass wool before being soaked in carefully prepared $NaOH_{(aq)}$ solution (0.1M) overnight. The reference electrode was then fitted into a fritted capillary tube filled with NaOH (0.1M) and left to stand, frit down, in $NaOH_{(aq)}$ (0.1M) (Figure 11).

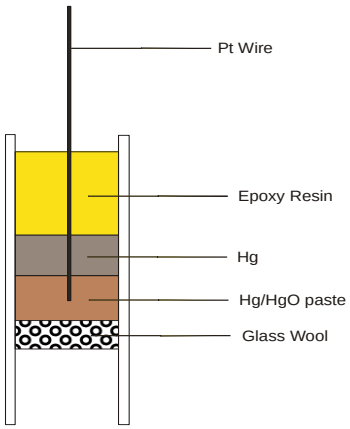

Figure 11: A schematic diagram of an Hg/HgO reference electrode.

2.2.2 Cyclic voltammetry.

Cyclic voltammetry measurements were performed using a three electrode cell, consisting of: A working electrode, a high surface area Pt gauze counter electrode and a Hg/HgO (in 1M NaOH) reference electrode. Scan rates were varied, from 1000 mV s^{-1} to 2 mV s^{-1}at room temperature in 1M KOH, in order to explore the behaviour of the electrode thoroughly. KOH solutions were prepared from KOH pellets (Fisher) in small batches (250 or 500 ml) and used in approximately 100 ml aliquots in the cell. The KOH solutions were stored in stoppered volumetric flasks. The electrolyte was degassed by gently bubbling dry N_2 through the solution for a minimum of five minutes between different electrodes, after the cell was set up, taking care not to allow the electrolyte to splash onto the clip holding the working and counter electrodes in place. The voltammograms were recorded over a set of 10 sweeps per scan rate with a rest period of 30 seconds between scan rates. The potential windows typically recorded over were between -0.8 and 0.3 V for TiN and -0.8 and 0.2 V for VN samples.

The potential window was optimised so that no gas evolution was observed during the potential range sweep by either the formation of gas bubbles at the sample or the large current changes associated with H_2 and O_2 evolution. The potentials at which this occurred were found by observing a sweep over a much wider range than that which the electrolyte was anticipated to be stable over. The window was then reduced so that the edge of this peak was no longer within the scan range. For redox inactive species, like TiN, this gave a stereotypical capacitance 'letterbox' from double layer charging, with redox active materials this gave the letterbox shapes with the redox peaks imposed onto it.

Specific capacitances were found from these scans by taking a single cycle of the scan and calculating its total area using EC lab software. All features observable on the cyclic voltammogram collected were included in this area. This area was then halved to account for the forward and reverse contributions from the cycling and the current value converted to Farads. This was combined with the measured surface area of the electrode material. For films, this was found from the geometric surface area of the electrode and the surface roughness value calculated from AFM results. The surface area or

mass of material employed was used to give a specific capacitance of F cm^{-2} for films or F g^{-1} for powders respectively.

2.3 Instrumental.

A large range of instrumentation has been used throughout this project in order to investigate the reactions and surface compositions of the materials and processes under study. Below is a brief description of how each of the less typical methods function, followed by the details of how each instrument was used.

2.3.1 Infra-red spectroscopy.

IR samples were prepared by one of two methods. A small sample of the material was mixed in the glovebox into dry CsI and pressed into a thin disc, before mounting into an airtight holder with CsI windows. Alternately samples were prepared as a nujol (dried over Na) mull in the same CsI holder. Spectra were collected on a Perkin Elmer Spectrum 1 spectrometer with CsI optics between 4000 cm^{-1} and 200 cm^{-1}. CsI discs were used for solids that were not expected to dissolve or suspend in nujol. This was usually for ammonolysis products. The key features under observation for IR studies in this project were those indicative of the molecules and materials under synthesis according to the literature

Table 1: The key IR band ranges expected in this project.[61]

Approximate peak vibration (cm^{-1})	Assignment
525-615	M-NR_2 stretches
940-1200	MNR_2 C-N stretches
3000-3500,	R_2N-H stretch (not expected)
1550-1650	R_2N-H bend (not expected)

2.3.2 Nuclear magnetic resonance.

Nuclear magnetic resonance (NMR) was used primarily to test for the purity of the synthesised amides and for tracking the progress of transamination

reactions. Literature sources for the expected shifts of the vanadium amides are non-existent, so these shifts have been assigned based on those for the corresponding Ti amide.

NMR samples were prepared by dissolving the compound under study in deuterated solvent (C_6D_6 or $CDCl_3$, Aldrich) in the glovebox and carefully sealing the cap onto the NMR tube with parafilm before acquiring the spectra as quickly as possible. For samples where an extended stay in the NMR tube was required, an NMR tube with a Youngs tap adaptor was borrowed from another research group. This tube, owing to its expense and reusable nature, was best cleaned starting with dry MeOH to remove the metal amide species before being cleaned and dried as normal.

2.3.3 White light interferometry.

White Light Interferometry (WLI) makes use of the principle that the phase of a wave will allow multiple waves to interact with one another constructively or destructively. Information about the surface that the waves are reflecting and scattering from can be extracted from this interference effect. The sample under test is illuminated by a broad band 'white light' source at the same time as a reference sample. The two sets of beams, those reflected from the sample and the reference, are then transmitted into a CCD and the information about the difference in the phase of each wavelength is undergoing is converted into a correlelogram. Analysis of this correlelogram can be used to generate data such as surface roughness of samples.

WLI was conducted with assistance from Chris Spindloe at Central Laser Facility Target Fabrication, RAL on a Talysurf CCI 3000.

2.3.4 Atomic force microscopy.

Atomic Force Microscopy (AFM), sometimes called scanning force microscopy, is performed by rastering a nanoscale probe across a surface. It is used to generate an image of surfaces and objects by 'feeling' them with the probe tip. As the tip is moved closer to the surface, the cantilever arm that the tip is mounted on is deflected away from the surface. This deflection is measured by reflecting a laser off the cantilever and over a grid of photodiodes. The

image can be produced by measuring the deflection of the probe in 3 different modes: Contact, tapping and non-contact.

- Contact mode. The tip of the probe is moved across the surface or at a constant repulsion force and the deflection to its position measured.
- Tapping mode. The probe is oscillated at its resonance frequency. As the probe tip approaches the surface of a material, the intermolecular forces present cause the amplitude of these oscillations to decrease, proportional to the forces exerted by the surface. The variation in the amplitude of the tip is measured and converted into a topographic representation.
- Non-contact mode. This is essentially a variation of the tapping mode where the tip is oscillated at its resonant frequency, close (<10 nm) to the surface of the sample. Van der Waals forces disturb the frequency of the tip, which is maintained by adjusting its height above the sample. A topographical representation of the sample surface can be generated by measuring this displacement or the variation in the frequency of the oscillation.

AFM was performed with assistance from Marek Jura at ISIS, Oxfordshire on a Bruker Dimension 3100 Scanning Probe Microscope. The instrument was run in tapping mode and the data processed with the software provided with the instrument

2.3.5 Scanning electron microscopy.

Scanning electron microscopy (SEM) images surfaces by accelerating electrons from a filament or field emission source onto the sample, then rastering the beam of electrons across the surface like a cathode ray tube. The electrons impacting onto the sample surface can excite the sample surface in a number of ways. The electrons can be scattered elastically from the surface. They can be absorbed and the excitation relaxes by ejecting an electron from the surface, often referred to in this context as secondary electrons. The absorbed energy can be released as electromagnetic radiation characteristic of the emitting element. All of these kinds of emission can be detected and converted to images or spectra. The electron beam is focused down to sub-

micron sizes using a series of magnetic lenses. Depending on the sample, accelerating voltage and the filament type of the instrument, a resolution as good as 1 nm can be achieved. A higher accelerating voltage implies a shorter electron wavelength as per $E = h\nu$. The sample needs to be very stable to electron bombardment and highly conductive for the highest resolutions to be observed. Sample conductivity can be increased by coating the sample in a conductive medium, such as carbon or gold. A conductive pathway between the sample surface and the sample stub must be maintained so conductive adhesives are used to mount the sample to the stub. Depending on the nature of the substrate (e.g. glass or SiO_2, an insulator) it was necessary to add a small piece of conductive carbon tape from the sample surface to the stub.

SEM images were collected on a Philips XL30-ESEM, a JEOL JSM5910 SEM or JEOL-JSM6500F, running under high vacuum conditions and using secondary electron imaging (SEI). SEM samples were prepared, wherever possible, without using any coating. This allowed the samples to be analysed accurately using EDX (Energy Dispersive X-ray spectroscopy, see 2.3.6 below) to gauge the elemental nature and composition of the surface. Where higher resolution images were desired or non-conducting samples were analysed, Au was used as the coating element. The accelerating voltage was varied between 5 and 30 kV, depending on the sample being analysed, the detail required from the image and the stability of the sample surface.

2.3.6 Energy dispersive X-ray spectroscopy.

Energy dispersive X-ray (EDX) spectroscopy is an analysis technique for evaluating the compositions of materials, usually used in conjunction with SEM. When electrons are bombarded onto a surface, the energy from the electrons can be absorbed by the atoms on the surface, ejecting a core electron. In order for these now excited atoms to return to a stable ground state, the absorbed energy can be emitted as excited electrons (used for SEI) or as radiation in the form of X-rays. EDX measures the energy of these X-rays to identify and quantify the atoms that emit them. Owing to the quantum nature of the atomic structure, the energy of the emitted X-rays is quantised into values specific to the energy differences between the electronic layers surrounding an atomic nucleus. This allows for the identification of atomic

species within the sampling volume of the technique. Counting the number of X-rays emitted for each energy value, in conjunction with the absorption coefficient of each species, can give a reasonably accurate estimate of the surface composition of a sample. This accuracy is usually determined to the nearest % is usually considered as the accuracy of the technique, for heavier atoms this can be increased to 0.1%. EDX allows for a non-destructive method of assessing the elemental composition of a sample.

EDX has a minor drawback, owing to the fact that the energy of X-rays is being determined and a number of atomic nuclei are relatively poor absorbers of electrons, the depth into a sample surface over which atoms can be excited can, typically, be around a micrometer.[62] This gives a 'bulk' reading of the sample, which can hide pertinent information about a sample surface, hiding the chemical rational for certain reactions and processes. Conductive coatings, such as C and Au, will also be excited and distort the atomic % at the surface of the sample or mask the peaks from the sample leading to larger errors in the composition readings. Whilst EDX is useful in analysis of the sample bulk, a much more surface specific analysis (See 2.3.7) method will be employed in conjunction for this project.

EDX was performed on uncoated samples wherever possible. When coated samples had to be analysed the peaks identified as the coating element (Au) were discounted from the estimated sample composition measurements. The accelerating voltage applied was at least 2.5 times the value of the highest desired peak to be observed, up to a limit of 30 keV. Sample acquisition time was 90 seconds. Data analysis was performed using the supplied software on an Oxford Instruments INCA EDX detector attached to a Joel JSMS 5910 and an Oxford Inca 300 X-ray detector (EDX probe) or a ThermoFisher Ultradry with NSST analysis system attached to a Philips Instruments XL30-ESEM.

2.3.7 X-ray photoelectron spectroscopy.

X-ray photoelectron spectroscopy (XPS) is an ultra-high vacuum technique that makes use of the photoelectric effect.[63] A sample is bombarded with monochromated X-rays of a known wavelength, usually Al K_α (1488 eV) or Mg K_α (1254 eV). The X-rays eject electrons from the atoms in the sample surface. The energy from this excitation enables the electrons to be ejected from the

sample surface, they are then collected and their kinetic energies determined. From the kinetic energies, the binding energy of the electron to the atom can be calculated from the following equation:

$$BE = h\nu - (KE + \Phi)$$

Where BE is the binding energy of the electron, hv is the energy of the photons used for excitation, KE is the measured kinetic energy of the electron and Φ is an instrumental work function to account for the energy difference between the Fermi level of the sample and the vacuum level, which is dependent on the instrument and the sample being analysed. As the energy levels in elements are quantised specific to the element they are associated with, the electron emissions are quantised with respect to the element. This means that XPS can be used as a sensitive probe to identify sample composition.

As XPS measures the energy of electrons from a sample, these electrons must escape from the sample to the detector. The excitation X-rays can penetrate a significant distance (microns) into the sample, depending on its density, exciting electrons from the bulk of the sample. However, these electrons are very unlikely to make it to the surface of the sample without undergoing some form of inelastic collision and being, either, reabsorbed by the sample or emitted as a component of the background 'noise' in the spectra. Only atoms in the surface 1-10 nm of the sample will emit photoelectrons that are able to escape the sample surface unperturbed. This makes XPS a very surface sensitive technique, ideal for studying the effects that electrochemical processes have on surfaces.

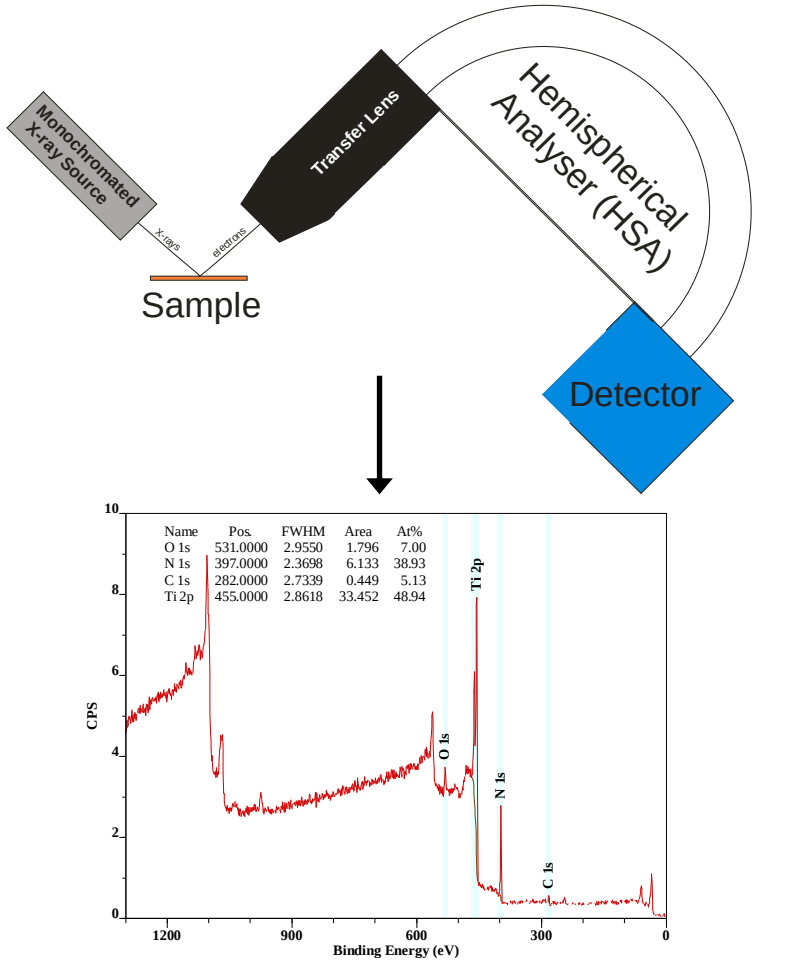

Figure 12: A basic schematic of an XPS instrument and an example of a 'survey scan'.

A monochromated X-ray source illuminates the sample with a known energy of X-rays, ejecting electrons from the sample via the photoelectron effect at energies characteristic of the elements in the sample surface. A survey scan will give a good indication of the relative concentrations of atoms at the surface as shown above, more detailed scans of the elemental regions will give an idea of the environments that those elements are in.

XPS data was collected by the author with assistance from Andrew Hector, Daniel Law, Imran Shah and Moritz Foelsing at NCESS, Daresbury on a Scienta ESCA300 spectrometer. This instrument is fitted with a rotating anode aluminium (Kα) source, operating at 200 mA and 14 kV, the analysis chamber is held under high vacuum between 10^{-10} and 10^{-9} mbar. Samples were introduced into the analysis chamber via a lock/load chamber; Ar ion etching was conducted in this chamber. Spectra were collected based on the species observed in a 'survey' scan of the sample over the available energy range. Regions from this range were selected over which to perform more detailed scans. Typically, these were around the region expected to be associated with emissions from the 2p energy ranges of the native metal in the nitride (Ti or V)

and those associated with 1p emissions from oxygen, carbon and nitrogen. The samples were generally in the form of conductive, nitrided metal foils (Ti and V). For the analysis of non- or poorly conducting powder samples, a charge compensating mask was used in conjunction with an electron floodgun operating between 3 and 5 eV, depending on the requirement of the individual sample.

All data analysis and peak fitting was performed using CasaXPS version 2.3.15 using an iterative method to construct a model of the etched, untreated, metal nitride spectra. This model was then transferred to the oxide species containing spectra and oxide environments that adhered to simple chemical rules in a rocksalt structure were added sequentially to achieve the best fit to the collected data, as determined by the R value of the peak fit. This oxide containing spectra was then transferred back to the nitride surface and the compositions of the surfaces determined from the relative percentages obtained from those peak models. The spectra were fitted with a Shirley type background. $2p_{1/2}$ peaks were constrained to half of the intensity of the $2p_{3/2}$ peak and between 5-9 eV of the $2p_{3/2}$ peak position. The shape of the $2p_{1/2}$ peaks was constrained by setting the FWHM of them to + 0.65 eV wider than their paired $2p_{3/2}$ peaks. Spectra were referenced to carbon 1s at 284.8 eV or the Ar $2s_{3/2}$ peak at 241.6 eV where carbon 1s was not present, usually after etching. All etching was performed using Ar^+ ion bombardment at 4 keV.

2.3.8 Grazing incidence X-ray diffraction.

Grazing incidence X-ray diffraction (XRD) is used for analysis of thin films in preference to normal powder X-ray techniques, as the incident angle of the X-rays allows for more of the sample to be analysed in preference to the substrate. As X-rays penetrate into material a fixed distance depending on the density of the material and the sample, lowering the incident angle means that more of this penetration distance is contained within the surface film of the sample (Figure 13). This can be achieved in several ways: The X-ray source must be placed at a low angle relative to the sample surface, the diffracted X-rays can be detected by a static area detector or by a mobile 2D detector rotated through the 2 θ range.

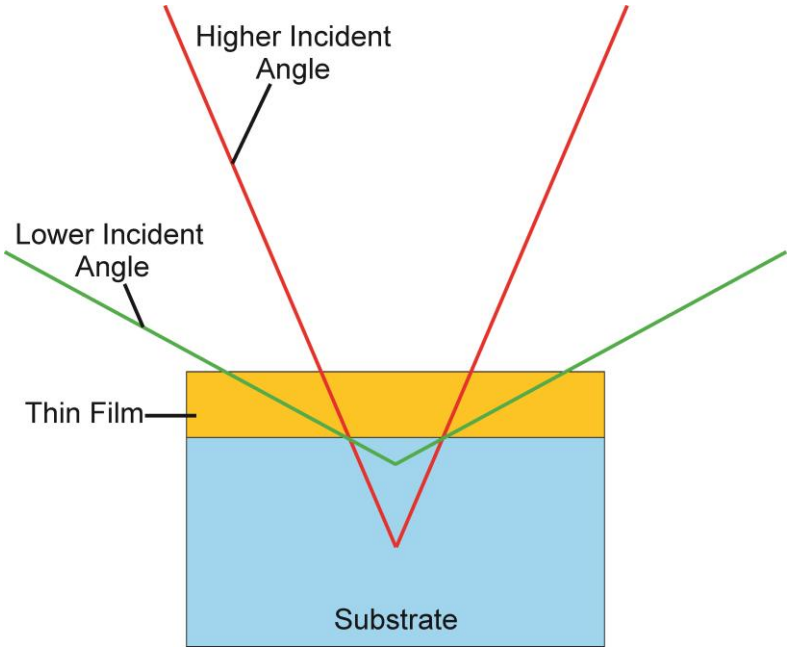

Figure 13: A diagram showing how the incident angle of X-rays affects the penetration depth.

The red line penetrates further into the substrate, meaning a higher proportion of the diffracted X-rays are returned by the substrate when compared to the lower incident angle green line.

2.3.8.1 Bruker C2 diffractometer

The C2 instrument allows grazing incidence to be performed as the area detector and X-ray tube can be set in an asymmetric geometry (Figure 14) with the X-ray source (tube) set at low incidence angles and the area detector aligned to intersect where the diffraction maxima are expected to be.

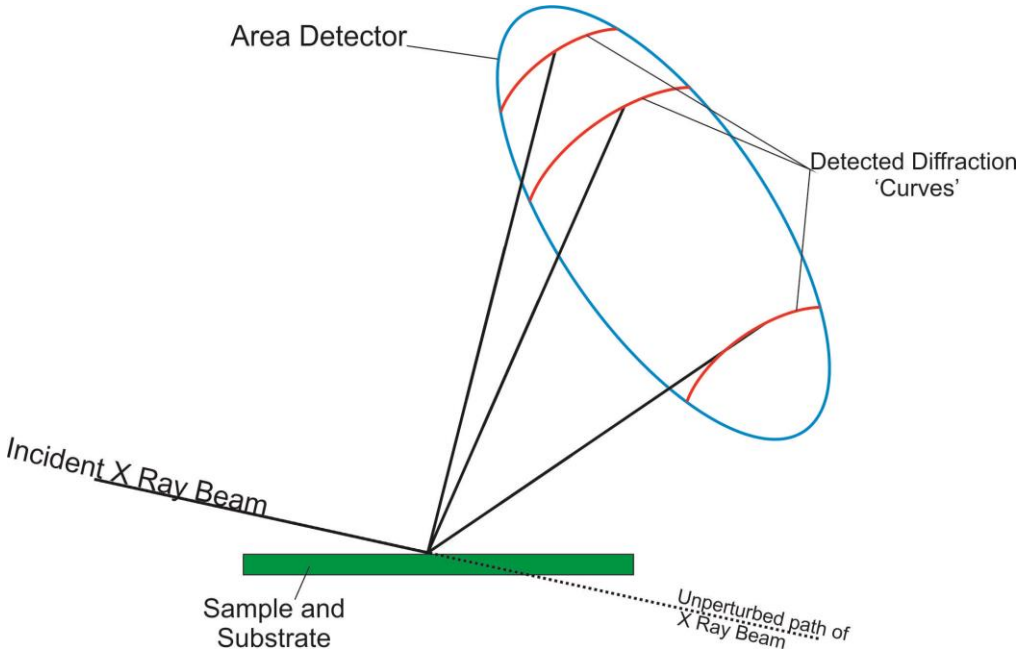

Figure 14: A diagram illustrating the setup of the 'C2' diffraction system in asymmetric geometry.

The incident angle can be set by altering the tube geometry relative to the sample surface. In principle this could be set to a fraction of a degree, however, in practice this is limited to 1˚ as the 0.5 mm parallel beam is elongated across the sample surface excessively at narrower incident angles.

This can be problematic if the peaks desired for phase identification occur at high angles, as the asymmetric geometry and physical set up of the instrument limit the range over which 2θ values can be recorded. The three reflections easily observable on the C2 instrument for VN appear at around 38° (111), 44.5° (200) and 64° (220).[64] Observation of the next two higher 2 θ reflections (76° (220) and 81° (310/222) is impossible on the C2 owing to the range of 2 θ values available on the area detector at such low incident angles. Furthermore, a very long sample, approximately 32 mm, would be required to accommodate the spread of the parallel beam at 1° incident angle. There are, however, some advantages to using an area detector. As the area detector generates an intensity map for the detected X-rays, crystal alignments in the sample can be observed and regions where extended crystallinity is present can be interpreted from the image. This intensity map is then integrated giving an X-ray pattern with a more traditional appearance.

Spectra were collected on the C2, equipped with a 0.5 mm parallel beam collimator and collected using Cu $K\alpha_1$ radiation (1.5406 Å) at incident angles of between 1° and 5°. Samples were held in the instrument inside an inert atmosphere holder, which was constructed from a specially shaped piece of acrylic with kapton carefully secured across it to form an air tight, X-ray transparent window. This was used for samples that hadn't previously been exposed to air. All samples were aligned as carefully as possible into the instrument, to achieve the correct sample height, and run for an appropriate length of time, depending on the sample in question. Metal foils were run for no more than 10 minutes each, macroporous films were run for a minimum of 2 hours to give a better signal to noise ratio.

Data collection and processing were performed using Bruker GADDS detector software. Sample identification was conducted using Bruker EVA software and the PDF card library.[65]

2.3.8.2 Smartlab

In order to overcome some of the limitations of the C2, a more 'thin film specialised' diffraction instrument was used where a 1D detector was swept through 2θ values, giving a larger 2θ range. This extended range allowed for sample speciation to be identified with a greater degree of certainty. Other benefits of using this system over the C2 are that it has a much brighter X-ray source so that similar quality data can be collected in a much shorter time or higher quality data can be collected in the same amount of time, and the incident beam is a 0.1 mm line, rather than a 0.5 mm spot. This gives a greatly reduced beam footprint in grazing incidence mode.

The instrument used was a Rigaku Smartlab with a 9 kW rotating anode source. The instrument was outfitted with a parallel beam-line focus and 5° Soller slits on the source and detector. The detector used was a DTex250. Spectra were collected with a variety of incident angles and analysed with PDXL software using the Powder Diffraction File and Crystallography Open Databases (PDF and COD).

Chapter 3: Sol-gel chemistry and charge storage behaviour of TiN, VN and (Ti,V)N.

Parts of this work were conducted with Thomas Hitch during his third year research project with my supervision.

3.1 Introduction.

3.1.1 Transition metal nitrides.

Transition metal nitrides (TMN's) have a wide range of useful properties, from high conductivity, excellent corrosion resistance, good refractory properties, good hardness and wear resistance to good dielectric properties[19, 66-68]. (Sections 1.7 and 1.8)

TMN's can be synthesised in a number of ways. They are usually synthesised as powders, which are then difficult to process further owing to high melting and sintering temperatures due to the strength of the M^{n+} and N^{3-} ionic interaction.[43]

One method of synthesis is the use of chemical vapour deposition (CVD) of a suitably volatile metal source, typically the desired metal halide and a nitrogen source, for example, NH_3 or hydrazine, onto a heated substrate[69, 70]. CVD is capable of making dense, high quality films and coating complex morphologies. Problems can arise with this when a delicate substrate is employed as the high temperature required for ideal TiN coatings[71] can lead to the degradation of the substrate. The use of metal halides in the CVD process can lead to the incorporation of those halides into the film, potentially leading to a detrimental change in the performance of the device. This can be mitigated by using non-halide metal precursors.[45]

Related to CVD is Atomic Layer Deposition (ALD). This method uses pulses of reactive gases over a heated substrate to deposit single atomic layers. Generally, this is performed by depositing layers of the desired elements in the material, rather than layers of the desired material itself. In the case of VN, this would be as a layer of vanadium, e.g. from a vanadium chloride or amide, and a layer of nitrogen, e.g. from NH_3. This can present problems with forming

the desired species at the surface if the precursors used are not selected very carefully. Whilst ALD can be used to create an inverse opal structure and this has been done in the past[48], doing so is a very slow process unsuitable for constructing the vast number of these structures that would be required to meet the global energy demand.

A further method for the preparation of TMN's is the nitridation of the appropriate metal oxide, for example, heating Ta_2O_5 under flowing, dry NH_3 to produce Ta_3N_5.[72] ZrN thin films have been prepared from a $Zr(O\text{-}iPr)_4$ derived sol[73] coated onto a substrate before heating under NH_3. Nitridation often requires high temperatures, especially for oxophillic metals such as group IV, so encounters the same issue with delicate substrates as CVD. Attempts have been made to convert TiO_2 inverse opal films to TiN[25]. However, the attempt resulted in the collapse of the inverse opal structure, possibly because of the change from the rutile or anatase crystal structure of TiO_2 to a cubic system of TiN. These reasons make conversion of the appropriate oxide into nitride only marginally more suitable to this work than CVD.

Recent work has demonstrated the interconversion between Cr_2O_3 and to $CrTiO_x$ to CrN and CrTiN and the reverse,[74] however, as the possibility of interconversion of VN to VO_x has not been established and TiN to TiO_2 is known to not be possible with the desired inverse opal structure, makes this an undesirable line of enquiry.

With these issues in mind, a sol-gel route (section 1.9 above) was selected as the most appropriate for this project.

Sol-gel chemistry involves the creation of a semi-solid material in solution via condensation reactions. The majority of the research into the mechanisms of their formation has been conducted with alkoxides to produce oxide solids[75] as is outlined in section 1.9. Sol-gel deposition has a good track record for producing high surface area and porous structures in a highly diverse range of morphologies. For this reason, it will be pursued for this project as it is potentially useful for charge storage applications. Whilst mechanistic studies into how sol-gel reactions occur and progress have been conducted, the vast majority of these are performed with silicon alkoxide systems.[75] Very few have been conducted using amide based sols.

Of the amide sol mechanistic studies,[45] similarities have been found between the silicon alkoxide systems and the metal amide ones. The NMR of this study showed that primary amines displace the dimethylamino ligands around the metal centre, with no 'free' H_2NPr visible until more than two molar equivalents were added. As the H_2NPr was not visible, it suggests, when coupled with the increase in the observed viscosity of the sols, that it was incorporated into the structure of a polymeric species resulting in restricted motion and relaxation of the –Pr protons. Above two equivalents of propylamine, it is reasonable to postulate that the majority of the dimethylamino ligands are displaced from the Ti-amide polymer structure, leading to a $[Ti(\mu\text{-}NPr)_x(NHPr)_y(NMe_2)_z]_4$ structure (Figure 15).

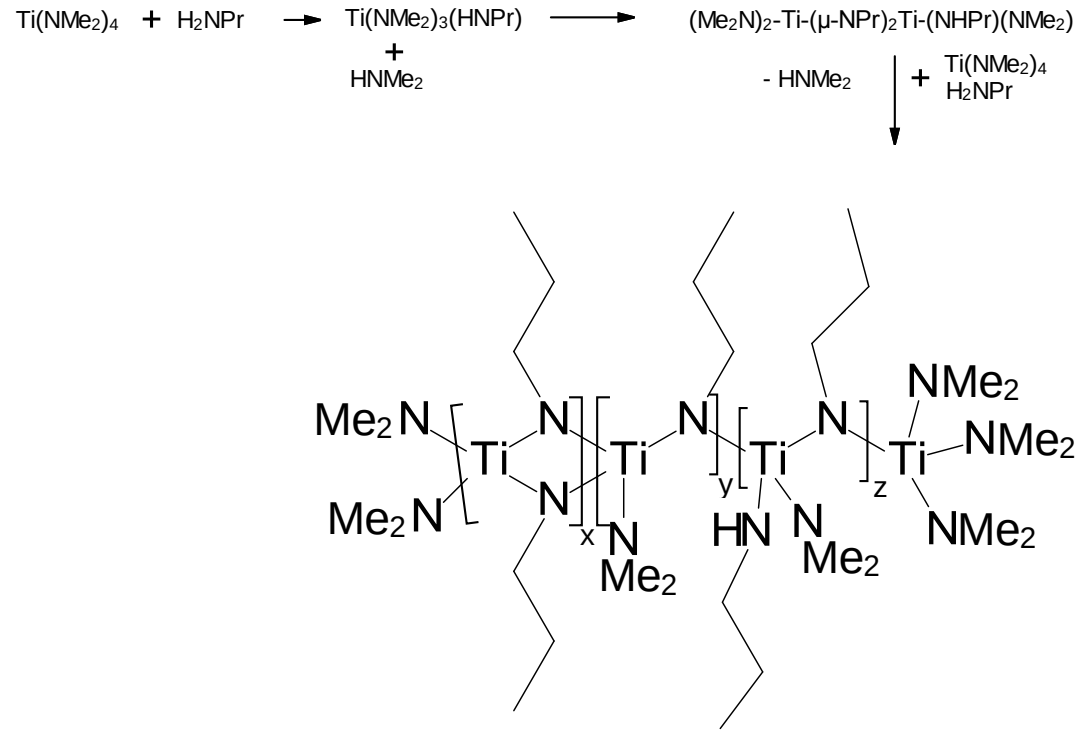

Figure 15: Reaction scheme for the $Ti(NMe_2)_4$ and H_2NPr sol gel reaction forming a Ti-amide gel.

The w, x, y and z monomers in the structure are possible combinations that can occur. The 'W' monomer unit is unlikely as four membered rings are strained and unstable.

Nitride precursor sol-gel chemistry has been developed by several researchers. It was first reported by Bradley *et al*[76] that, on the addition of a primary amine, transition metal dialkylamino compounds could form a metal nitrogen

polymeric structure when attempting to synthesise $Ti_2(NEt_2)_2(\mu\text{-}NPr)_2$ dimers. Instead, this reaction gave $Ti_x(NBu^n)_{(2x-2)-y)}(NEt_2)_y$ (x = 6-14) as a red solid material which 'resisted disproportionation at 130 °C/0.1 mm Hg' (the temperature and pressure at which $Ti(NEt_2)_4$ distils). This approach was further developed within the Hector group, exchanging ammonia for primary amines to prevent the precipitation of the $[Ti(NR_2)]_x$ oligomers and demonstrating that the extra carbon added into the chemical reaction by this ammonia amine exchange was removed by ammonolysis.[45, 46] This reaction produced a sol that could be used to form thin films and, with some minor alteration, infiltrated into templates to produce thin films of TiN exhibiting structured morphologies and minimal carbon contents.[25]

NH_3 can also be used as the cross linking agent in these sol-gel reactions to produce nitride materials. Maya and Brown[77] then Baxter et al[78] heated these $[Ti(NR_2)]_x$ materials identified by Bradley[76], synthesised from ammonia and metal dialkyamides, in ammonia to give TiN solids and films, amongst other metals.

Other materials can be made via sol gel methods such as sulphides[79] and theoretically phosphides[43] could be as well. A considerable amount of research within the group has focused on the use of amide sols to produce useful morphologies in nitride materials.[25, 36, 60, 80, 81] An extension of this would be to synthesise solid solutions of binary metal nitrides.

Binary metal nitrides of TiN and VN show promising supercapacitor performance. However, these have not been examined in a solid solution of TiVN. Core-shell nanoparticle morphologies of a TiN core with a VN shell have demonstrated an improved rate response compared to VN and specific capacities of 170 F g^{-1},[41] compared to 540 F g^{-1} [42] observed using pure VN. Combining the metals more intimately may yield a material with the specific capacity of VN with the rate response of TiVN. Recent work with CrN, another rocksalt structured binary nitride, has led to the production of a CrTiN inverse opal by infiltration of $CrCl_3 \cdot 6H_2O$ and $TiCl_4 \cdot 2THF$ in EtOH solution into a functionalised polystyrene template[74] before annealing under ammonia atmosphere. Solid solution of TiVN have been prepared previously[78] by ammonolysis of the precipitated solids from the reaction of the metal dimethyl amides and ammonia to give a solid with the composition $Ti_{0.32}V_{0.68}N$.

3.1.2 Inverse opals versus suspended particles.

One of the reasons for pursuing an inverse opal morphology is that suspended particles will have an incomplete conduction pathway from the current collecting substrate to the electro active surface of the particles(This can be seen in Figure 9). This is due to the exterior of the electroactive material potentially having higher resistance material surrounding it, for example, aluminium with Al_2O_3. An inverse opal is grown directly onto the substrate, which, in the case of components made from them, must serve as the current collector. This minimises the number of materials that the current must pass through to reach the surface of the electrode, in theory, reducing the resistance of the component.

Current passing through the carbon/VN composite pellet will encounter several different resistances before reaching the redox active surface of the VN particles. The structured film has a much more uniform conduction pathway to the redox active surface. The substrate would ideally be conductive as well to reduce conduction path lengths through the film.

3.1.3 Chapter Aims.

In the work presented in this chapter a sol gel templating approach will be used to generate metal nitrides from an appropriate metal amide sol. The amides synthesised to produce the amide sols will be analysed by IR and NMR to check for purity as well as MA where deemed necessary. The developed sols will be analysed using TGA and XRD to determine a suitable ammonolysis temperature for the transformation into crystalline metal nitrides, as well as by NMR to track the polymerisation reactions to completion. The deposited films will be analysed by SEM, EDX, and XRD to demonstrate that the morphology of the template is preserved through the ammonolysis process and assess the composition of the films produced.

3.2 Experimental.

3.2.1 General remarks.

Owing to the highly air and moisture sensitive nature of the reaction intermediates and some of the starting materials, all reactions were carried out under inert atmosphere conditions using standard Schlenk line techniques with N_2 (BOC) as the inert atmosphere unless otherwise specified, using dry solvents and in an N_2 filled glove box where necessary (O_2 <5 ppm, H_2O <1 ppm). Solvents used were distilled over sodium/benzophenone or barium oxide as appropriate for the solvent in question.

3.2.2 $LiNEt_2$ synthesis.

Into an RBF (1L, 3 necked) chilled with an ice/salt bath, butyl lithium (BuLi, 1.6M in hexanes, ~500ml, Aldrich) was carefully cannulated. $HNEt_2$ (85ml, 0.82 mol) was added slowly to avoid violent reaction, via a dropping funnel with stirring. The drops of $HNEt_2$ went from clear and colourless to milky white on contact with the pale yellow BuLi solution.

Once the addition was complete, the solution was stirred whilst being allowed to warm to room temperature before being filtered through a large filter frit. This yielded a white solid. The isolated solid was dried under vacuum for four hours before being collected (53.1g, 84%). The filtrate was disposed of as per 1.6M BuLi as it still exhibited considerable reactivity towards protic solvents.

3.2.3 $LiNMe_2$ synthesis.

Into an RBF (1L, three necked) chilled with an ice/salt bath BuLi (1.6M in hexanes, ~300ml, Aldrich) was carefully cannulated and left to chill (~30 mins) with stirring. $HNMe_2$ (Aldrich) was then carefully blown into the surface depression of the reaction caused by stirring the solution rapidly. Care was taken not to cause any splashes of BuLi onto the needle that might cause it to become blocked. The places where the gas and the cold BuLi solution contacted formed a milky precipitation at first, followed by distinct lumps of white solid material. The $HNMe_2$ gas was allowed to pass over the BuLi solution for ~45 minutes until no further precipitation was observed. The

$HNMe_2$ gas flow was then stopped and the milky white solution allowed to warm to room temperature before the solution was filtered and the resulting white solid dried. The frit was then sealed and transferred to the glovebox before the solid was collected. Yield 40.1g, 98%. The filtrate was disposed of as 1.6M BuLi.

3.2.4 $V(NMe_2)_4$ (tetrakis dimethylamino-vanadium(IV)) synthesis from VCl_4 and $LiNMe_2$.

A literature route [61] was modified to optimise yield of recoverable $V(NMe_2)_4$

In the glovebox, a 3 neck 1L round bottom flask (RBF) was charged with lithium dimethylamide ($LiNMe_2$, 11.17 g, 0.22 mol) and a large stirrer bar, before being fitted with a condenser, a subaseal and a dropping funnel (300 ml). This was then removed from the glovebox, carefully secured to the framework in the fume cupboard and connected to a Schlenk line (Ar) over a water/ice/salt bath on a stirrer hotplate. Dry Et_2O (150 ml) was added with stirring such that the $LiNMe_2$ was fully suspended giving a milky white solution. Whilst this was stirring, dry benzene (40 ml) was delivered into the dropping funnel, with the valve closed, via a subaseal. Vanadium tetrachloride (VCl_4, 4.85 ml, 0.045 mol) was added to the C_6H_6 in the dropping funnel producing a dark red/brown solution. A further portion of C_6H_6 (10 ml) was used to wash the VCl_4 from the side of the dropping funnel. Once the $LiNMe_2$ was suspended into the Et_2O, the VCl_4 solution was added to the reaction over 30 minutes with the reaction temperature being monitored via a thermometer held against the outside of the RBF in the water bath and vigorous stirring. The rate of addition of VCl_4 was controlled so that the reaction temperature did not rise above 3 ºC. Once the addition had finished the reaction solution was an intense dark green colour. The resulting solution was refluxed (45 ºC) for an hour before the solvent was removed via vacuum distillation. A small amount of dark green coloration was observed in the solvent trap. This was possibly a more volatile and unstable $VCl_{4-x}(NMe_2)_x$ species, although there was insufficient material to isolate and analyse to confirm this). The resulting dark green/black oily material was suspended in benzene (100 ml) and the flask allowed to stand overnight to allow LiCl to precipitate. A large frit with a two neck RBF (1 L) was set up and left under vacuum overnight also.

The condenser was replaced with the refilled frit. The settled solid, a dark green/brown gelatinous material, was decanted from the liquid through the frit to give a very dark green/black solution. This resulting solution was evaporated as far as possible under vacuum to give a dark green black gel.

The gel was vacuum sublimed using a hot air gun and solid carbon dioxide (cardice)/acetone to cool the receiving flask. The sublimation produced large (3-4 mm) very dark green/black diamond shaped plate crystals in the elbow joint of the sublimation set up, these were collected and analysed via IR, NMR and microanalysis. Yield: 3.32g, 32%. IR[61]: Nujol mull, CsI windows, 592 cm^{-1} (s), 944 cm^{-1} (s), 1050 cm^{-1} (m), 1148 cm^{-1} (s), 1244 cm^{-1} (s). NMR: (Figure 16) $CDCl_3$, 300 MHz, 3.45 ppm. MA: Theory C 42.26 %, H 10.64 %, N 24.65 %. Found C 42.11 %, H 10.53 %, N 24.85 %.

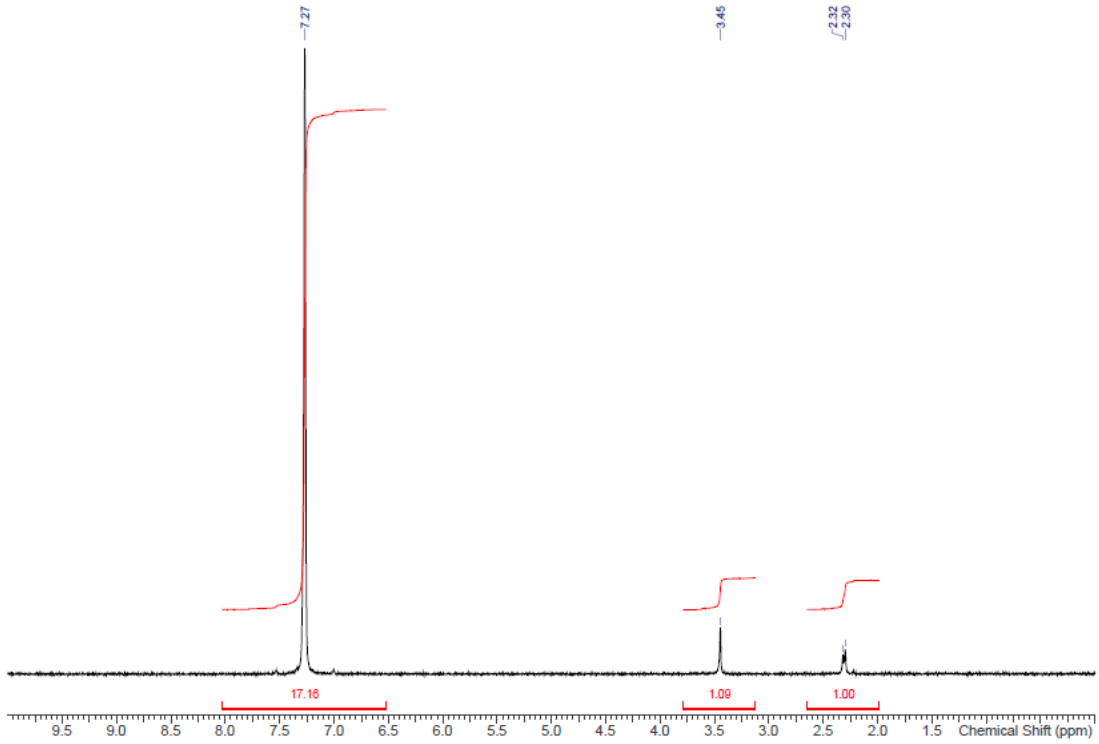

Figure 16: The ^1H NMR spectra of $V(NMe_2)_4$ in $CDCl_3$.

Acquiring a relatively 'clean' spectra of this amide was difficult owing to its reactivity. The large peak at 7.27 ppm is from residual protons on $CDCl_3$. The peak at 3.45 ppm is from the $V(NMe_2)_4$ and the doublet at 2.32 ppm is most likely from $HNMe_2$ generated from the decomposition of the $V(NMe_2)_4$.

A second sublimation was attempted using an oil bath with the aim of gaining an approximate value for the sublimation temperature of the amide. No

material was recovered from this before the maximum temperature of the oil bath on the hotplate was reached.

3.2.5 $V(NEt_2)_4$ (tetrakis diethylamino-vanadium(IV)) synthesis from VCl_4 and $LiNEt_2$.

The literature method used to synthesise $Ti(NEt_2)_4$ [82] was modified to use VCl_4 to produce the vanadium analogue.

In the glovebox $LiNEt_2$ (8 g, 0.11 mol) was measured into an RBF (1 L, 3 neck) and fitted with a stirrer bar before being sealed with two stoppers and a subaseal. The flask was then transferred to a fume cupboard and fitted with a purged dropping funnel and large filter frit. $LiNEt_2$ was dissolved in Et_2O (75 ml) with stirring to give a milky solution. This was cooled with a salt/ice bath to ~0 ºC. Whilst the $LiNEt_2$ solution was cooling, VCl_4 (2.2 ml, 0.02 mol) was suspended in benzene (35 ml) in the dropping funnel before being added slowly into the Et_2O solution. Once the addition was complete the dropping funnel was carefully rinsed with benzene (10 ml). The reaction solution turned green from milky white and remained so once the addition of VCl_4 was complete.

The ice/salt bath was replaced with a water bath and the reaction solution was gently refluxed at 45 ºC for 2 h. The heating was then stopped and the Et_2O removed under vacuum to aid LiCl precipitation. A further portion of benzene (40 ml) was added. The resulting green reaction solution was allowed to stand without stirring for 20 minutes to aid LiCl precipitation before being decanted and filtered carefully through a filter frit.

The resulting dark green solution was reduced in volume without heating as far as possible. The dark green, viscous liquid from this reduction was then purified using short path sublimation with a hot air gun and cardice/acetone. A further sublimation of the crude product yielded material that changed colour from dark green to dark red/brown on warming to room temperature. The desired product was a green-black oily liquid.

Yield: 15.1 g, 59 %. IR: 1153 cm^{-1} (s), 1003 cm^{-1} (s) 612 cm^{-1} (s) (Figure 18). NMR: 1.25 ppm (t), 3.7 ppm (q). The NMR for this compound shows some impurities, exhibiting a range of environments around 0-1 ppm as well as free

diethylamine. Owing to time constraints it was decided to use the product anyway. The use of carbon based grease in subsequent experiments showed no traces of silicon by EDX.

3.2.6 Synthesis of $Ti(NEt_2)_4$.

This preparation has been slightly modified from a literature method[82] where the BuLi and diethylamide were prepared in-situ before the synthesis of the titanium amide.

Previously synthesised $LiNEt_2$ (27 g, 0.341 mol, as per 3.2.2 above) was weighed out in the glovebox and dissolved/suspended into dry Et_2O (240 ml) with stirring and cooling over ice water/salt mix to produce a milky white solution. $TiCl_4$ (9.5 ml, 86 mmol) was suspended in benzene (60 ml) in a dropping funnel and added slowly to the amide solution with vigorous stirring over 30 minutes. The temperature was kept below 5 ºC at all times during the addition by altering the flow rate of $TiCl_4$ into the reaction and periodically stirring the ice water/salt coolant. Once the addition was complete, the dropping funnel was washed with a portion of benzene (20 ml) and the reaction solution was refluxed gently for two hours. Initially, a brown intermediate precipitated during the addition but this dispersed during the reflux to give a bright orange solution with a pale orange precipitate of lithium salts. The ether was removed by evaporation and replaced with an equal volume of benzene before being filtered through a frit to remove the Li salts. The benzene was removed under vacuum. $Ti(NEt_2)_4$ was isolated from the remaining yellow/orange oil by short path sublimation as an oily orange liquid

(Yield: 19.0 g, 65 %. IR: 1152 cm^{-1} (s), 1002 cm^{-1} (s), 609 cm^{-1} (s) (Figure 18). NMR: C_6D_6, 300MHz, 1.25 ppm (t), 3.7 ppm (q). This was transferred into a gas tight container in the glove box for storage.

3.2.7 Formation of metal amide sols by amination.

All four coordinate metal amides were aminated using the same method.

In the glovebox and into a Schlenk tube, $M(NR_2)_4$ (M = V, Ti. R = Me, Et. 11.2 mmol) was weighed out and a magnetic stirrer bar was added. The tube was fitted with a septum and transferred to the Schlenk line before hexane (7.5 ml)

was added with stirring. H_2NPr (1.75 ml, 22.4 mol) was then added slowly and the mixture left stirring under inert atmosphere for 2 (R = Me) or 72 (R = Et) hours to form a black-green viscous liquid.

Portions of these sols were used in two ways: It was infiltrated into a polystyrene template (detailed in section 4.2.3) or it was evaporated to a gel and heated under flowing ammonia to give a black solid.

3.2.8 Nuclear magnetic resonance investigation into $Ti(NEt_2)_4$ sol gel reaction.

Into a Youngs tap NMR tube in the glovebox, $Ti(NEt_2)_4$ (0.55 g (approximately 0.67ml), 1.88 mmol) was added followed by C_6D_6 (1.5 ml) and H_2NPr (0.33 ml, 4 mmol). The tube was tightly sealed before being thoroughly shaken to mix the liquids and transferred from the glovebox to the NMR spectrometer. ^1H NMR spectra were collected once an hour on this sample for 24 hours.

NMR; (Figure 19) C_6D_6, 400 MHz, 'X' minutes, 3.6 ppm (sex) Ti-N-C**H**$_2$CH$_2$CH$_3$, 2.6 ppm (quin) Ti-N-CH$_2$C**H**$_2$CH$_3$, 1.2 ppm (t) Ti---NHCH$_2$-C**H**$_3$, 1.1 ppm (t) Ti-N-CH$_2$CH$_2$C**H**$_3$. TDEAT, 3.7 ppm (q) Ti-NC**H**$_2$-CH$_3$, 1.25 ppm (t) Ti-NCH$_2$-C**H**$_3$. n-Propylamine, 2.55 ppm, (t) H_2N-C**H**$_2$-CH$_2$-CH$_3$, 1.4 ppm (sex) H_2N-CH$_2$-C**H**$_2$-CH$_3$, 0.9 ppm (t) H_2N-CH$_2$-CH$_2$-C**H**$_3$, 0,6 ppm (s) **H**$_2$N-CH$_2$-CH$_2$-CH$_3$. Diethylamine, 2.6 ppm (q) HN-C**H**$_2$-CH$_3$, 1.1 ppm (t) HN-CH$_2$-C**H**$_3$

Following the experiment, the NMR tube was soaked and then rinsed with dry methanol to lower the reactivity of the Ti-amide sol before being decanted and neutralised by slow addition of water.

3.2.9 Preparation of TiN, VN and (Ti,V)N solid solutions.

A range of solid solutions from TiN to VN were prepared with the intended stoichiometry at 0.2 molar intervals ($Ti_{0.8}V_{0.2}N$ etc) as detailed in 3.2.7:

The ratio of $V(NEt_2)_4$ to $Ti(NEt_2)_4$ for each solid solution is in Table 2.

Table 2: The molar ratios of Ti and V diethylamides used to create each solid solution in this chapter.

The liquid amides were syringed out into a pre-weighed syringe and needle, then weighed in the glove box before being added to the reaction Schlenk. This was done as an accurate value for the density of the amide could not be obtained.

Intended molar ratio (Ti:V)	$Ti(NEt_2)_4$ (mmol)	$V(NEt_2)_4$ (mmol)	Ratio of reactants (Ti:V)
100:0	11.3	0	100 : 0
80:20	1.07	2.66	80.1 : 19.9
60:40	6.45	4.53	58.8 : 41.2
40:60	4.49	3.40	41.2 : 58.8
20:80	2.24	8.53	20.8 : 79.2
0:100	0	10.7	0 : 100

3.2.10 High temperature ammonolysis of $M(NR)_x$ gels.

A variety of $M(NR)_x$ materials were heated under ammonia to convert them into the corresponding MN compounds. These include infiltrated inverse opal films (3.2.7) and bulk samples of the $M(NR)_x$ gels (3.2.7) including those from solid solutions (3.2.9).

The solids were heated under flowing anhydrous ammonia, dried by passing through 3 Å molecular sieves, to 600 ºC (2.5 ºC min^{-1} heating rate) to give a range of black powders and films. Films were cooled at a maximum rate of 5 ºC min^{-1}.

3.2.11 Electrochemical evaluation of TiN, VN and (Ti,V)N solid solutions.

In order to assess the electrochemical performance of the prepared solid solutions, the synthesised materials were coated onto titanium metal substrates as 'inks' before electrochemical cycling as detailed in section 2.2.2.

A sample of electrode material (20 mg) was placed into a sample vial with PVDF (2.5 mg) and carbon black (3 mg) before being dissolved/suspended into cyclohexanone (0.2 ml per electrode) by sonication for 10 minutes. Titanium metal was cut into substrates (10 x 15 mm) and one side of each was cleaned and roughened with fine (800 grit) sand paper. These were cleaned and degreased by sequential sonications and rinsing in acetone and water, blown dry with a stream of dry nitrogen and left on a clean piece of tissue paper and allowed to stand for several hours until completely dry. The electrode substrates were carefully weighed before being coated with the solid solution suspension. This was added to the substrate dropwise, allowing each drop to evaporate before the next was added. Once the final drop was dry the electrode was reweighed before being individually stored ready for cycling. This resulted in a powdery black residue across the roughened area of the substrate with a visually even distribution.

3.3 Discussion of the preparation of vanadium amides.

Initially, $V(NMe_2)_4$ was chosen as the target precursor for making VNR_x based sols. This was chosen as the analogous $Ti(NMe_2)_4$ system was known to work reliably under sol-gel processing conditions[45, 83] and using the equipment and procedures currently in practice within the group. $V(NMe_2)_4$ should share many of the properties of $Ti(NMe_2)_4$, in terms of reaction rate and solvent compatibilities, making it an ideal candidate for making (Ti,V)N solid solutions of various compositions. The composition will be controllable by the quantity of the amides added at the start of the sol reactions.

The literature details two preparations for making $V(NMe_2)_4$. The first reported preparation is from Bradley *et al*, using VCl_4 as the starting vanadium source and reacting it with $LiNMe_2$ dissolved in dry Et_2O. This method was chosen to be held in reserve initially, as VCl_4 slowly decomposes at ambient temperatures into Cl_2 and VCl_3[13] over time. The second method, more recently described by Haaland *et al,*[84] uses $VOCl_3$ as the starting vanadium source, reacting this with a $LiNMe_2$/pentane solution. $VOCl_3$ is a more desirable starting material as providing it is stored correctly it does not spontaneously decompose.

3.3.1 Synthesis of $V(NMe_2)_4$ from $VOCl_3$ and $LiNMe_2$.

Despite various iterations and minor alterations, using $VOCl_3$ to synthesise $V(NMe_2)_4$ was not successful. IR scans of the crude products from these reactions (Figure 17) showed promise as they had a peak characteristic of V-N stretches[61] (~1155 cm^{-1}). However, this was not isolated despite multiple attempts. The $V(NMe_2)_4$ is isolated as the volatile product of the reaction. Any oxygen containing species are less volatile and are left behind on sublimation. These oxygen containing species presumably account for significant proportion of the loss in the yield reported for this synthesis (37%).[84]

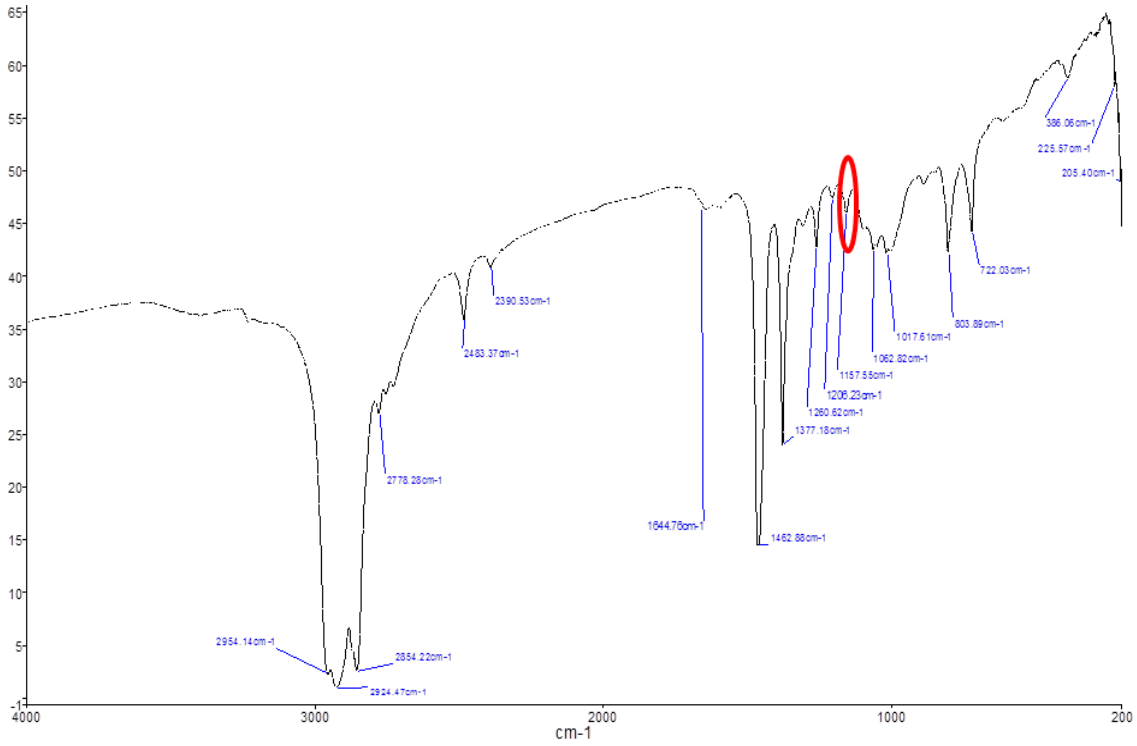

Figure 17: IR of the crude reaction products from a $VOCl_3$ and $LiNMe_2$.

The red ringed peak at 1157 cm^{-1} is indicative of a VN-C bond, suggesting a species containing this motif was present in all the preparations.

3.3.2 Synthesis of $M(NEt_2)_4$ from MCl_4 and $LiNEt_2$.

After the unsuccessful attempts to make $V(NMe_2)_4$ from $VOCl_3$, it was decided to try the alternate method for preparing $V(NMe_2)_4$, described by Bradley.[61] The methyl amides tend to be the most reactive of their family,[13] due to the higher entropic gain associated with their decomposition, owing to $HNMe_2$ being gaseous at room temperature, and a sterically less hindered structure when

compared to more massive and less volatile diamines. Hence the diethyl amide was targeted. Ethyl groups are also able to undergo beta elimination processes and so be just as effective as starting materials for sol-gel processing.

This method uses VCl_4 as the starting V source. VCl_4 is less pleasant to work with than $VOCl_3$. It needs to be kept cold and in the dark to prevent it from decomposing into solid V^{III} [13, 85] species and Cl_2. On contact with air, VCl_4 releases large plumes of HCl as it reacts with atmospheric water vapour, the solids deposited fuse items together, such as the needle used to extract it from the bottle and the bottle seal. This can occur when transferring the syringe from the bottle to the reaction flask, blocking the needle. Speed and impeccable inert atmosphere techniques must be exercised when handling this reagent. It is also toxic and the HCl released on contact with airborne moisture makes it corrosive and harmful. Whilst these last two hazards are not restricted to VCl_4 ($VOCl_3$ is also toxic and corrosive), VCl_4 is a d1 species,[85] making it reactive to any minor deviation from its preferred conditions. $V(NEt_2)_4$ was synthesised by the addition of VCl_4 dissolved in benzene into a chilled solution of $LiNEt_2$ in ether as a green-black oil (see 3.2.5 for further experimental details).

$Ti(NEt_2)_4$ was made by a modified literature route.[82] The route details the preparation of BuLi and $LiNEt_2$ in situ before the synthesis of $Ti(NEt_2)_4$. $LiNEt_2$ was prepared separately and suspended in the reaction prior to the addition of $TiCl_4$. This gave the desired product in good yield (3.2.6).

The IR spectra of both compounds look nearly identical (Figure 18). Many of the peaks are from the same bond groups (C-N and C-H stretches from the diethylamine groups), the only bond that differs between the two compounds should be the M-N bond, V-N should display a higher wave number (lower frequency) vibration than the Ti-N bond because the Coulombic attraction between the V^{4+} and the N^{-3} atoms will be weaker than those of the Ti^{4+} and N^{-3} owing to the d^1 arrangement of the V centre. This effect is only subtly observed in the spectra with a 3 cm^{-1} difference between the two peak values (609 (TiN) and 612 cm^{-1} (VN)).

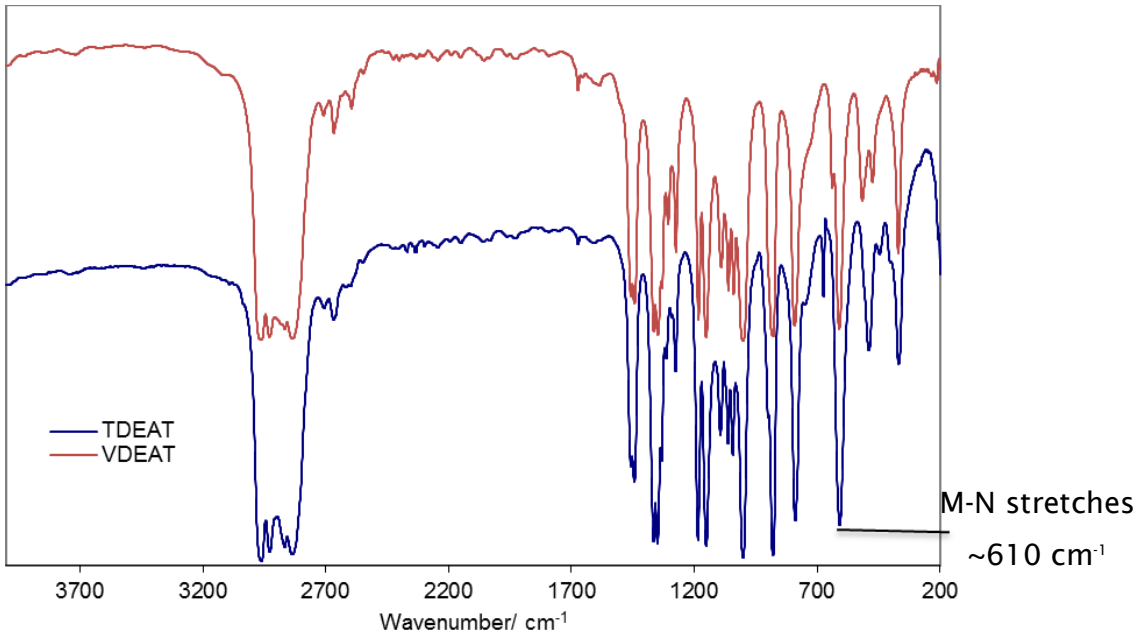

Figure 18: FT-IR spectra of $V(NEt_2)_4$ (red, top) and $Ti(NEt_2)_4$ (blue, bottom), showing the similarities between the two spectra.

The M-N stretch has been highlighted.

3.3.3 Synthesis of $V(NMe_2)_4$ from VCl_4 and $LiNMe_2$.

After the preparation of $V(NEt_2)_4$ was successful another attempt to make $V(NMe_2)_4$ was made, with lessons learnt from the previous amide preparations informing the procedure. The procedure used to synthesise $V(NMe_2)_4$ was altered to the route described by Bradley[61] with VCl_4 as the starting material and the greatest care taken towards the inert atmosphere technique employed. These reactions proceeded smoothly to produce 1-4 mm, very dark green, diamond plate shaped crystals after sublimation. Analysis by microanalysis, and IR (see 3.2.4 for IR and MA results) showed that the desired amide was produced in a reasonable yield (32%). Losses could have occurred from a range of scenarios, the biggest loss es are likely to be in the isolation of the amide by filtration and distillation/sublimation. Passivating the interior surfaces of the glassware and any trace moisture contained within could also reduce the yield. Another possible area of loss could be from the incomplete substitution of the metal amide leading to the formation of $VCl_{4-x}(NMe_2)_x$ species. These lower molecular weight compounds are expected to be more volatile than the desired $V(NMe_2)_4$, so could explain the small quantity of dark

green material observed to distil over the sublimation apparatus before heating the dried reaction residue.

3.4 Metal amide and propylamine sol-gel chemistry.

$V(NEt_2)_4$ was synthesised as a dark green/black oily liquid by altering a preparation by Bradley[76] for $Ti(NEt_2)_4$ (see 3.2.5 for details). Investigations of this compound showed that it was much slower to react with primary amines than its dimethyl amide counterpart, taking three days to create a suitably viscous solution with no monolith formation observed. This is most likely due to the coordination of $HNEt_2$ to the vanadium centre, blocking the reaction sites and approach angles of the primary amines employed with the large steric bulk of the $HNEt_2$ group.

As $HNEt_2$ has a lone pair of electrons present on the nitrogen, it can act as a coordinating solvent. This would block or slow down the route of nucleophilic substitution by primary amines as the necessary coordination sites around the vanadium would become congested or occupied. As the desired/intended reaction proceeds, the concentration of diethylamine in the reaction vessel increases, further inhibiting the reaction with its high steric bulk. The same could be observed with $HNMe_2$, however, its increased volatility (boiling point = 6 ºC) makes this far less likely to occur at room temperature. The increase in entropy of the system in the $HNMe_2$ changing state from liquid/solvated gas to gas will drive the $HNMe_2$ to evaporate at the ambient temperatures at which the reaction is performed.

The diethylamine could be encouraged to evaporate but requires a more careful set of reaction conditions to be chosen: Diethylamine boils at 55.5 ºC, so to evaporate it from the reaction solution and remove it as an inhibitor as it is produced, the reaction needs to be heated to approaching this temperature, if not slightly above it. Hexane and propylamine boil at 68 and 48 ºC, respectively, so are not suitable for reaction conditions that will force the evaporation of $HNEt_2$ and encourage the polymerisation of the vanadium diethyl amide. Amines and hydrocarbon solvents with longer carbon backbones, having boiling points in excess of 65 ºC should be used, such as hexylamine (bp: 131.5 ºC) and octane (bp: 125.5 ºC).

The $V(NEt_2)_4$ produced was used to prepare solid solutions of Ti/VN materials as detailed in section 3.2.9.

As the reactivity of the vanadium amides is similar to that of the analogous titanium amides, the logical starting point for this investigation was to employ the same conditions as used previously[25] to synthesise a suitable sol for inverse opals; RT, propylamine, hexane solvent, stirring and inert atmosphere, two hours gelation time before infiltration.

These conditions were employed and form a very dark green starting solution of $V(NMe_2)_4$ in hexane. A near black, slightly viscous solution was made on the addition of propylamine and after two hours gelation time, infiltrated into a template and the remainder reduced to a near black gelatinous solid.

3.4.1 NMR study of $Ti(NEt_2)_4$ and H_2NPr sol formation.

The reaction between $Ti(NMe_2)_4$ and H_2NPr has been tracked previously. The reactivity difference between the dimethyl and diethyl amides of the same metal species is not inconsiderable, meaning that the monitoring of the reaction between $Ti(NEt_2)_4$ and n-propylamine could be conducted 'in-situ' instead of by stepwise additions of propylamine. In contrast to the methods employed for the methyl amides, this reaction was conducted in an NMR tube fitted with a Youngs tap. This meant that the whole reaction could be monitored instead of a range of proportions of propylamine being added to separate samples. Additionally, the larger diameter tube (10 mm vs 5 mm) meant that the volumes of each reagent employed could be measured more accurately. The reaction is slowed by the liquid $HNEt_2$ by-product produced. However, the lower pressure increase as the reaction progressed meant that the samples were safe to leave in the spectrometer, again allowing the spectrometer to be left to run the sample over an extended period of time.

One possible problem could have been the production of $HNEt_2$, as discussed above (3.4). In the case of dimethyl amide the loss of the volatile dimethylamine by-product drives the equilibrium of the reaction towards substitution of dimethylamide groups. Diethylamine boils at 67 °C and so this mechanism will not operate unless the reaction is heated. Hence reactions of $Ti(NEt_2)_4$ with a primary amine would proceed more slowly than with $Ti(NMe_2)_4$.

As $HNEt_2$ is a co-ordinating species, it could possibly co-ordinate with the metal centre and blocking reaction sites, slowing the reaction.

The NMR (Figure 19) shows that after 780 minutes (13 hours), the reaction gelled and stopped being a free flowing liquid. This can be seen as the peaks broadening and the multiplet patterns being lost (top spectrum, 780 minutes). There is no $HNEt_2$ visible in the NMR spectra, either, dissolved into the solvent or coordinated to the Ti centre. Through the course of the reaction, the integral of Ti-NEt_2 protons (peak at 1.35 ppm) decreases in relationship to those from the N-C-C-CH_3 protons (1.1 ppm). This shows that, as the reaction progresses, the diethyl amide groups are displaced, presumably, by the propylamine groups.

This shows, as previously found with $Ti(NMe_2)_4$, that the ideal number of equivalents of primary amine to amide is 2:1. Whilst it should theoretically be possible to see $HNEt_2$ both free and coordinated to the Ti centre on the spectra, it is not present.

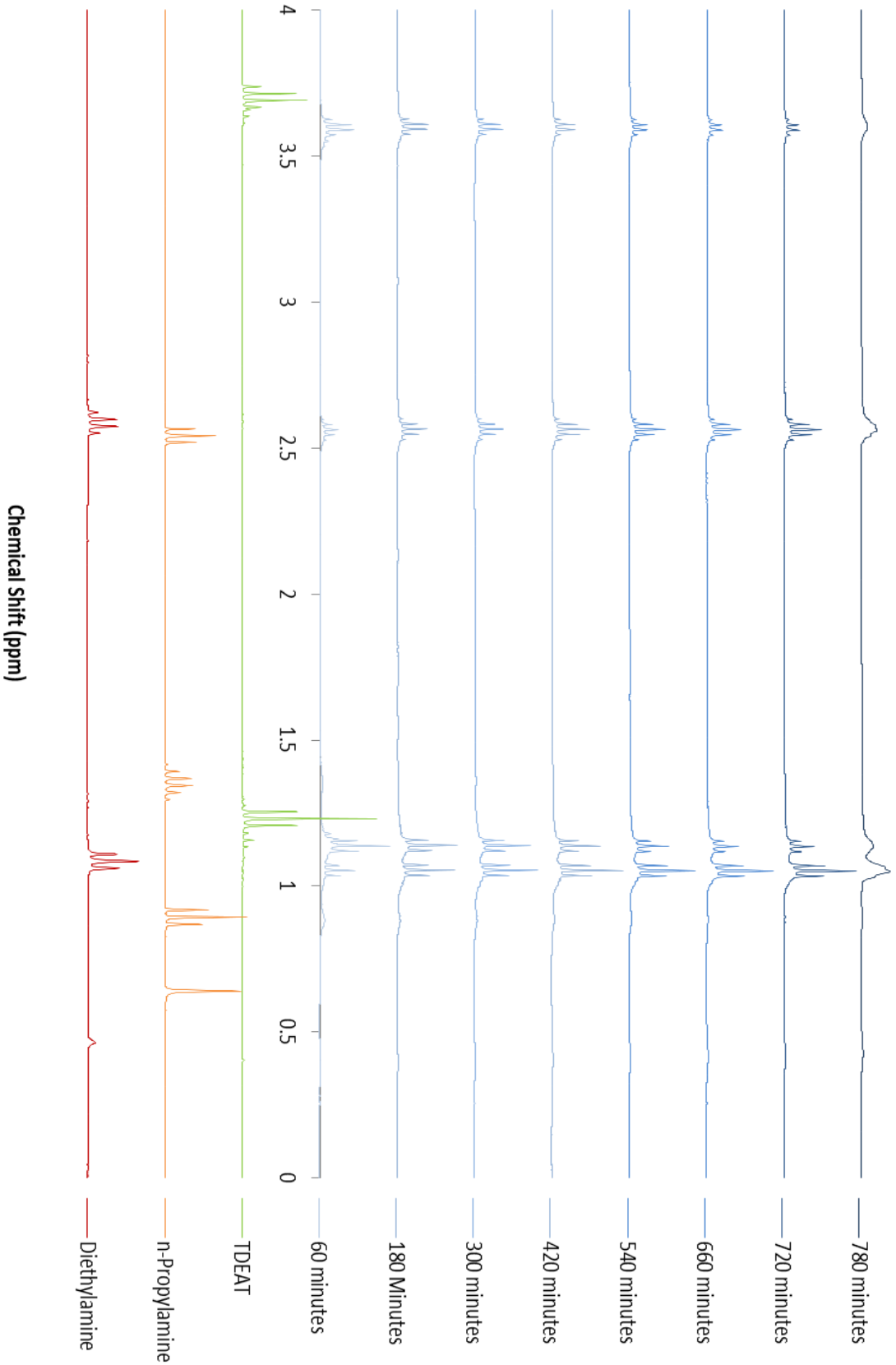

Figure 19: 400 MHz ^{1}H NMR in C_6D_6 following the reaction between $Ti(NEt_2)_4$ and H_2NPr over a 15 hour period at room temperature. Peak assignments can be found in section 3.2.8.

3.5 Sol-gel preparation of TiN, VN and (Ti,V)N powders.

Mixed metal amide solutions were reacted with n-propylamine to give mixed metal amide sols (3.2.9). All of these sols, which contained vanadium amide, were black in colour.

Portions of $V(NEt_2)_4$ and $Ti(NEt_2)_4$ were reacted together with propylamine in hexane to give a series of $(Ti,V)NR_x$ gels. The addition of $V(NEt_2)_4$ to the reactions turned the solution near black even at the lowest concentrations used. The orange of the $Ti(NEt_2)_4$ was not visible in any of the mixed reaction sols. All these solutions were reduced down to give black gels.

Owing to difficulties accurately weighing the diethyl amides inside the glovebox, the solid solutions were synthesised as accurately as possible according to the idealised values desired (Table 3) and the actual compositions determined by EDX afterwards.

The prepared solutions were stirred before evaporating the THF solvent to give a dark gel material. In the cases where the starting solution contained, vanadium the gel appeared black. The pure TiN gel was blood red.

3.5.1 Characterisation of TiN, VN and (Ti,V)N powders.

3.5.1.1 Infra-red.

IR analysis of the synthesised powders showed that the products from the ammonolysis were almost IR silent (Figure 20). This occurs because M-N stretches in metal nitrides are difficult to see as the MN material reflects infra-red radiation before the sample absorbs enough energy for the sample excitation to be visible. The spectra show some peaks in the region associated with N-H stretches (2900 cm^{-1}). This was expected as the synthesis temperature of the solid solutions (550 ºC) is below that of the temperature at which TiN has been shown to form from Ti-amide sols[83] (600 ºC). It was also expected that as the Ti content of the solid increased, the intensity of these stretches would increase, but this isn't the case. The other peak visible on all the spectra at ~2350 cm^{-1} is from CO_2.

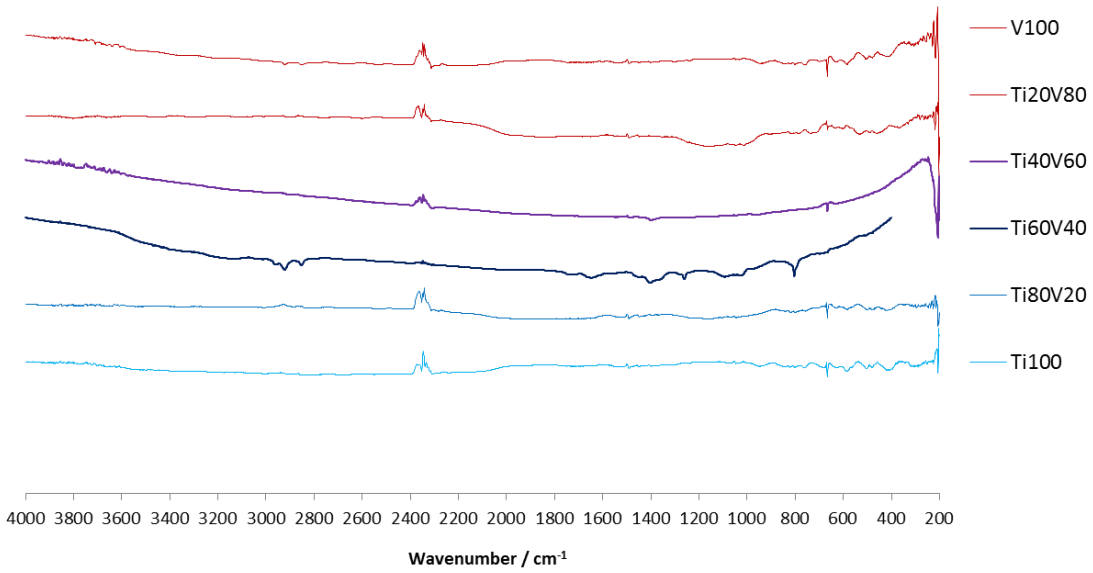

Figure 20: IR analysis of the synthesised solid solutions.

VN is the dark red line (V100), the top spectrum. TiN is the light blue line (Ti100), the lowest spectra. The other compositions, at ~20 % atomic intervals are shown in order of increasing vanadium content to VN (V100). The peaks at around 2350 cm^{-1} are from CO_2, there is also a possible M-N stretch around 670 cm^{-1}.

3.5.1.2 Energy dispersive X-ray an micro- analysis

EDX (Table 2) analysis of the particles showed that the vanadium containing solids had a trace amount of silicon and chlorine incorporated into them. The silicon was probably incorporated into the $V(NEt_2)_4$ during the synthesis from the silicone joint grease used to give an air tight seal between the glassware parts. This grease melts at a relatively low temperature and so during the sublimation, when heat was applied to the glass elbow, excess grease forced from between the joint would have dripped into the receiving flask and been incorporated into the isolated $V(NEt_2)_4$. On ammonolysis this would have turned into a silicon oxide/oxy-nitride/nitride[86] material and been incorporated into the solid.

The silicon contaminant visible in Figure 21 is present in all materials prepared using the $V(NEt_2)_4$ and is present at around 1%.

MA, performed by Medac Ltd using a combustion method with WO_3 oxidiser added, of the solid solutions shows that the carbon content is low as is the hydrogen content. There is still some hydrogen present in the samples that contain the most Ti, however, this can be explained by TiN requiring a higher formation temperature, meaning that the removal of these unwanted atoms is more difficult under the conditions employed. The microanalysis (MA) of the compounds shows that ternary titanium vanadium nitrides can be prepared by sol-gel methods with a low carbon and hydrogen content at 600 °C.

Table 3: CHN microanalysis results for the prepared (Ti,V)N solid solutions showing the atomic % opf each element found in the sample.

All results are to 2 dp.

Titanium content	C Theory	C Found	H Theory	H Found	N Theory	N Found
1	-	0.91	-	<0.10	21.57	20.95
0.8	-	<0.10	-	<0.10	21.77	21.20
0.6	-	<0.10	-	<0.10	21.98	20.65
0.4	-	0.96	-	0.80	22.20	20.33
0.2	-	<0.10	-	0.83	22.41	19.12
0	-	<0.10	-	0.95	22.64	18.93

The MA also shows that the highest carbon content leads to the lowest nitrogen content, suggesting that any carbon incorporated into the structure is present on the anion sites in the rocksalt structure.

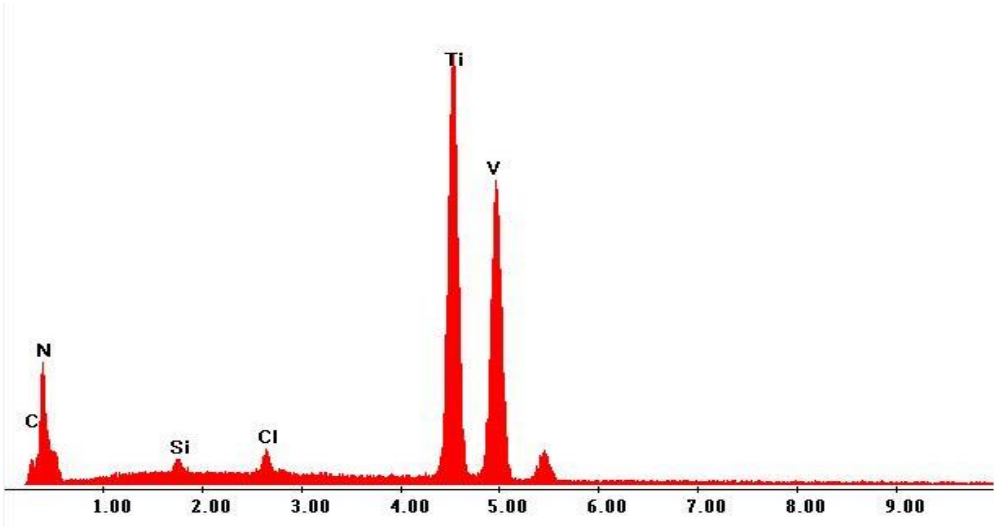

Figure 21: EDX analysis of the $V_{0.4}Ti_{0.6}N$ solid, showing the trace amounts of Si and Cl in the solid solutions.

The amounts of Cl and Si were discounted from the total atomic % of the samples.

EDX analysis of the solids suggests that the compounds contain a small amount of Si and Cl in addition to the expected V, Ti and N. This could account for the low conductivity fine solid observed in the SEM (Figure 22).

The EDX analysis showed that, with the exception of one of the solid solutions (0.8), the vanadium contents of the produced solids were all low compared to what was intended (Table 4).

Table 4: Intended vs observed V content by EDX of the solid solutions.

Results are given to 1 dp and are atomic % of the sample

Intended V content	V content from EDX
100	100
80	82.5
60	51.5
40	36.1
20	15.0
0	

This suggests that the vanadium amide is not pure and is supported by the residual elements observed in EDX (Si and Cl). Plotting these observed V contents against the lattice parameters produces a clearer picture of how the lattice parameter varies with the change in vanadium content (Figure 24).

3.5.1.3 Scanning electron microscopy

SEM of the solid solution materials showed that they were small solid particles.

The small polyhedral particles in Figure 22 are composed of metal nitride, the lower conductivity (brighter) particles visible around the nitride polyhedral are most likely silicates or ammonium chloride as evidenced by the other elements observed in the EDX.

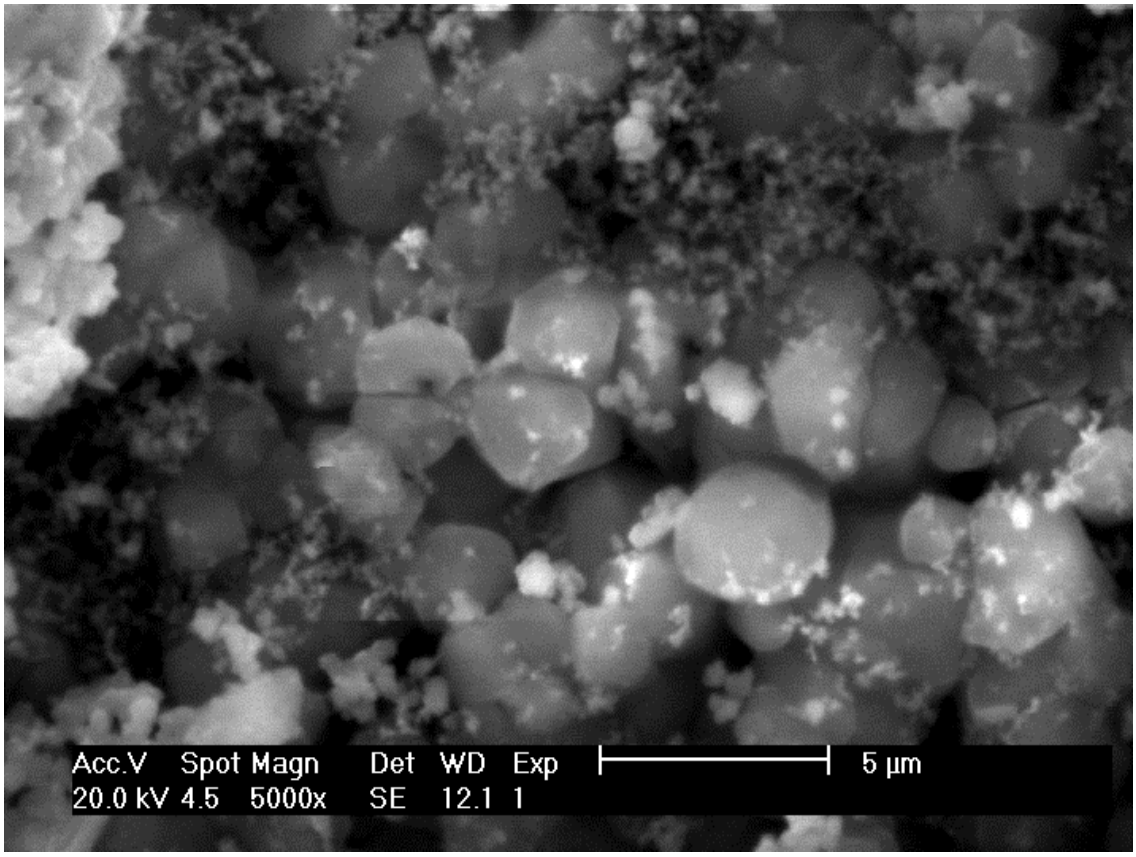

Figure 22: SEM image of the $Ti_{0.6}V_{0.4}N$ material at 20kV under high vacuum at ~5000X magnification.

3.5.1.4 Powder X-ray diffraction.

PXD measurements were conducted on a Bruker D8 diffractometer operating between 20-120 °. This data range was trimmed down to 30-80 ° as the peaks beyond this point were lost into the background scattering of the sample.

PXD of the solids revealed that the materials had formed a rocksalt structure with the observed peaks appearing at smaller 2θ values as the Ti content of the solids increases (Figure 23). Analysis of the patterns gives an approximately linear relationship between the lattice parameter for TiN and VN for the solid solutions, especially when the composition values are adjusted to account for the EDX values (Figure 24).

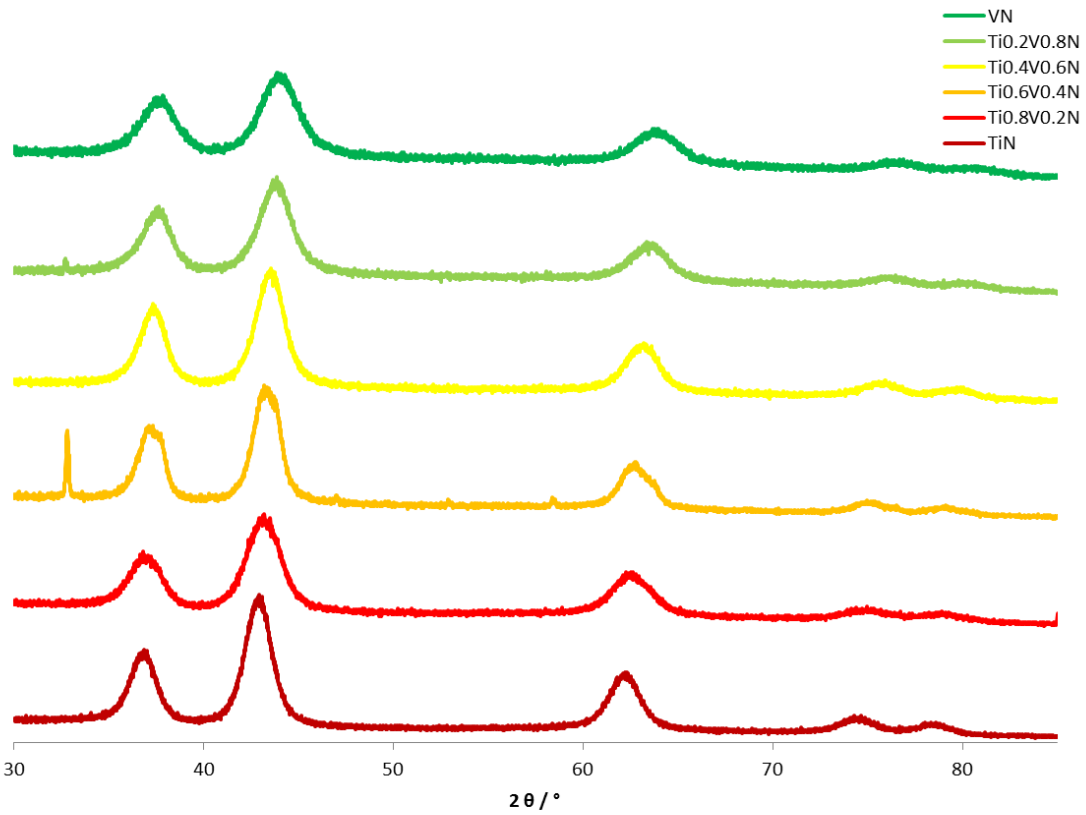

Figure 23: PXD collected from the range of solid solutions, TiN (dark red, lowest spectra) and VN (dark green, highest spectra). The reflections show an increasing 2θ value with increasing V content, indicating that the lattice of the material is shrinking as the vanadium content increases.

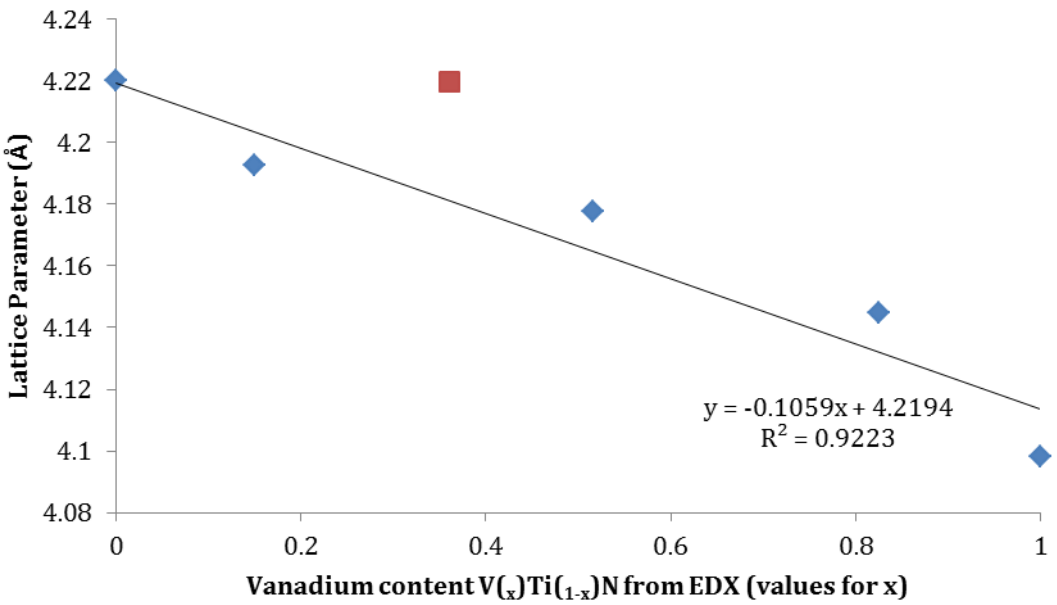

Figure 24: Lattice parameters versus vanadium content of the solid solutions found by EDX.

The red point ($(V_{0.4}Ti_{0.6})N$) has been excluded for the calculation of the line of best fit displayed as a higher than average (for the samples collected here). Si content was observed by EDX.

Figure 23 shows the 2 theta angles of the lattice reflections increasing as the vanadium content of the solid solution is increased.

Figure 24 shows that the lattice parameter of the solid solutions varies linearly within the lattice parameters of TiN (4.22 Å) and VN (4.11 Å) synthesised using the same methods.

The bulk solid materials, prepared as powders from the ammonolysis of the diethylamide sols, were analysed by PXRD on a Bruker D8 diffractometer operating over 20-120 °. No phase separation (e.g. crystals of VN or TiN) were observed where the two amides were used, suggesting that a true solid solution has formed.

Rietveld analysis of the spectra conducted by Tom Hitch and Andrew Hector gave lattice parameters for the materials that shrank as the vanadium content increased Figure 24). This shows, in agreement with the literature[87], that the trend decreases between 4.22 Å and 4.12 Å. Of note is the anomalous reading around 40% vanadium.

3.5.2 Electrochemical evaluation of TiN, VN and (Ti,V)N powders.

The specific capacities calculated, as detailed in 2.2.2, obtained from the cyclic voltammetry (Figure 25) of the solid solutions are plotted in Figure 26. This shows that the composition with the highest specific capacity was $Ti_{0.2}V_{0.8}N$ (Figure 26, Ti20, pale green square), showing a specific capacity of 58.5 μF g^{-1}. This high capacity does not appear consistently across all the scan rates tested with $Ti_{0.2}V_{0.8}N$, however, the observed specific capacity drops very rapidly above 5 mV s^{-1} scan rate in comparison to the other compositions in the study. The composition that displays the highest capacity at higher scan rates is $Ti_{0.6}V_{0.4}N$ (Figure 26, Ti60, orange diamond).

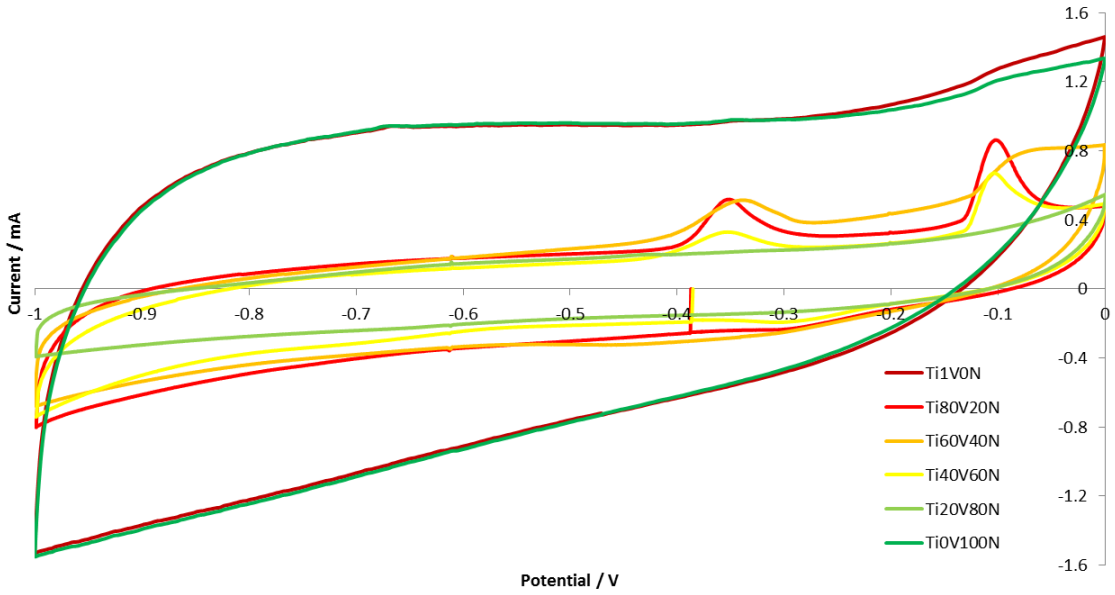

Figure 25: Cyclic voltammagrams of the solid solutions in 1M KOH vs Hg/HgO. All scans are at 1 mV s^{-1}.

There are two oxidation peaks easily visible at around -0.35 V and -0.1 V on the positive sweep, with no obvious peaks on the returning half of the scan, there is a peak at around -0.3 V but it is not of a comparable area. This suggests that a soluble species is formed by this process that is diffusing away from the electrode surface and into the bulk of the electrolyte so is no longer present at the interface to undergo the reverse process required to cause a peak in the current on the negative scan.

The cyclovoltammagrams of all the solid solutions display redox peaks at -0.345 and -0.103 V on the oxidative sweep and -0.294 on the reductive

sweep. This suggests that the surface of the solid solution particles are being oxidised on cycling. Similar reactions of oxidising on cycling have been observed for VN in the literature.[42]

The composition that displayed the best cyclability was VN, exhibiting a 17 % capacity increase over 60 scans. This supports the conclusions of Kumta et al[42] that VN requires some surface oxidation to achieve its highest specific capacitance. None of the titanium containing compositions retained their original capacity throughout the study. The best performance after VN was from TiN, displaying a loss of 13 %. The worst was from $Ti_{0.2}V_{0.8}N$, showing a loss in capacity of 98%. Clearly, this is not an acceptable loss of capacity for a commercial application.

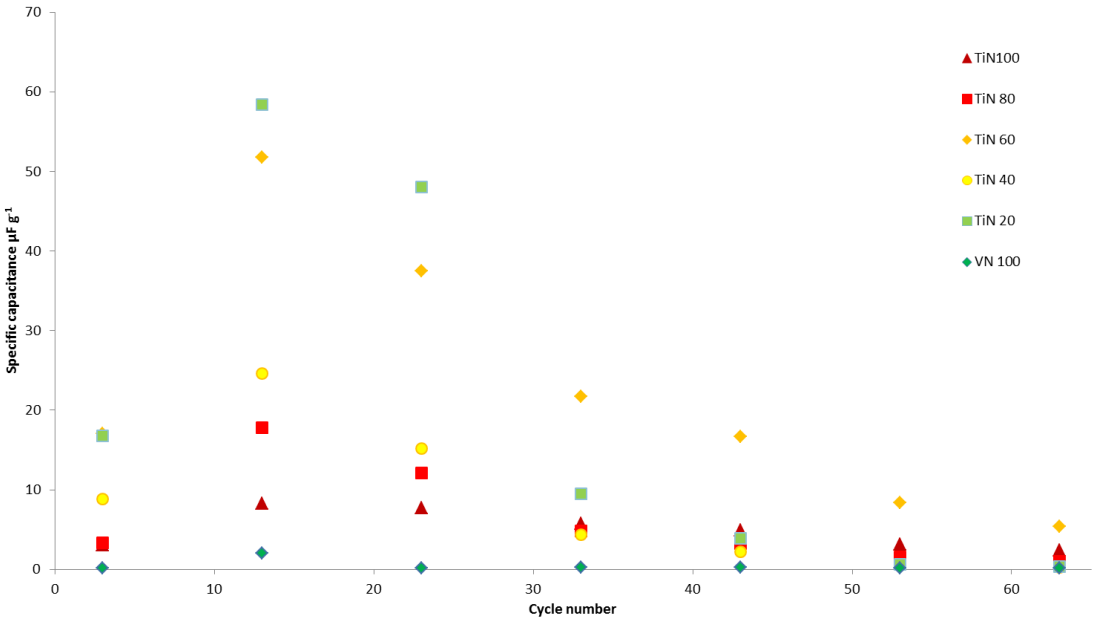

Figure 26: Specific capacitances from the 3rd cycle of each scan rate for the range of solid solutions.

The scan rates used for the study were, in order: 1000 mV s^{-1} (cycle 3), 1 mV s^{-1} (cycle 13), 5 mV s^{-1} (cycle 23), 10 mV s^{-1} (cycle 33), 100 mV s^{-1} (cycle 43), 500 mV s^{-1} (cycle 53), 1000 mV s^{-1}(cycle 63). The cyclability of each material was assessed by comparing the value for the specific capacity for the first 1000 mV s^{-1} scan rate with the last 1000 mV s^{-1} scan rate. The colours displayed for the points on this match the colours used for the cyclovoltammagrams in Figure 25 by composition. The specific capacities were calculated as detailed in 2.2.2.

Table 5: The capacity change of the $V_xTi_{(1-x)}N$ solid solutions over 60 cycles in 1M $KOH_{(aq)}$.

The initial capacity is calculated from the area of the CV trace from the 3rd cycle of the experiments, the after 60 cycles value is found from the areas of the 63rd cycle. This shows that all the surfaces capacities dropped with the exception of VN.

Vanadium content (x)	Specific capacitance ($\mu F\ g^{-1}$)		Capacity change %
	Initial	After 60 cycles	
1	0.16	0.18	117.6
0.8	16.81	0.32	1.9
0.6	8.87	0.28	3.2
0.4	17.05	5.39	31.6
0.2	3.28	1.03	31.3
0	3.06	2.36	77.1

3.6 Sol-gel preparation of TiN and VN inverse opals.

The template used for this infiltration of the V-and Ti amide sol was grown upon a gold-coated substrate to allow for cycling experiments to be conducted on the inverse opal.

Both the infiltrated opal and the black gel were heated, separately, under flowing ammonia to a temperature of 550 ºC for 10 hours, with a cooling rate of no more than 5 ºC min^{-1} employed.

The bulk material and inverse opal prepared from ammonolysis of the gel gave the peaks associated with VN (Figure 23 and Figure 30, dark green lines) and EDX of the bulk material showed a low carbon content (Table 3). This was further supported by the MA of the sample showing low amounts of C and H and an N content indicative of VN.

3.6.1 Characterisation of TiN and VN inverse opals.

3.6.1.1 Scanning electron microscopy

An attempt to synthesise an inverse opal (IO) film of TiN was made using a $Ti(NMe_2)_4$ sol templated around colloidal opal PS templates, using the same sol as had been previously employed for this process in the literature.[25] These

templates exhibit longer range order compared to those used previously within the group[25] (compare Figure 27 and Figure 36). The development of the deposition process leading to these templates was detailed in 2.1.2 and discussed in 4.3.

These templates exhibiting longer range order produced inverse opals with longer range ordering (

Figure 28), showing some cracking produced from thermal cooling of the prepared inverse opal film (Figure 29). This shows that the quality of the template, rather than the heating regime, is the major source of defects in the produced inverse opal structures.

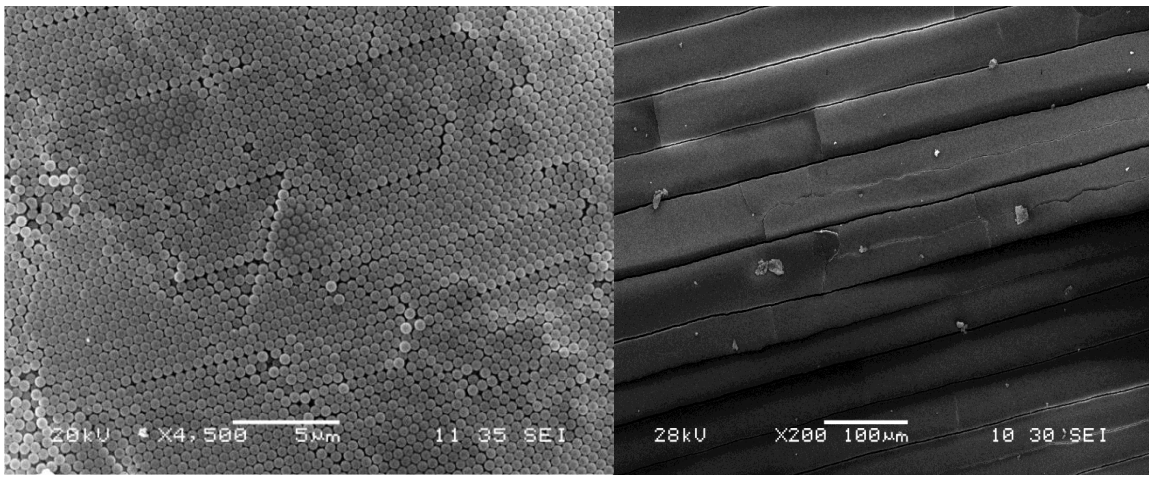

Figure 27: SEM micrographs of 500 nm PS beads deposited onto glass microscope slides at 4500x and 200x magnification, showing the degree of crystallinity in the templates used.

The banding observed in the right hand image is as a result of minor thermal variation during the colloidal deposition and extends the full width of the substrate. It is amplified by drying the PS opals for use with metal amide sols.

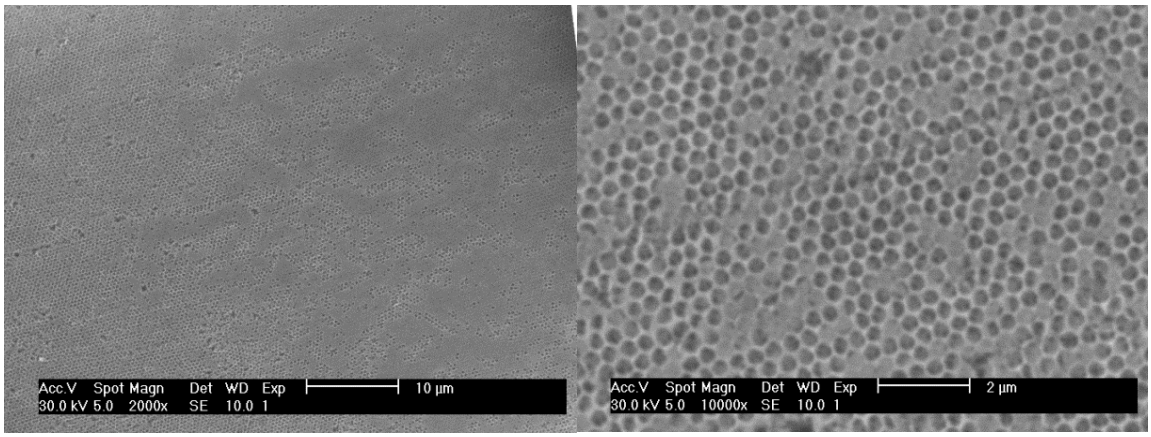

Figure 28: Micrographs of a TiN inverse opal film at 2000x (left) and 10000 x (right) magnification, showing the extent of the ordering.

The left image shows some over infiltration (the sol has coated over the top of part of the template on the right hand edge of the image).

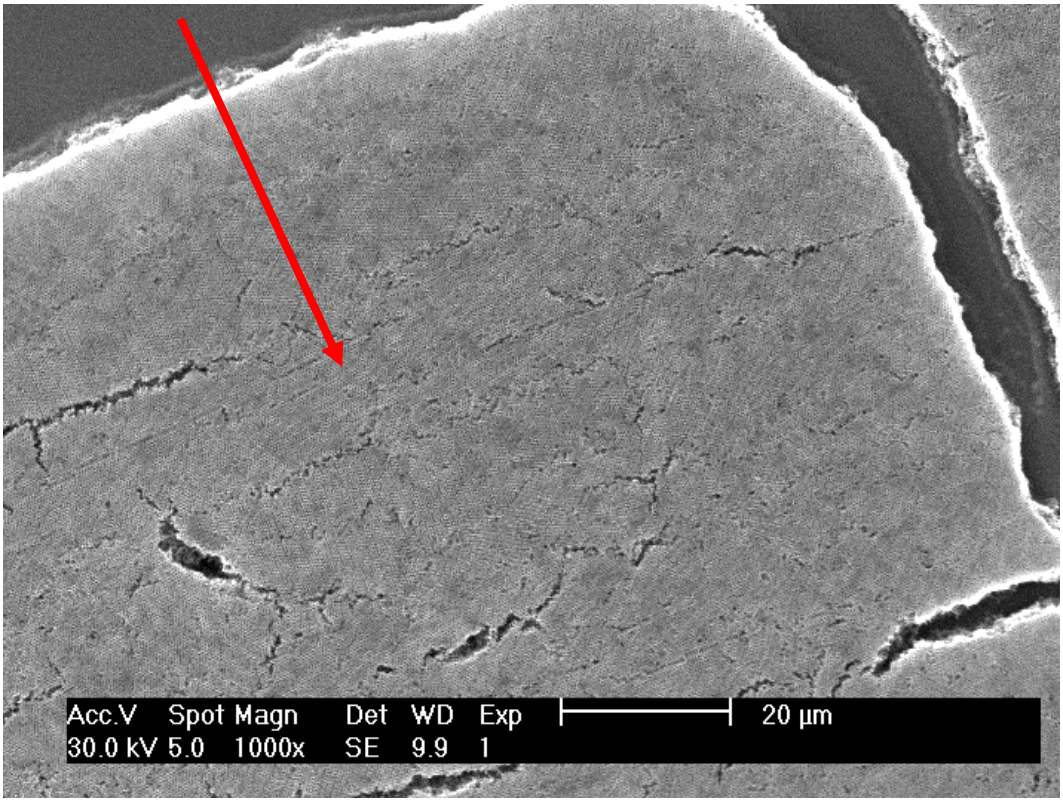

Figure 29: An SEM micrograph showing a section of TiN inverse opal film with more defects and cracks. The arrow shows the direction of template growth.

The inverse opal produced was not without major defects (Figure 29). It exhibited defects from the opal template used where the colloidal beads hadn't deposited properly for whatever reason. These mainly appear as 'full height',

from substrate to surface, cracks perpendicular to the direction of template growth. Other defects such as the crack visible in the bottom right of Figure 29, are most likely as a result of a thermal dislocation of the template PS opal. The synthesis temperature used to form the TiN material has led to the collapse of one of the bridging sections of the inverse opal. As the PS opal temperature changes, stress will be imparted onto the inverse opal as the template pyrolyses out and the TiN is forms and crystalizes. This strain will break the weakest point in the structure, which will be the site of one of these structural defects caused by the collapse of a 'bridge'. This will lead to further weakening of the structure in that area. In this way, a single defect, as is visible in Figure 27 (left image, centre), can become a crack, as is visible in the bottom right of Figure 29. These can cause the inverse opal to 'unzip', leading to linear fractures that can change course at 30 or 60 ° along the lattice planes in the inverse opal structure perpendicular to the inverse opal films surface.

3.6.1.2 X-ray diffraction

XRD data was collected on the smartlab instrument on samples prepared on gold coated silicon. This gave very sharp peaks, identifying that the intended nitride for each inverse opal (TiN and VN) had been formed (Figure 30). These diffractograms were of much higher quality than had been previously collected on nitride inverse opals within the group.

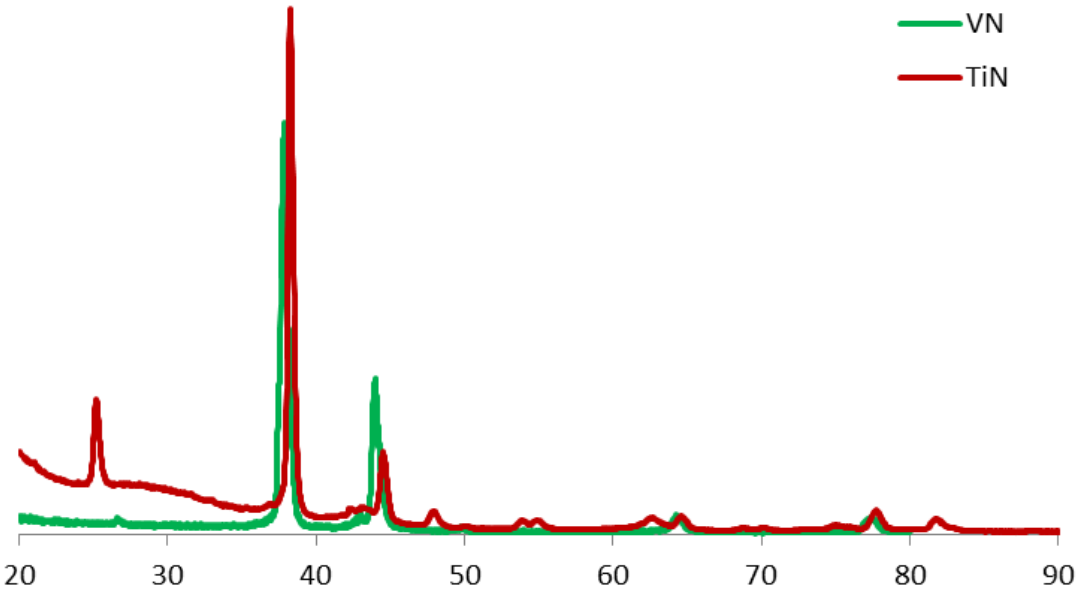

Figure 30: XRD of MN inverse opal films on Au coated Si substrates.

3.6.2 Electrochemistry of TiN inverse opals.

TiN inverse opals were initially cycled under the conditions outlined in 2.2.2. This resulted in the Au current collecting layer deposited onto the silica substrate delaminating from the substrate with the inverse opal. As a result of this, the potential range that the inverse opals were cycled over was reduced to 0.8 V (-0.8 V – 0 V vs Hg/HgO). This prevented the Au backing from delaminating and allowed for cyclic voltammagrams to be collected.

These cyclic voltammagrams were processed as described in 3.2.11 to give specific capacitances for the mass of material contained in the inverse opal structure.

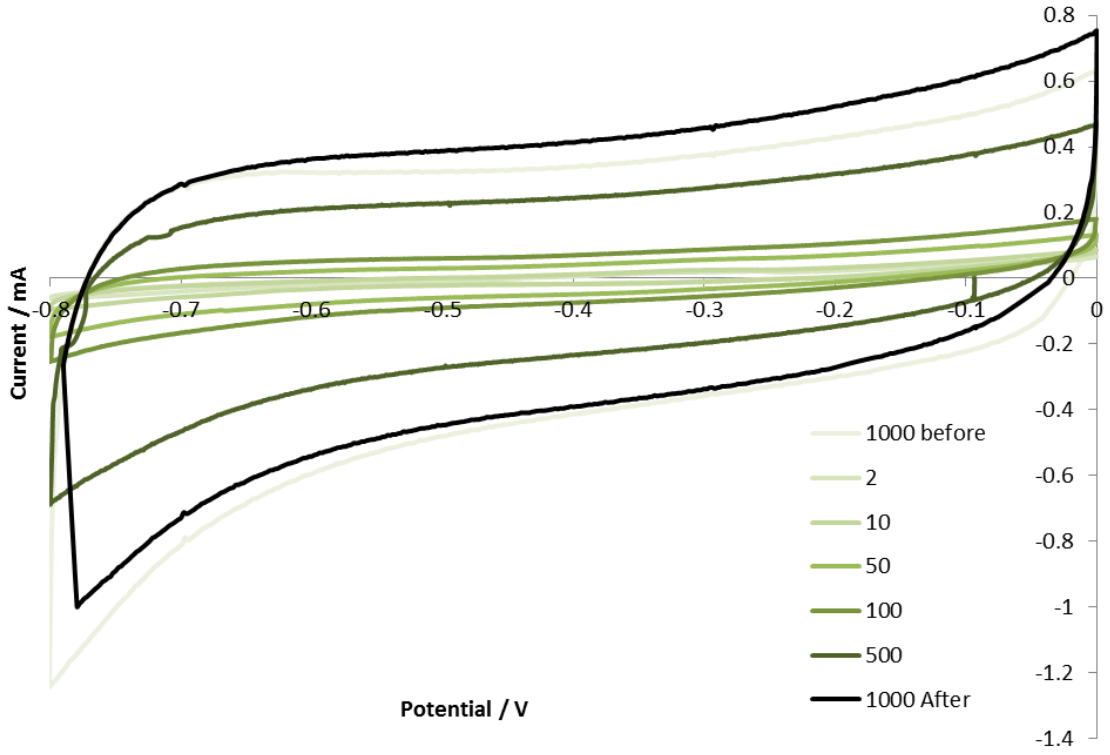

Figure 31: Cyclic voltammagrams collected on a TiN inverse opal film on an Au coated silica substrate in 1M KOH vs Hg/HgO reference at various scan rates (displayed in the key).

As this mass wasn't directly measured, an approximation calculated from the free volume in an FCC lattice, an estimated depth of the inverse opal film, the volume of the inverse opal film across the substrate and the density of TiN was used to give the specific capacity in F g^{-1}.

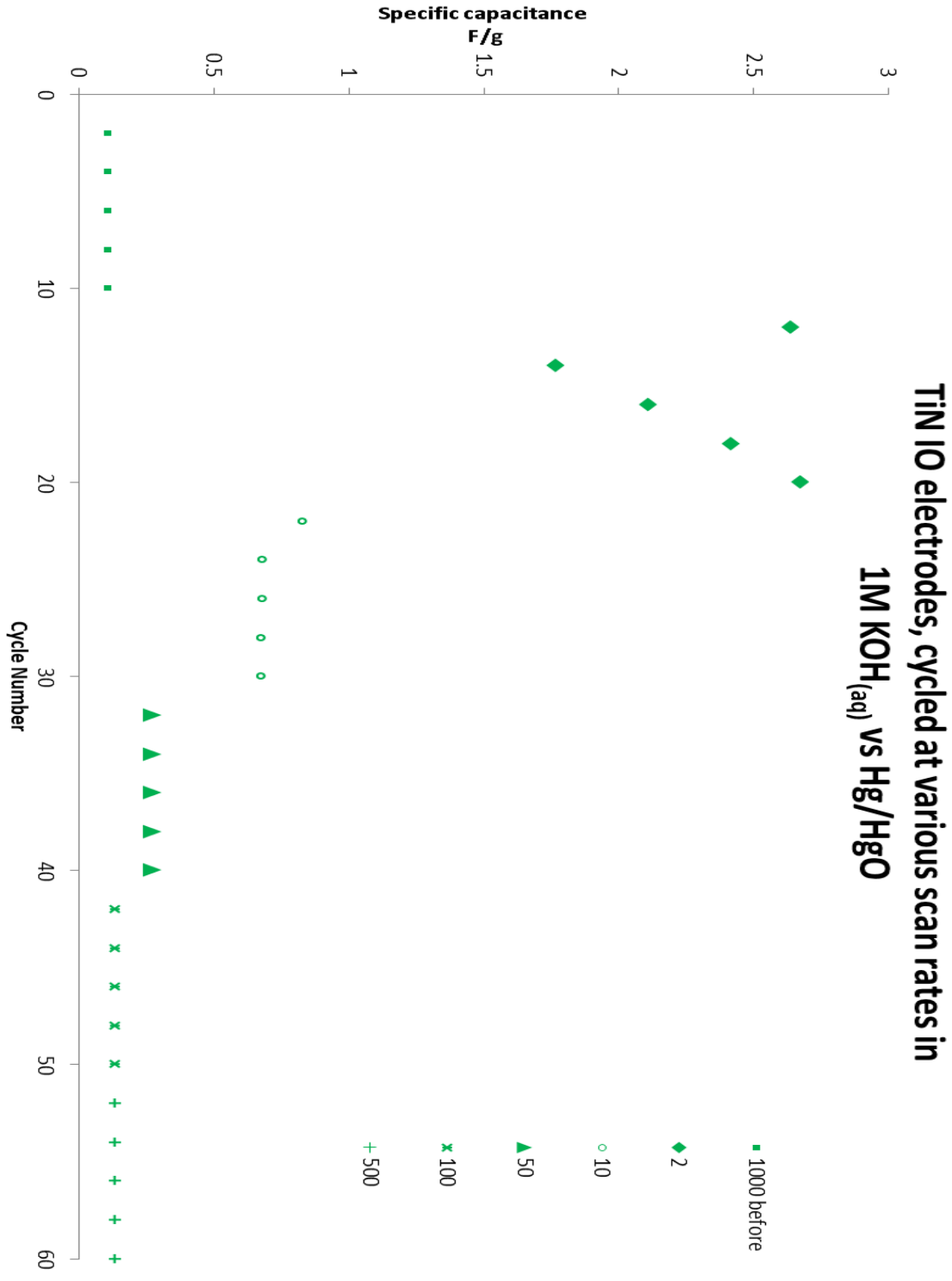

Figure 32: A graph of the specific capacity values observed for the TiN inverse opal films at various scan rates(displayed in the key).

Please note the units of the y axis compared to those of Figure 26 and Figure 64.

The capacitance of the inverse opal film is two orders of magnitude higher than the highest value observed for the 'flat' nitride foils (Chapter 5:) and five orders of magnitude higher than those observed for the solid solutions (3.5.2).

Over the reduced cycling range the highest capacitance observed was 2.67 F g^{-1} at 2 mV s^{-1}. This is one order of magnitude lower than the specific capacitances reported for some RuO_2 films used for super capacitor applications at similar scan rates.[88]

This specific capacitance is also stable over an extended cycling range, after 660 cycles the electrode exhibited a capacitance increase of 2.2 %. This supports the observation made with VN that a thin oxidised layer over the surface of a nitride under layer increases the specific capacitance of the material.

3.7 Conclusions and further work.

V^{IV} amides are much more sensitive than their Ti^{IV} analogues and a much higher degree of care and attention must be taken during their synthesis.

The ideal ratio of primary amine to metal amide for the formation of stable sols is two amide groups:one amine molecule, this has been found with $Ti(NR_2)_4$ and $V(NR_2)_4$ amides.

Of the solid solutions $Ti_{0.2}V_{0.8}N$ gave the highest specific capacitance of 58.5 F g^{-1} at a scan rate of 1 mV s^{-1}. This was different at higher scan rates where the $V_{0.4}Ti_{0.6}N$ solid solution gave the highest specific capacitance of 8.3 F g^{-1} at 500 mV s^{-1}. The solid solution that exhibited the highest stability is VN, showing a 17 % increase in specific capacity over the duration of the experiment of 60 cycles. The nitride powders used did not have their surface areas optimised for these experiments and this could have a considerable effect on their specific capacitance values.

The template synthesis and infiltration techniques, employed in the group previously, have been improved to enable the growth of templates across a much larger area showing a higher degree of ordering.

TiN inverse opals show a massively increased specific capacity over the TiN powders also tested in this chapter, exhibiting a peak specific capacity of 2.7 F g^{-1} compared to a capacity of 9 μF g^{-1} for the powdered TiN.

Further work should include synthesising a similar range of solid solutions from the dimethyl metal amides and evaluating their electrochemical performance. The increased reactivity of the dimethyl amides should speed this process up, providing enough $V(NMe_2)_4$ is readily available. Additionally, the synthesis of a VN inverse opal should be attempted using the dimethyl amide as well as synthesising the most promising V_xTi_yN solid solution into an inverse opal film and evaluating them electrochemically.

Following the evaluation of the solid solution inverse opals, thin films of the solid solutions should be grown and their surfaces modified (as detailed in Chapter 5: to attempt to optimise performance.

BET surface area analysis should be performed on the powders and inverse opals to allow for calculation of the specific capacitance in F cm^{-2} instead of F g^{-1}. This would allow the results for the specific capacity to be compared more easily with those for the surface treatments. The two studies should then be combined to try and find the ideal nitride composition and surface treatment combination.

An assessment of the feasibility of the synthesis of other solid solutions of rocksalt structured nitrides should be undertaken. These may display different electrochemical performance that far exceeds that observed from TiVN materials. Ni_3N materials have already been examined as the negative electrode for Na ion battery applications,[32] CrN and CrTiN have already been show to form an inverse opal morphology.[74] Both of these elements may have interesting or desirable redox properties for supercapacitors when combined with titanium or vanadium. Some of these compositions may be inaccessible via non-oxide sol gel routes so, in addition to this, the oxides of these solid solutions could be prepared and assessed for their ability to interconvert between the oxide and nitride. This has been demonstrated recently with CrN and CrTiN.[74]

Chapter 4: TaN_x sol-gel reactions and structured ammonolysis products.

Parts of this work were conducted with Christopher Mallinson as part of his third year research project, the template fabrication method was developed with substantial input and advice from Dr Martyn Mclachlan (Imperial College) and has also been published.[89]

4.1 Introduction.

4.1.1 Inverse opals.

Inverse opal structures offer a range of interesting properties not readily available in other morphological layouts. They can be used to filter specific wavelengths of light in the visible and infrared with the wavelengths affected determined by the size of their pores.[48] They have a low density, large free volume and periodic structure, making them ideal for uses such as catalyst supports, with liquid or gas feeds. Additionally they can be used as electrode materials where redox reactions are occurring with the electrolyte.[74] Restrictions in the speed of electrolyte diffusion to the electrode surface will restrict the rate at which a reaction with that surface can occur, leading to an apparent drop in the electrode's specific capacity. The honeycomb-like structure of the inverse opal allows for increased diffusion through the total volume of the structure, such that the bulk electrolyte concentration is more easily maintained throughout the structure, across all cycling actions, whilst still increasing the surface area of the electrode. This should lead to an increased specific capacitance for the material under study when compared to a nano- structured film with the same surface area.

Inverse opal films have been made employing a variety of methods. They have been deposited by 3D printing the structure, with the size resolution of the printer being the limiting factor on how small they can be. Inverse opals are normally templated around a sacrificial support template, which forms an opal structure. A considerable amount of the theory relating to the deposition of these opal templates has been developed by depositing regularly sized silica beads from aqueous solutions. The use of silica beads has its disadvantages:

If the volume occupied by the beads needs to be empty to allow the diffusion of reactants or electrolyte, then the removal of silica is accomplished using highly aggressive and dangerous HF acid washes. Whilst there are other materials that will dissolve silica, such as strong alkali washes, both present a less than ideal treatment for the nitride. If the desired application of the structure requires acidic or basic sites for reactivity, then a basic or acidic wash may present a problem for preserving these. Whilst the removal of these reactive sites might not affect the specific capacity of the material, they may be fundamental for the catalytic activity[90, 91] desired from other potential areas of application for these morphologies.

With this in mind, chemical methods for removing the template should be avoided. This limits the methods that can be employed to physical removal and thermal removal. Physical removal of the individual component beads on the 500 nm length scale that is desirable for this project is beyond the capabilities of the vast majority of technical institutes. This leaves thermal removal as the only remaining option.

Thermal removal of the template requires that the material from which the template is constructed behaves in a certain way when the temperature is changed. The template needs to melt out, evaporate or pyrolyse away from the desired inverse opal structure. This makes polymer beads appropriate choices for the template material.

Polymer beads can be synthesised from a variety of sources, usually using polystyrene or poly(methylmethacrylate) (PMMA) for the narrowest size dispersion. In this project, divinylbenzene cross linked, amidine capped, polystyrene spheres have been chosen as the templating material. This is because: standard polystyrene is not resistant to organic solvents[25]: Diethylamine and diethylether have been shown to make the beads swell and disrupt the opal structure of the template or dissolve the polystyrene beads themselves. Aromatic solvents (benzene, toluene) and THF very quickly dissolve the polystyrene template. The DVB cross-linking increases the resistance to swelling and dissolution. This means that the template does not become so disrupted and some templating can be observed when more polar solvents are employed.[25] The amidine caps on the polymer chains make the beads more compatible with the amide chemistry, allowing the bead surface

itself to react with the metal amide sol of the reaction solution (Figure 33), ensuring a strong chemical bond between the two. The final aspect of the beads that needs to be considered for template production is their size variance. This is specified as ±5 nm by the manufacturer (Invitrogen) for these beads. Too large a variance will increase the number of defects in the template produced and so the number of defects transferred to the inverse opal produced from that structure.

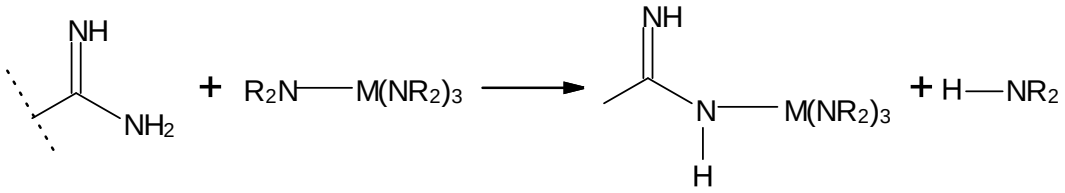

Figure 33: A one possible reaction between the amidine capped beads and a metal amide sol.

With regards to the thermal behaviour of the beads they do not melt below 300 ºC, but pyrolyse away at temperatures lower than 600 ºC[25]. At this temperature, the amide gel should have solidified around the beads and any remaining solvent should have evaporated out of the structure, meaning that the templated structure should be mechanically stable enough to survive removal of the template. This is the case with the TiN and SiN_x materials, in that this method has been previously employed,[25] the success of which was only limited by the template quality.

4.1.2 Photocatalysis.

Photocatalysis is the process by which energy is absorbed from sunlight and used to perform a task. These tasks in nature include photosynthesis, more engineered applications include the 'self-cleaning' abilities of windows[92] and hydrolysis reaction catalysts to generate hydrogen[93] for use as a cleaner alternative to hydrocarbon fuels.

The basic principle of photocatalysis is to promote an electron from its ground state in a material to an excited state in the energy level(s) above this ground state, in the presence of the components needed to bring about the desired reaction. In the case of hydrolysis this component is water. The energy absorbed by the catalytic material is released as the electron relaxes from its

excited state to its ground state. This energy can be transferred to these reaction components to promote the desired reaction, provided they are positioned close to the atom where this relaxation is occurring. A basic schematic of this can be seen in Figure 34.

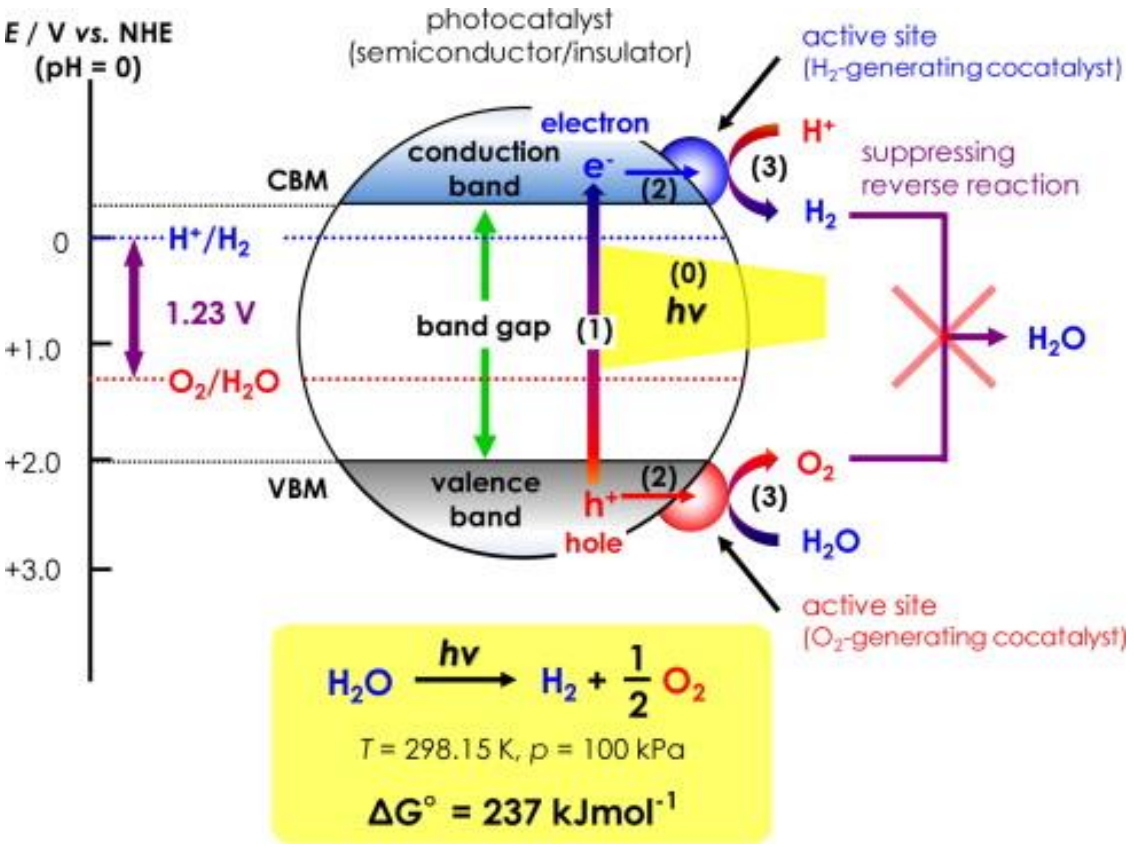

Figure 34: A diagram showing how a material could be employed for the photocatalytic hydrolysis of water.[94]

Image used with permission of the publisher.

The band gap of Ta_3N_5 has been calculated at around 2.1 eV,[95] corresponding to light of 590 nm (via $E = h c / \lambda$). Hydrolysis of water requires 1.53 eV[96] meaning that all the radiation absorbed by Ta_3N_5 can be used for hydrolysis. In order for the same semi-conducting material to perform both processes, the band gap of the material also needs to span across this 1.53 eV window, such that the edges of the band gap lie on either side of its energy.

4.1.3 Tantalum nitride.

Ta_3N_5 is a nitride of interest for photocatalytic hydrolysis applications.[93] Its red colour means that it absorbs a much higher % of the radiation spectrum that

makes it to the Earth's surface than TiO_2, a material that is currently used in many 'self-cleaning surfaces'.[97] If more photons are absorbed by these surfaces then the rate of any catalytic reaction taking place at these surfaces, whether self-cleaning or hydrogen evolution,[93] will be accelerated. There would, therefore, need to be less catalytic material to achieve the same turnover number required to produce enough hydrogen for widespread transportation use for example. Conversely, it makes more efficient use of the available sunlight falling on the earth's surface. This means that, when compared to TiO_2, less sunlight or Ta_3N_5 catalyst will be required to produce the desired quantity of hydrogen.

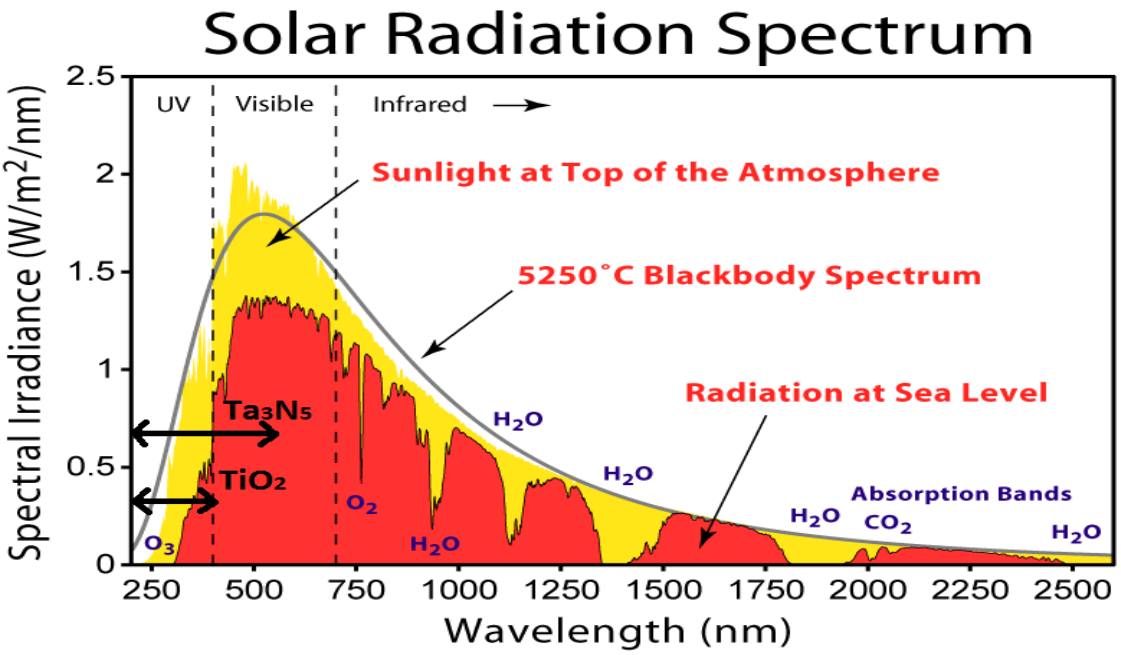

Figure 35: A graph showing the quantity and wavelengths of solar radiation to make it to the earth (inside the black line), available in the upper atmosphere (yellow area) and at sea level (red area).

A proportion of the energy from the sun that interacts with the earth does not arrive at sea level. It is absorbed by a variety of constituents in the atmosphere (O_3, O_2, CO_2 and H_2O are shown).

Image created by Robert A. Rohde / Global Warming Art.

At ground level (Figure 35), atmospheric O_3 has blocked a large amount of the UV wavelength energy that TiO_2 can absorb from reaching the surface of the

planet. As Ta_3N_5 absorbs into the visible spectrum, approximately eight times as many photons can be absorbed by it and provide electrons or holes.

This energy absorption range in addition to Ta_3N_5's band gap of 2.1 eV, corresponding to electromagnetic radiation of a 590 nm wavelength, makes Ta_3N_5 a material of great interest for creating a visible light wavelength hydrogen evolution catalyst. This has been described as a scientific 'holy grail'[98] as it would be a major milestone towards a potential hydrogen powered economy.

As Ta_3N_5 materials have shown such a promising potential towards the photolysis of water under visible light a wide range of morphologies have been explored already including; thin films,[99] modified nano powders[100] and nanotubes.[101] Inverse opal films would further expand the morphologies studied for this application.

4.2 Experimental.

4.2.1 General remarks.

$Ta(NMe_2)_5$ was supplied by Epichem/Aldrich. Owing to the air sensitive nature of the chemistry inert atmosphere handling techniques were employed. $Ta(NMe_2)_5$ is not as reactive as the 3d metal amides used elsewhere in this work (Chapter 3:), however, care was taken to avoid any atmospheric exposure to minimise oxygen contamination and the hydrolysis of the $Ta(NR_2)_x$ compounds. The DVB cross linked amidine capped PS beads were supplied by Invitrogen. n-Propylamine and deuterated solvents were supplied by Aldrich. C_6D_6 was stored over dried 4 Å sieves. Solvents were supplied by Fisher.

4.2.2 Amination of $Ta(NMe_2)_5$.[60]

In the glovebox, a Youngs tap Schlenk tube with a stirrer bar and septum was charged with $Ta(NMe_2)_5$ (4 g, 10 mmol) before being sealed and transferred to the Schlenk line. Under inert atmosphere, hexane (7.5 ml) was added with stirring and allowed to stir for 10 minutes to ensure the amide had fully dissolved, giving a straw yellow solution. n-Propylamine (2.05 ml, 25 mmol) was added carefully via syringe and the solution allowed to stir for 2 hours under Inert atmosphere. Over this time, a slight darkening of the reaction

solution was observed as the sol formed. This sol was then treated using one of the two ways detailed in section 3.2.9.

For some of the initial experimentation with $Ta(NMe_2)_5$ based sols, an equivalent volume of THF was used in place of hexane.

4.2.3 Infiltration of polystyrene templates.

Inverse opals of TaN_x were prepared by infiltrating an appropriate Ta amide sol into a prepared and dried PS template as described in section 2.1.2. To achieve a Ta_3N_5 inverse opal film, a substrate that will maintain its structure during ammonolysis must be used. Silica was found to give the best results.[60]

Inverse opal films were prepared by placing the PS template substrates, perpendicular to the direction of growth, into a sample vial and submerging the minimum amount of the substrate in a small amount of the Ta-amide sol to allow for capillary action to draw the sol into the void spaces of the template. These were then sealed to avoid splashing of the sol and left to infiltrate for 1 hour. During this time the volume of the sol visibly reduced to around 80% of the original volume as the sol was drawn into the template. The infiltrated template was then removed to a clean sample vial and allowed to dry for 2 hours.

4.2.4 NMR investigation into $Ta(NMe_2)_5$ amination.

In a Youngs tap flask with a stirrer bar, $Ta(NMe_2)_5$ (10.0 g, 25 mmol) was dissolved in $CDCl_3$ (25 ml) with stirring and allowed to stir for 30 minutes to ensure complete dissolution and intimate mixing. This flask was transferred to the glovebox, in addition to NMR tubes, dry pipettes and a syringe (1 ml). Portions of this amide solution (1 ml) were divided into NMR tubes before individually having various molar equivalents of n-propylamine (0.72 to 7.2 at 0.72 molar equivalent intervals, 0.059 - 0.59 cm^{-3}) added to them. Each tube was then quickly sealed and shaken vigorously to mix the amine and amide solution as effectively as possible. Once the tube had been shaken they were transferred from the glovebox to the NMR spectrometer and ^1H spectra run on the sample whilst the next amine concentration in the sequence was prepared. Once completed, the amide samples in the tube were carefully poured into a flask and the tubes were rinsed with ethanol. The samples and washings were

neutralised with more ethanol followed by water, to ensure the safe destruction of any amide species remaining. The waste was then disposed of safely. The spectra (Figure 39) were referenced to the residual proton signal of the NMR solvent.

Peak assignments are as follows: 'Propylamine' ($C_3H_8NH_2$) 0.55 ppm (s) Pr-N**H**$_2$, 0.77 ppm (t) C**H**$_3$-C_2H_4-NH_2, 1.23 ppm (m) Me-C**H**$_2$-CH_2-NH_2, 2.44 ppm (t) Et-C**H**$_2$-NH_2. 'PDMAT' ($Ta(NMe_2)_5$) 3.23 ppm (s) RTaN-C**H**$_3$. (0.72 to 7.2) 0.81 moving to 0.77 ppm (t) Pr-N**H**$_2$, increasing in intensity and moving from 0.92 to 0.89 ppm (m) possibly as a result of hydrogen bonding of the species in solution, (0.72 to 2.16 only) 1.16 moving to 1.14 (t) decreasing intensity, 2.21 ppm (d), 3.22 – 3.31 (m).

4.2.5 TaN_x film ammonolysis.

Flat films of TaN_x were prepared in the glovebox by dipping cleaned silica substrates into the Ta-amide sols, prepared above, to a depth of 20 mm before allowing the solvent to evaporate from the sol and being re-dipped. In total each substrate was dipped four times.

These films were placed into an alumina boat and loaded into a reactive gas furnace tube sealed with carbon-based grease before being transferred to the Schlenk line. The nitrogen used in the glovebox was purged from the furnace tube for 10 minutes with NH_3 passed through a column of 3 Å molecular sieves. Following this, the ammonia flow rate was lowered from the rate used for purging the apparatus to 1 bubble/second and the furnace tube was heated to a range of temperatures (600-800 ºC). This temperature was maintained for 10 hours before the furnace was allowed to cool to room temperature (5 ºC min^{-1}).

4.3 Development of template growth methodology.

The method previously employed in the group[25] to manufacture PS opal templates was a horizontal evaporative method, where a solution of the PS beads were evaporated onto a clean surface over a period of days in a refrigerator. This leads to the deposition of a film suitable for inverse opal production. However, the template film that is produced is polycrystalline and

exhibits only small areas of extended ordering (see Figure 36). Whilst this may be sufficient for proof of concept, there are clear areas for improvement: The amount of long range order needs to be increased to as far as possible; the number of defects needs to be lowered by turning this polycrystalline structure into a single crystalline structure; the deposition time needs to be reduced to increase the production rate of the template structures and the depth of template produced needs to be increased to increase the number of electrodes, as well as, the mass and surface area of electroactive material available for charge storage.

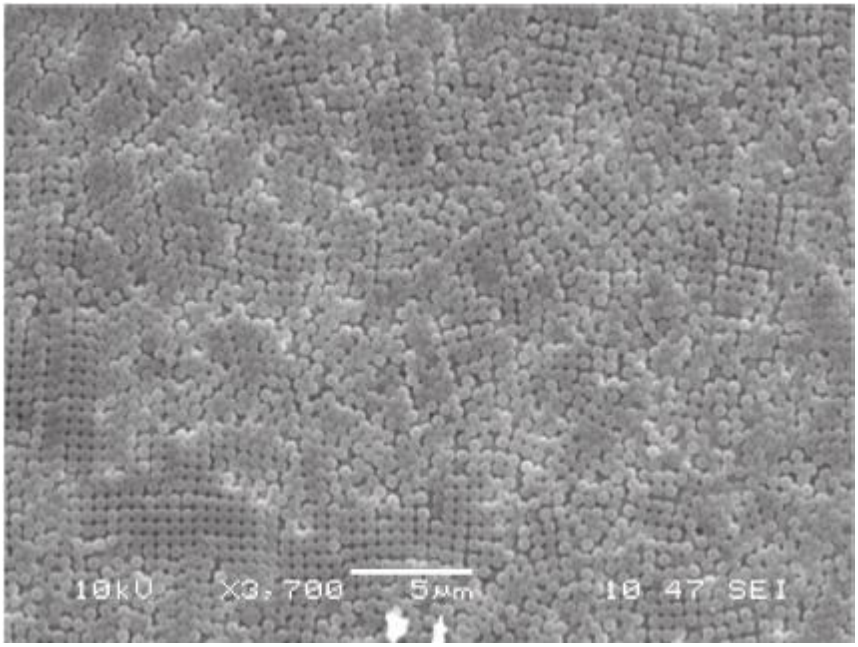

Figure 36: SEM micrograph of inverse opal templates previously synthesised in the group using a template of 500 nm PS beads.

The scale bar is 5 μm. These templates are iridescent to the naked eye, but are highly polycrystalline and exhibit low levels of long range order.

With these objectives in mind, an alternative method to the one currently employed was sought. Discussions with other researchers at UoS revealed that another research group produced similar templates for alternative uses and an attempt was made to use a revision of their method.[44, 58] This method involves suspending a substrate into a thermally stable suspension of PS beads and evaporating the solution with a flow of dry air. This method was unsuccessful, depositing only amorphous materials onto the substrates and so was abandoned.

The 'near vertical deposition' method was adapted to produce inverse opal films of the crosslinked PS beads as described in section 2.1.2. This method involves evaporating the colloidal solution of PS beads at an elevated temperature,[52, 53] in contrast to the reduced one used previously in the group. This elevated temperature accelerates the evaporation of the solution and leads to the deposition of crystalline opals displaying very long range order (Figure 37). This temperature must be stable, otherwise the template produced is banded, exhibiting banded regions of ordered deposition, amorphous deposition and no deposition across the substrate. The lack of ordering in the amorphous regions will lead to a lower surface area than for the crystalline regions, so the structured film produced from the template will have a lower overall surface area. This would lead to a lower specific capacitance per unit area or lower number of catalytic sites, depending on the material and application.

Controlling the hydrophobicity of the substrate surface seemed to be a key variable in whether the colloidal suspension deposited in an ordered template or not. Areas were observed, where tools had been used to handle and manipulate the substrates, showing foreign material had been transferred from the surface of the tool to the substrate resulting in no or amorphous deposition.

Another key variable was found to be the technique used to degrease the substrates. Methods were attempted using concentrated KOH washes followed by aqueous rinsing and drying. These had been shown to work when uncrosslinked PS beads were employed, but the attempts with the crosslinked amidine capped PS beads produced no ordered deposition. A further method was attempted using only organic washings to try and dissolve the surface residue without altering the glass substrate. This also resulted in no ordered deposition. The only degreasing method that produced favourable results was one utilising acidic piranha solution to remove the surface grease and protonate the glass surface. This surface modification will increase the attraction between the amidine caps on the PS beads and the substrate slightly, which presumably aids in the deposition of the beads onto the surface.

Templates produced in this way exhibit a far greater degree of long range order and large single crystalline strips across the width of the substrate.

Thermal fluctuations in the equipment used to deposit the templates could give rise to bands in the templates (Figure 37, upper image cracks running at approximately 45° to vertical). Another source for these cracks could be destabilisation of the structure as it dries. These could possibly be avoided if a truly stable temperature environment was used for the deposition or the beads were partially melted into each other and onto the substrate before drying.

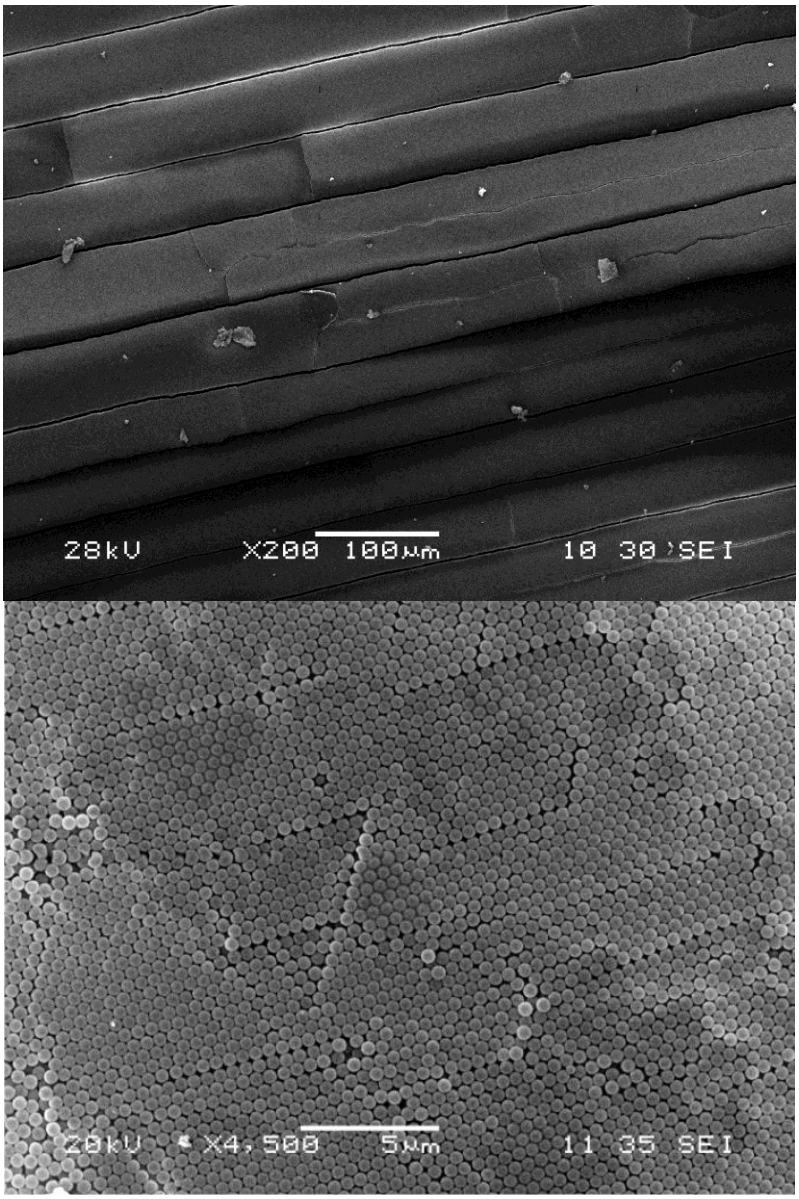

Figure 37: SEM micrographs of a PS opal template prepared by near vertical deposition.

Areas of the template exhibiting an even greater degree of long range ordering were observed but were impossible to image cleanly at a resolution where individual beads were observable due to the electron beam damage.

A depth assessment of the templates was not possible, owing to the near total coverage of the substrate with the crystalline template unlike the templates produced by horizontal deposition. Depth assessment could be achieved by cross sectioning the templates.

4.4 Investigation of the sol-gel behaviour of $Ta(NMe_2)_5$.

Ta is in group 5, however does not form Ta^{4+} amides in the same manner as V. It has a far greater preference to form a d^0 (Ta^{5+}) or pentavalent complexes. Additionally, $Ta(NEt_2)_5$ is unstable, forming a mixture of mainly $Ta(NEt_2)_4$ and $EtN{=}Ta(NEt_2)_3$ and a small quantity of $Ta(NEt_2)_5$ when sublimed from its crude reaction mixture (Figure 38). This elimination behaviour and resulting inability to synthesise and isolate an analogous Ta complex to the $Ti(NMe_2)_4$ used previously[25] means that the stable $Ta(NMe_2)_5$ amide must be used and the stoichiometry of the reaction needs to be adjusted accordingly.

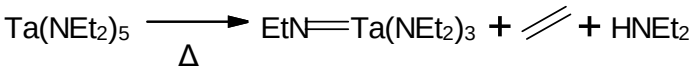

Figure 38: Scheme showing the formation of a tantalum imido complex on heating, as would happen during sublimation of the crude reaction material.

4.4.1 Sol behaviour of $Ta(NMe_2)_5$ sols.

The analogous tantalum compound to the V and Ti dimethyl amide compounds desired for making inverse opal MN films in Chapter 3: is $Ta(NMe_2)_5$. This amide material is commercially available or relatively easily synthesised, in a similar manner to the other metal amides examined in this project, by nucleophilic substitution of the metal chloride. The different number of NMe_2 groups around the Ta centre makes this an interesting compound to study with respect to developing the area of non-oxide routes to metal nitride inverse opals.

4.4.1.1 NMR study of the sol reaction of $Ta(NMe_2)_5$ and propylamine.

NMR studies of the reaction between propylamine and $Ta(NMe_2)_5$ were conducted in C_6D_6. This was conducted with controlled portions of H_2N-Pr being added to a fixed volume of a $Ta(NMe_2)_5$ in d6-benzene stock solution in the glovebox to give the desired propylamine;$Ta(NMe_2)_5$ ratios before the

samples were well sealed in NMR tubes, shaken to ensure full mixing and the spectra recorded, as rapidly as possible, to minimise amide hydrolysis.[60] The propylamine does not become visible on the NMR spectra until 2.88 equivalents are added suggesting that it is consumed into the structure of the polymer, where the lowered symmetry and restricted motion broaden its resonance signal, making it invisible on an NMR time scale. At this concentration there is a stable level of $HNMe_2$ dissolved into the NMR solvent, which appears to stay relatively constant. This is due to an equilibrium forming between the liquid sample and the gas above the sample in the NMR tube.

The NMR study (Figure 39) shows that at 2.88 equivalents of propylamine (Figure 39), the major constituent of the sol was small, oligomeric Ta-amide particles. A polymeric particle would show a single broad peak across this range, owing to the wide range of available quantum energy levels associated with the monomer units giving the signal. As an oligomer has fewer monomer units, the range of environments is reduced and so the range of energy levels available is lowered, meaning that the signals observed on the NMR spectra are more likely to be partly overlapping and less likely to be wholly overlapping, leading to sharper peaks. These are still merged together into a multiplet. This arises because of the chain entanglement of the oligomer units leading to the molecules relaxing from the energy imparted to them slowly on an NMR timescale. This leads to a very slow T_1 relaxation time, broadening the features observed on the NMR spectra.

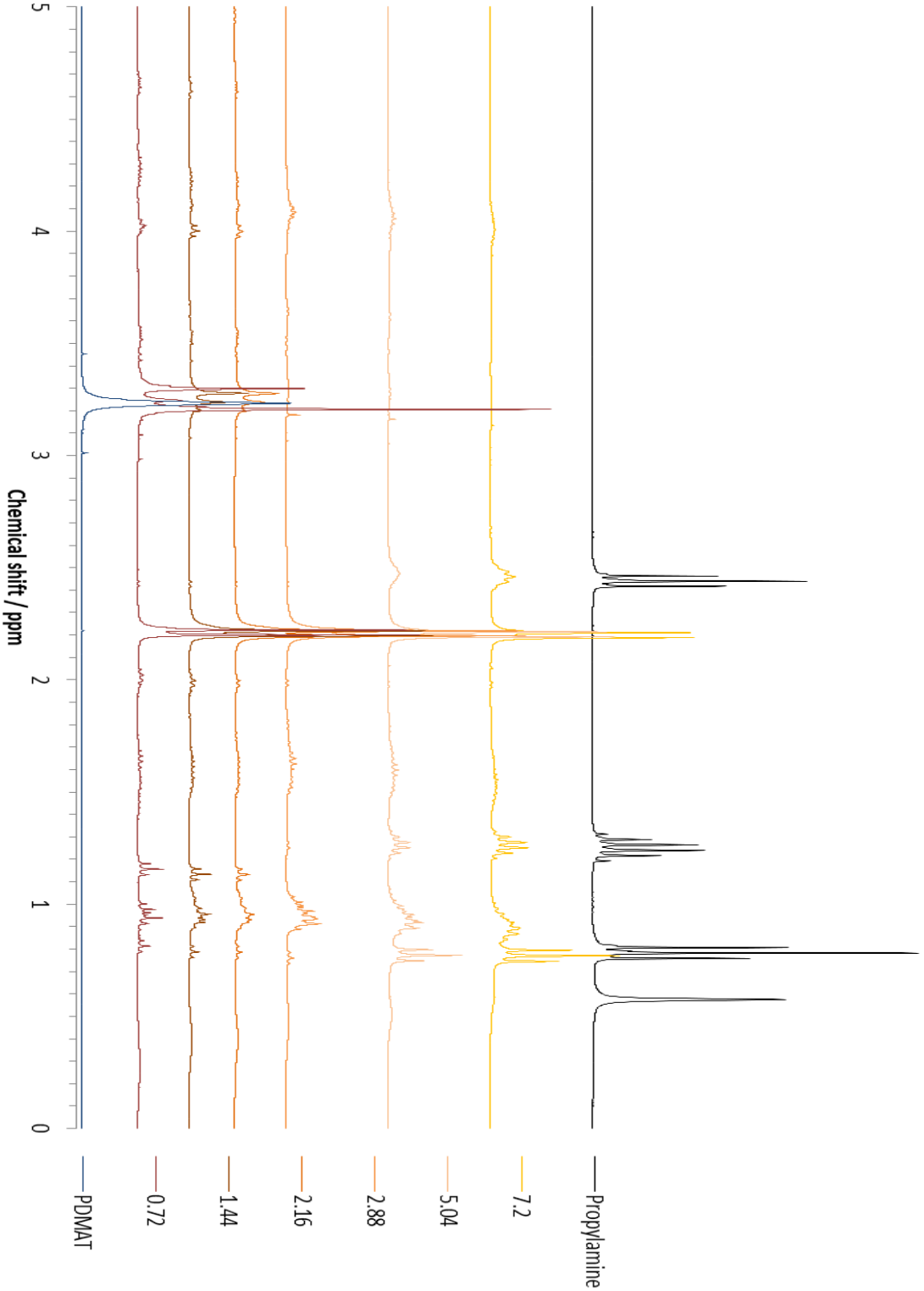

Figure 39: ^{1}H NMR spectra following the reaction of $Ta(NMe_2)_5$ and H_2NPr in various proportions conducted in C_6D_6.

Each series is labelled in terms of how many equivalents of n-propylamine were added to the reaction. Peak assignments can be found in 4.2.4

This study (Figure 39) suggests that the reaction does not consume any propylamine above 2.88 molar equivalents, supporting the logical prediction made above. The presence of free amine, as indicated by the signals from the $-NH_2$ (~2.45 ppm) above 2.88 equivalents, suggests that the amine is unable to react with the metal amide above this concentration, possibly due to steric effects from the previously reacted N-Pr groups around the Ta centres. This all suggests that in contrast to the Ti system studied previously,[45] reaction of primary amines with the Ta centre is slow, possibly due to the increased steric bulk around the Ta centre in $Ta(NMe_2)_5$.

The ideal adjustments to the stoichiometry of hexane and propylamine used compared to those used for the Ti-amide sol[25] are detailed in section 4.2.2 above. The ideal molar ratio of amide groups co-ordinated to the metal centre to primary amine appears to be 1:2, as evidenced by the molar quantity of amine employed with both four co-ordinate and five co-ordinate amides being 2 and 2.5 respectively. Whilst it is incorrect to assume a pattern from two points, this conclusion makes logical sense as each amine has two N-H bonds, which can substitute a single M-N bond each, bridging two adjacent metal centres. The amount of amine that gave the highest quality thin and inverse opal films (discussed in section 0) was a 3:1 H_2NPr: $Ta(NMe_2)_5$ sol. This slight excess ($1/5^{th}$ above the expected value) should have ensured that all the Ta atoms in the polymer were linked to as many neighbouring Ta atoms in the sol as possible, ensuring that the polymeric particles in the sol were as saturated with nitrogen prior to ammonolysis as possible.

4.4.1.2 TGA of the Ta-amide gels.

Samples of the Ta-amide gels prepared with a 3:1 ratio of propylamine:PDMAT, dried and analysed by TGA under N_2 and oxygen.

TGA under N_2 of a Ta sol (Figure 40) showed that, as had been observed with Ti based sols,[46] the major mass loss in the heating process occurs around 125-150 °C. This mass loss could be from the evaporation of any remaining solvent trapped into the gelated solid of the sample. A further mass loss occurs at 250 °C and continues steadily to 350 °C. It has been suggested that this mass loss also corresponds to the removal of the carbon containing side chains[46] from the metal amide polymer. This is a logical assessment as the

polymer beads are polystyrene and decompose at a similar temperature under nitrogen atmosphere.

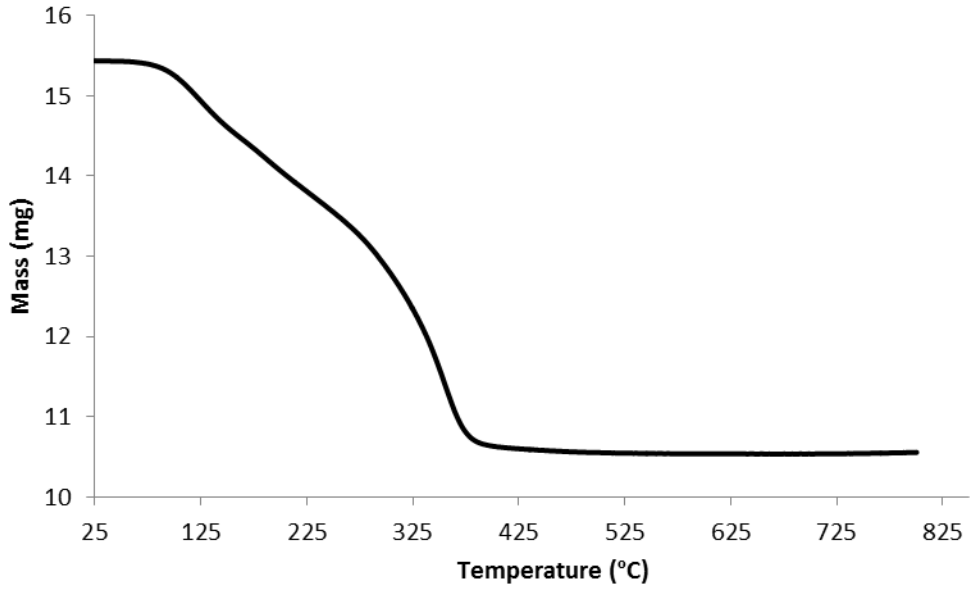

Figure 40: TGA of a 3:1 propylamine:PDMAT gel under N_2 at 50 ml min^{-1} and 10 °C min^{-1} heating rate.

TGA performed under oxygen of the Ta-amide gels (Figure 41) shows a very rapid mass loss from 55-180 °C. This suggests that the initial mass loss observed from both samples is the loss of residual solvent from the gels. However, the rapid mass change in the TGA under O_2 also indicates the removal of some co-ordinated groups by the O_2. Further mass loss is observed from 200-500 °C, most likely from the removal of the organic side chains in the polymeric structure, present either from the propylamine or the dimethylamino groups of the starting materials. A further mass loss is observed from 500-800 °C. This is likely the combustion of elemental carbon contained in the structure from the decomposition of the solvent or organic parts of the polymer, and accelerates from 625 °C to the highest temperature of the TGA sample (800 °C).

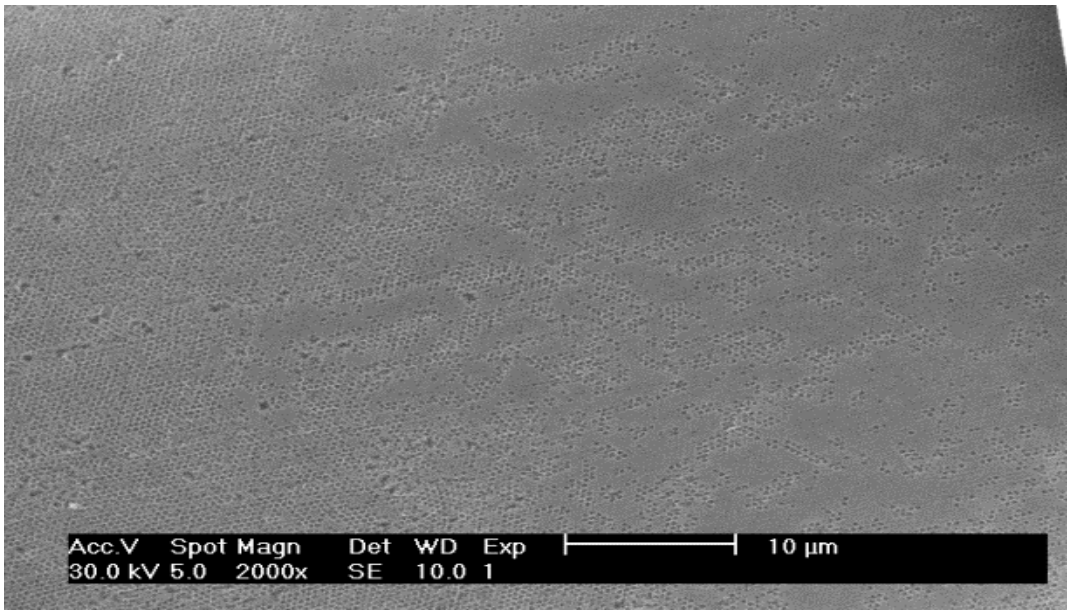

Figure 41: An SEM of a Ta_3N_5 inverse opal film on silica ammonolysed at 700 °C, showing the long range of ordering present in the films. At 2000 x the 500 nm templated pores are barely visible.

TaN_x compounds present an outstanding opportunity to more quickly study and understand how the sol chemistry of Ta-amides affects the tantalum nitrides produced from those sols. Solid thin films present a better option than templated ones to study the coating and ammonolysis conditions that will produce the highest quality films. In addition to this TaN_x films are of interest for barrier materials in electronics.[102]

It is not possible to create thin films or infiltrated structures with the materials derived from a $Ta(NMe_2)_5$ and ammonia reaction, as these reactions lead to the aggregation and precipitation of the Ta-amide material.[103] Investigation of the production of TaN_x films and inverse opals was undertaken with this is in mind, to attempt to find a sol-gel method that could produce thin and or templated TaN_x films.

A range of problems were encountered with the substrates used and the temperatures employed for the conversion of Ta-amide infiltrated templates to TaN_x materials. The templates used initially were made using standard glass microscope slides as substrates. This material, unfortunately, softens and melts around 600 °C. The temperature required for the conversion of the sol into TaN_x materials is around 700 °C, making glass an unsuitable choice for substrates.

At 800 °C, the amount of thermal strain generated in the structure caused a large number of cracks and distortions of the structure produced, as can be seen in **Error! Reference source not found.** However, at 800 °C the material of which the structure comprised of was the desired Ta_3N_5 material targeted for photolysis applications, as shown by XRD (Figure 43).

At 600 °C the amount of observable cracking and distortion was greatly reduced. However, the conversion of material to Ta_3N_5 was incomplete and the material, either, failed to crystallise or was not present as it was not observable by XRD (Figure 43). This is supported by literature reports of the formation of crystalline Ta_3N_5 occurring at temperatures above 800 °C.[104] The material that was observed at 600 °C was a phase of TaN. This implies that whilst this temperature is hot enough to facilitate the removal of all the hydrocarbon species in the structure (the –R groups and the PS template), it is lacking in sufficient energy for the full conversion of the Ta(amide) sol to Ta_3N_5. A temperature of 600 °C was attempted as it is the highest temperature that the glass substrates used had been shown to tolerate without distorting due to becoming less viscous and losing their structural rigidity.

4.4.2 Synthesis of TaN_x thin films.

The ratio of amide to amine that worked best with Ta was higher than that employed with the V and Ti at three equivalents of amine to one equivalent of amide, compared to the 2.1:1 observed for $M(NR_2)_4$ compounds and the 2.5:1 expected for the Ta-amide. 2.5:1 was expected based upon the $M(NR_2)_4$ compounds requiring one N-H bond to substitute one of the M-NR_2 groups from its structure and having four M-NR_2 groups to substitute.

Sols synthesised with a 1:3 relationship of $Ta(NMe_2)_5$:propylamine produced a sol that was suitably concentrated to deposit enough Ta_3N_5 into the void spaces of the templates and to generate a dense structure on ammonolysis, and not too viscous to infiltrate into the template. This ratio is in excess of the ratio indicated in the NMR study as the point at which unreacted H_2NPr is observable, suggesting that there should be an excess of primary amine for the amide to react with and form a gel. The increased viscosity of this sol will help with the infiltration process as the increased surface tension will help

draw the sol into the template or help more of the sol to stick to the surface of the substrate to generate a thicker or denser film.

This ratio is slightly higher than the amide:amine ratio used for tetravalent amides. This is not unexpected as $Ta(NMe_2)_5$ is pentavalent, so would require five N-H bonds, or three molecules of propylamine, to fully substitute the dimethyl groups.

Using the information from the TGA of the Ta-amide gels and knowledge about the combustion of the templates,[25] it was decided that the films should be heated between 600 and 800 °C. At 600 °C, the inverse opal structure is still observable using other metal amide systems[25] but the Ta_3N_5 material desired probably has not fully formed. At 800 °C the TGA suggests that the material from the templates should have combusted from the structure as well as the Ta_3N_5 material should have formed. However, prior experience demonstrated that at temperatures significantly above 600 °C the inverse opal structure desired collapsed,[25] although this could have been due to a change in crystal structure, in addition to the temperature.

4.4.3 Thin films.

Thin films of TaN_x were prepared using THF sols with a 3:1 amine:amide ratio in hexane. At ammonolysis temperatures of 600 °C, this produced films that were black in colour and poorly adhered to the substrate, with the majority of the material being recovered from the bottom of the alumina boat after the reaction. This dark colouration is usually indicative of high carbon content in the films produced from other metal amides. However, this is not shown in the XRD analysis of the films produced at this temperature. XRD of material prepared at this temperature, collected from the alumina boat, suggest that the deposited material is not crystalline (Figure 43, bottom spectra).

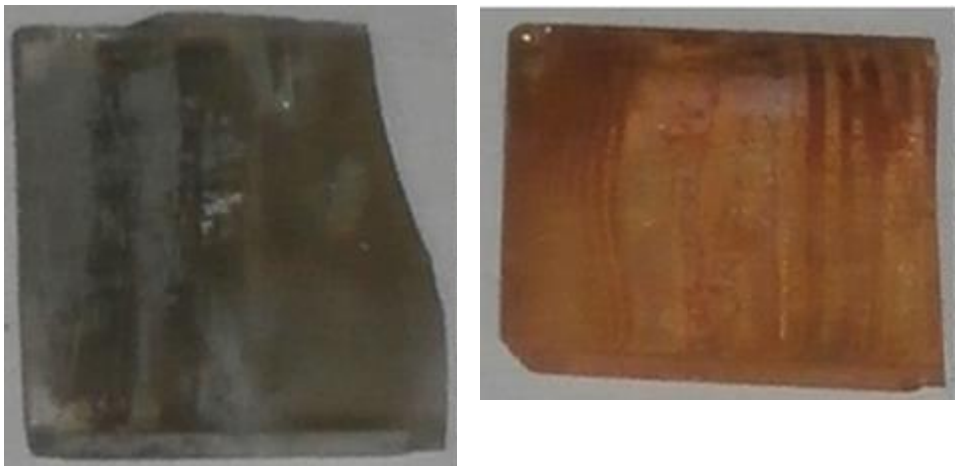

Figure 42: Photographs of the $Ta(NMe_2)_5$/propylamine in THF thin films at 600 °C (left) and 700 °C (right).

The darker film probably contains more carbon left over from the starting materials, at higher ammonolysis temperatures these carbon containing species are removed more effectively.

A further attempt using a THF sol produced a film with much better surface adhesion of the deposited black/brown material at 600 °C (Figure 42, left). The films heated to 700 and 800 °C were orange-red in colour (Figure 42, right), visually indicative of Ta_3N_5. This was confirmed by XRD (Figure 43, middle and top pattern). The Scherer equation was used to calculate the crystallite size of the 800 °C sample from the peak width, indicating that the crystallites were 267 Å.

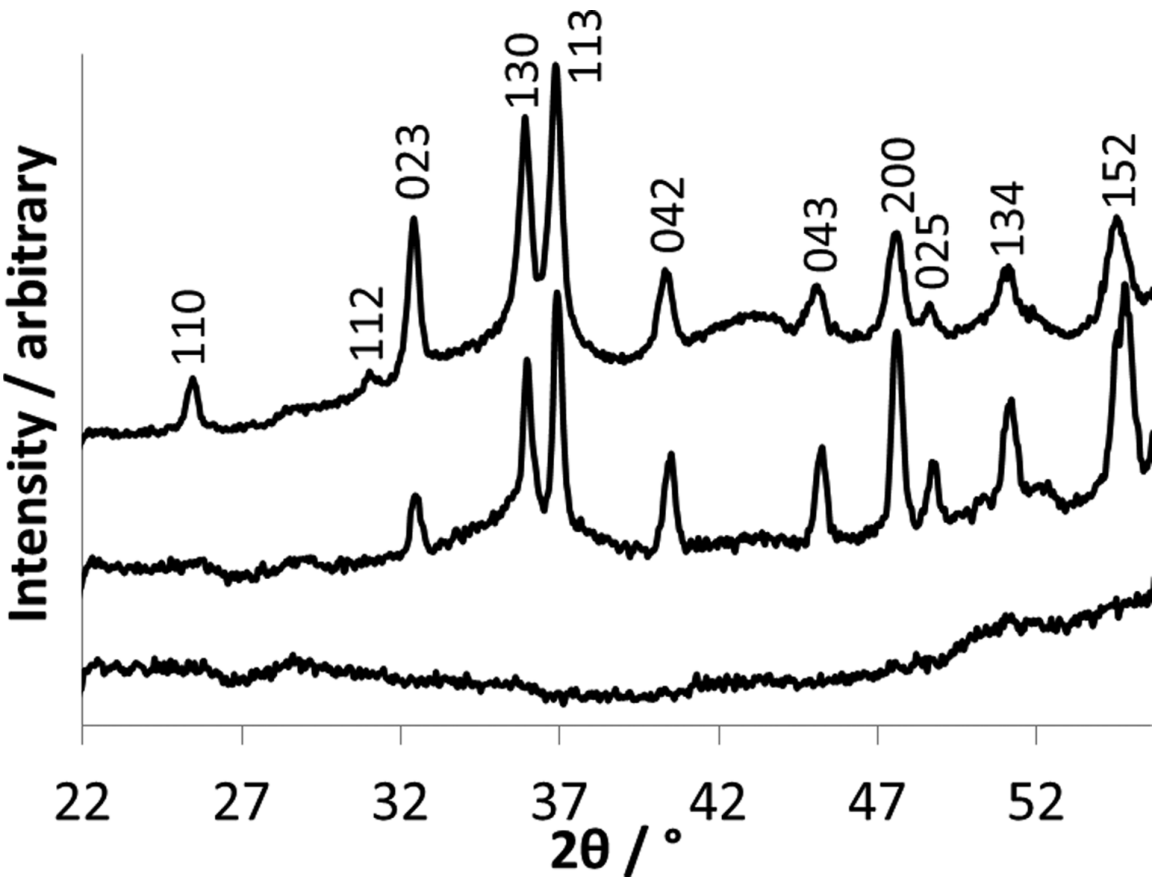

Figure 43: XRD (Bruker C2) of the TaN_x films prepared from $Ta(NMe_2)_5$/propylamine sols in THF.

The bottom spectrum is of a 600 °C film, middle is 700 °C and the top of an 800 °C film. The 600 °C spectrum shows that no crystalline material is present on the surface of the substrates. The 700 °C and 800 °C spectra both show that at these temperatures, Ta_3N_5 is formed using the ammonolysis conditions employed. The Miller indices displayed above the spectra correspond to those of the orthorhombic form of Ta_3N_5.[60]

4.4.4 Inverse opal films.

Owing to the group interest in inverse opal films and nitrides, there was a desire to improve upon the development of inverse opal nitride films. TaN_x species were chosen owing to the ease of procuring the amide precursor and the interest in Ta_3N_5 as a potential reaction catalyst for hydrogen evolution.[101] A structure that allows for the easy diffusion of reactants and products to and from the active sites, such as an inverse opal, would be advantageous for this application.

TaN_x inverse opal films were prepared by infiltrating an opalescent template, prepared as detailed in section 2.1.2.2, with the 3:1 amine:amide $Ta(NMe_2)_5$ in hexane sol. The infiltrated PS opals were fired at 600, 700 and 800 °C. These showed that at ammonolysis temperatures of 800 °C, the structure collapses and a dense film of Ta_3N_5 is formed where the PS opal s were exposed. In areas where slight over infiltration of the Ta amide sol had occurred and covered the surface of the template, some structuring was observed on the SEM (Figure 44).

In areas where the film had been 'over infiltrated', a thin layer of material was present over this ordered structure. Through cracks in this surface layer (Figure 44), presumably from the thermal cycling of the films, some templated structuring is visible via SEM.

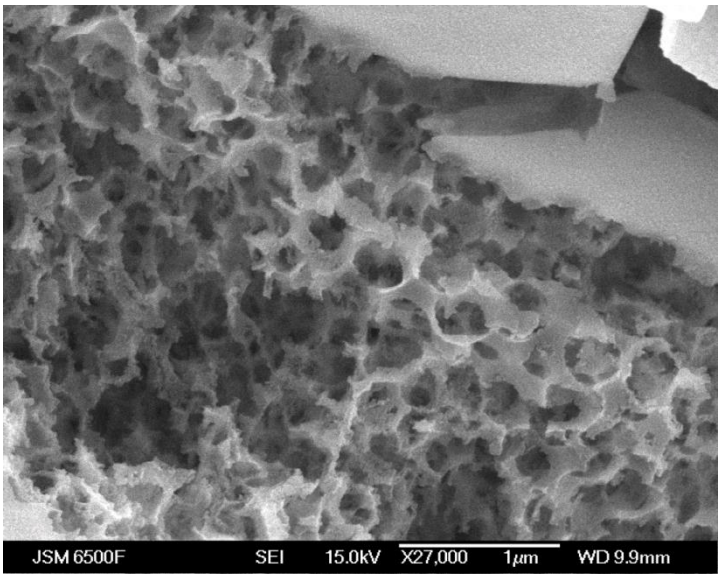

Figure 44: An SEM micrograph of a partially collapsed Ta_3N_5 macroporous film synthesised at 800 °C.

The image is at roughly X 27000 magnification and a cracked 'protective' over-infiltrated layer can be seen in the upper right of the image.

At the lower ammonolysis temperatures inverse opal films exhibiting long range order were formed (Figure 41 and Figure 45, lower two images). In some regions of the film, the inverse opal films exhibited regions where the template deposition had deposited structures of beads exhibiting little to no long range order (Figure 45, top). This demonstrates that the sol infiltration will work with a variety of structures where there is sufficient surface tension between the individual particles for the sol to be drawn into the structure by

capillary forces, irrespective of the degree of ordering observed in those structures.

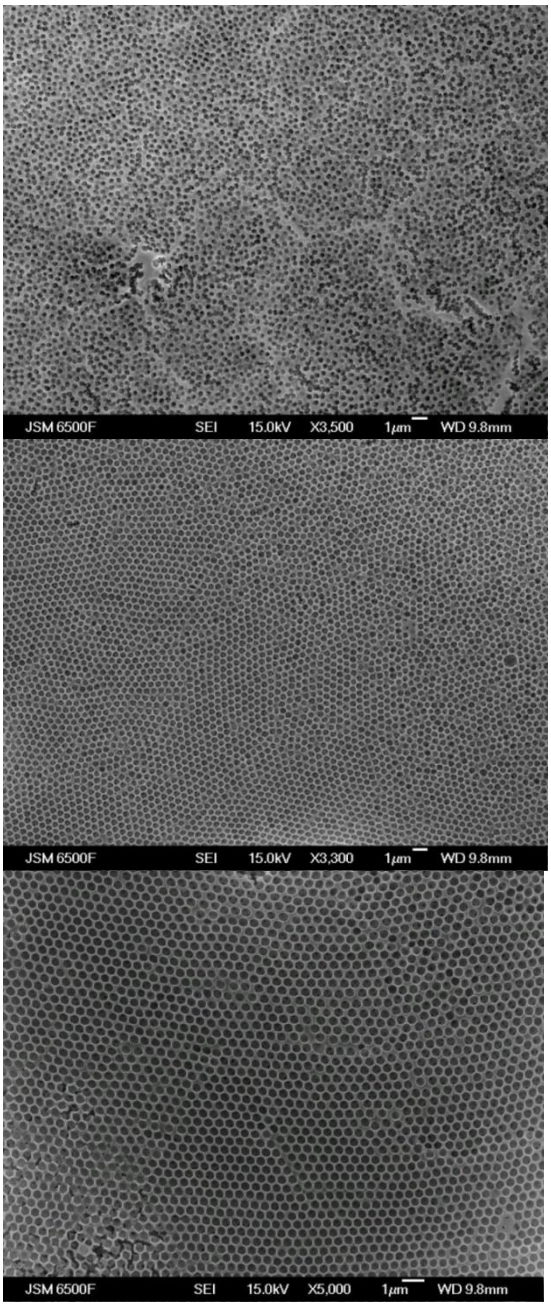

Figure 45: SEM micrographs of templated inverse opal TaN_x films synthesised at 700 °C.

The upper two images are at 3500 x and the lowest at 5000 x. In all cases the scale bar is 1 μm. The top image shows an area of the tile where amorphous deposition of the template particles had occurred, been infiltrated and its inverse structure preserved in the film. The lower two show the nearby region of the film, where a crystalline template had been deposited and infiltrated. The cracking in the lower left of the bottom image is most likely from thermal expansion and contraction stress.

The films ammonolysed at 700 °C gave the best combination of desired material and preservation of templated structure. This lower synthesis temperature results in a larger crystallite size (146 Å at 800 °C vs 247 Å at 700 °C) size as indicated by the XRD. This could have an effect on the surface area of the film at the nanoscopic level but not to the same extent that the collapse of the inverse opal structure.

4.5 Conclusions and further work.

$Ta(NMe_2)_5$ reacts with propylamine in a 1:3 ratio to give a suitably viscous sol for infiltration and dip coating films of Ta_3N_5.

It is possible to template Ta-amide sol compounds around the polymer bead templates used previously in the group. These infiltrated structures can then be pyrolysed under an ammonia atmosphere at 700 °C to produce Ta_3N_5 inverse opals.

The route used previously in the group with tetravalent inorganic amides (Si and Ti) to synthesise inverse opal films by templating around amidine capped PS spheres has been extended to a pentavalent metal amide with minor modifications. This suggests that the methodology employed is more widely applicable to creating other metal amide sols from a more diverse range of co-ordination environments, and potentially their nitride counterparts.

The quality of inverse opal templates within the group has been improved; templates exhibiting a much higher degree of long range order are now able to be prepared in a much shorter period of time (3 vs 7-10 days).

The TaN_x materials prepared in an inverse opal morphology film should be tested as hydrogen evolution catalysts. This would allow another structure type to be explored for this application.

The possibility of combining pentavalent and tetravalent metal amides into solid solutions should be explored. This may give rise to interesting synergistic effects between the metal centres in the final nitride products, which may have applications in improved photocatalytic performance of Ta_3N_5 or other areas of catalysis. If the inverse opal morphology is shown to be

advantageous to catalysis reactions then these solid solutions could also be deposited in this structure type and tested.

An interesting proposition might be the pursuit of a Ta alkoxide based sol to synthesise inverse opals before converting them to Ta_3N_5 materials via ammonolysis. This has been demonstrated with CrN and CrTiN inverse opals's[74] and could be extended into working with other group V and IV elements (S, Se, Te, P, As) if desired, to synthesise sulphides, selenides, tellurides, phosphides and arsenides.

Chapter 5: The effect of surface treatment on charge storage properties of TiN and VN.

Owing to circumstances beyond my control, I was unable to perform the final section of the experimental work for this chapter. Some of this data was collected, under my direction, by Andrew Hector. Parts of the data for the cycling of the VN electrodes are incomplete due to problems that were only identified during writing.

5.1 Introduction.

In order to optimise any potential metal nitride supercapacitor for electrochemical performance, one factor that cannot be ignored is the surface chemistry of the metal nitride. This chapter examines this factor for TiN and VN.

Nitrides have been specifically chosen for this work as they exhibit a high level of chemical stability, imparted by the strong ionic bond between the metal cation and the N^{3-} anion. Whilst this is desirable for supporting structures, it does not provide an electrochemically active redox surface for charge storage applications in the materials under study. With this in mind, it was thought that oxidising the top layers of atoms in the nitride material surface would provide a more redox active layer for charge storage without compromising the conductivity of the nitride bulk. This would mean that electrons could be effectively transported to or from this more reactive surface. This is supported in the literature by studies that have 'passivated' nitride materials to give high specific capacitances.[42]

In previous reports, TiN has been cycled in aggressive basic electrolytes,[105] exhibiting a stability window of around 1.4 V in 6 mol dm^{-3} KOH. This suggests that although stable to basic solutions with no applied over- or under-potential, it is possible to produce a fully or partly oxidised surface on TiN in a basic solution with sufficient over-potential. TiO_2 species are known to be useful in charge storage applications, both for aqueous[39] and lithium

insertion[106] conditions, so the controlled growth of TiO_2 surfaces merits investigation.

In addition, VN has been studied by cyclovolatmmetry in 1M $KOH_{(aq)}$ electrolyte as a slurry/ink combined with poly-(vinylidene fluoride) (PVDF) and N-methylpyrolidinone (NMP) before being applied to Ni electrodes.[42] This produced a remarkably high specific capacitance of 1340 F g^{-1} at 2 mV s^{-1}.

$V_2O_5.H_2O$ has been studied,[107, 108] but owing to its low conductivity, it is unsuitable for the fast charging and discharging rates required for capacitors. This is true even when combined with a high proportion of carbon (25%) to improve this conductivity, it exhibited 350 μF g^{-1} at a relatively slow scan speed of 5 mV s^{-1}.

As films of metal nitrides are time consuming and technically involved to produce via a non-oxide sol-gel route, an alternative route to produce metal nitride films was sought. The literature suggested that bulk samples of early transition metals could be nitrided by heating under ammonia.[23] This was chosen as the best method to produce the required metal nitride surfaces for this type of testing as they could be produced comparatively quickly and in larger volume than by a sol-gel route. The method employed in the literature was altered slightly so as to produce as little of the undesirable M_2N species as possible. For Ti and V this alteration consisted of lowering the ammonolysis temperature by 100 K and ensuring that there was a good and unrestricted diffusion pathway to the metal surface. The major problem with ammonolysis of this type for this project is the high temperatures required for the conversion from elemental metal to nitride (1000 °C in this work for Ti, see section 5.2.1) when compared to an equivalent sol-gel process (600 °C). This problem is also referred to as 'The Chromium Enigma'. TiN, VN and Cr all exhibit good thermal stability, with synthesis temperatures much higher than for the other 3d metals,[25, 42, 109] typically between 600 and 500 °C for high degrees of crystallisation. Later 3d transition metals tend to produce more metal rich compositions and synthesis temperatures of around of around 250 °C.[110]

Problems were noted with the samples used in that they were very brittle and not robust to handling. For delicate morphologies this is less than ideal as a great deal of care and time is required when handling the samples used here.

In addition to the Ti and V detailed here, it is possible to nitride Cr at temperatures around 900 °C under NH_3 atmospheres.[23] MnN_x[111] and Ni_3N[110] nanoparticles can be grown on or from their base metals at lower temperatures, 700 and 240 °C respectively. The trend in decreasing temperature appears to move along the period as the atomic mass of the metal part of the nitride increases.

Surface oxide has been identified as the redox active component in other studies using metal nitrides as supercapacitors.[15, 42, 112-114] Controlling the oxide formation over a highly conductive metal nitride support could allow optimisation of the capacitance.

5.2 Experimental.

5.2.1 Preparation of metal nitride foil electrodes.

Metal foil nitridation

The procedure used is adapted from the literature;[23] a lower dwell temperature was used to avoid the formation of Ti_2N species (discussed further in 5.3 below).

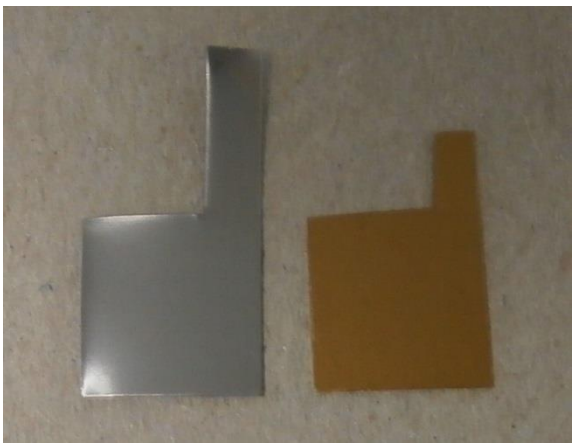

Figure 46: A photograph of Ti based electrodes before ammonolysis (left) and after ammonolysis at 1000 °C (right).

Areas found to be richer in Ti_2N species displayed a more red-bronze colouration.

Titanium metal (Aldrich, 0.25mm, 99.96%) was cut into 10 x 25 mm strips with a guillotine, before being cut into flag shapes with 10 x 10 mm 'flags' and 10

x 3 mm 'poles' (Figure 46) providing there is enough material for a crocodile clip to attach on to on the 'pole' and obtain a good electrical contact the size of this pole is not critical. The shaped metal electrodes were then degreased by sequential ultrasonic treatment in each of the following solvents: acetone, IPA, EtOH and water, with each electrode being rinsed with a clean portion of the solvent it had left and the one it was about to enter (e.g. EtOH sonication, EtOH rinse, H_2O rinse, H_2O sonication). Once all four sonication/rinsing cycles had been completed the electrodes were left to dry on clean tissue paper.

The electrodes were placed in sets of four into a clean, dry alumina boat before the boat was placed inside a 1 m, B24 quartz tube. The quartz tube was carefully suspended through a tube furnace and clamped so that the alumina boat ended up in the middle of the furnace. The quartz tube was attached to an Ar gas supply and purged of air through an oil bubbler (10 minutes). Following this, the Ar was replaced with an ammonia gas supply via a tube of dry 3 Å molecular sieves and the Ar purged from the tube with NH_3 (10 minutes). 3 Å sieves were selected because of their ability to absorb H_2O in preference to NH_3.[115] The flow rate of ammonia was lowered from the rate used for purging and set to approximately one bubble per second through the oil in the bubbler. The furnace was heated to 550 °C before dwelling for 20 minutes so the temperature could stabilise, then heated to 1000 °C at 1 °C/min with a 10 hour dwell, followed by cooling to room temperature (Figure 47). The heating profile is based upon a literature procedure[23] with the dwell temperature lowered to produce less undesirable Ti_2N by-product.

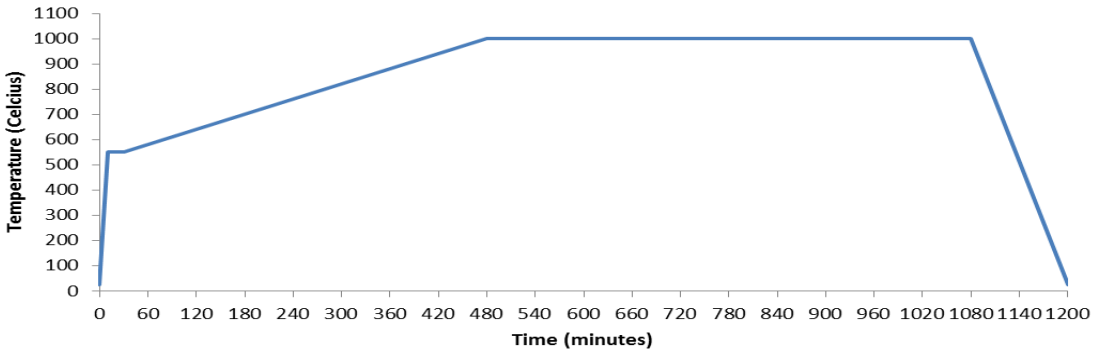

Figure 47: A graphical representation of the heating profile used for the ammonolysis of the metal foil electrodes.

The electrodes were gold coloured (Figure 46, right hand image). Grazing incidence (1° - 5°) XRD analysis suggested that these were the most TiN rich electrodes (for the 1 μm depth closest to the surface) of the temperatures examined and that any produced that were more red-bronze were richer in Ti_2N phases[65] at the surface. Regions of this bronze colour occurred where the access to the Ti surface was restricted, either by the electrodes overlapping during ammonolysis or where the electrodes were placed leaning against the alumina boat. To avoid this, the electrodes were carefully placed leaning against the crucible with as much free volume as possible around them. Placing them at an angle against the side of the boat was found to work best, with a small space between them so that they did not overlap. This allowed four electrodes to be fired at once, owing to the size of the crucible boat required to fit inside the silica furnace tube.

The procedure for preparing the VN electrodes was identical, but for the use of vanadium metal (0.25mm, 99.96 %, Goodfellow) and a dwell temperature of 900 °C during heating instead of 1000 °C used for Ti, owing to the lower thermal stability of VN when compared to TiN.[78]

5.2.2 Surface treatment of electrodes.

The electrodes were surface oxidised, as transition metal oxides have increased redox reactivity when compared to nitrides owing to weaker bonding between the metal cationic centres and the O^{2-} anion vs the N^{3-} anion.[116] These have been studied in the literature for charge storage applications.[106, 117, 118] A variety of methods were employed in order to establish the basic methodology that produced the surface oxide layer exhibiting the optimal surface oxide layer depth and speciation by giving the highest specific capacitance. This basic methodology could be further examined, at a later date, to optimise it in terms of finding the highest specific capacitance conditions.

The electrodes were treated in batches of four in the following manners:

As Prepared: Left in sealed sample vials under air until cycled.

Thermally oxidised: The set of electrodes was heated to 300 °C in air for 10 h in a an oven in an alumina boat before being allowed to cool to room temperature to grow a layer of surface oxide. These were stored in a sealed,

snap top sample vial under air until cycled. This has been shown to be a temperature at which the conduction of the film is not affected by a layer of surface oxide.[119]

Cyclic voltammetry oxidised: The electrodes were placed into a KOH_{aq} (6M) cell with a fine Pt gauze counter electrode and a Hg/HgO reference, and 10 cyclic voltammetry cycles were applied at 100 mV s^{-1} between 1.2 V and 0 V vs Hg/HgO. As the electrode approached more positive potentials, gas evolution was observed around the electrode. The electrodes were removed from the cell, rinsed with DI and patted dry using tissue paper before being left to completely dry on clean tissue paper. These were stored in a sealed, snap top sample vial under air until cycled.

Potential Step oxidised: The electrodes were placed into a KOH_{aq} (6M) cell, as before, and the potential of the cell was raised to 1.2 V from the open circuit potential vs Hg/HgO and maintained for 100 s. Gas evolution from the electrode was observed throughout the experiment. Once the oxidation was completed the electrodes were removed from the cell, rinsed, dried and stored in the same manner as the CV oxidised electrodes (detailed above).

The conditions (potential limit) for the electrochemical oxidation were chosen in part by examining the literature[105] and by cycling a representative electrode over the stable window for the chosen electrolyte (6M KOH). The range was then chosen so as to give a normal capacitive response at negative potentials and a positive potential that just started to show a non-reversible reaction. This reaction was deemed to be due to the hydrolysis of water and oxidation of the electrode.

5.2.3 Electrochemical evaluation of metal nitride foil electrodes.

All electrodes were cycled under the same conditions, over a series of scan rates in the sequence 1000, 1, 5, 10, 50, 100, 500 and 1000 mV s^{-1}, with 10 sweeps at each rate. A more detailed version of this procedure can be found in section 2.2.2 above. The initial 1000 mV s^{-1} rate was performed to assess any change in the capacitance of the electrodes on cycling.

5.2.4 Specific capacitance calculations for metal nitride foils.

The cyclic voltammagram for each cycle was integrated to find the total charge passed (A V). This area was divided by two as the cycle has a positive and negative half before being divided by the scan rate of the cycle being analysed (A V s^{-1}). This value was divided by the surface area taken from the AFM (A V s^{-1} cm^{-2}) and the potential window (A V s^{-1} cm^{-2} V^{-1}) for the experiment to give the specific capacitance in F cm^{-2}. Finally, this value was converted to μF cm^{-2}.

Percentage change values for each electrode surface were calculated from the first cycle of the 1000 mV s^{-1} cycles and the last cycle of the final set of 1000 mV s^{-1} cycles, 90 cycles later.

5.3 Characterisation of metal nitride foils.

The experimental procedure, as described in the literature,[23] produced films rich in Ti_2N species, as suggested by XRD. In order to remedy this, the dwell temperature of the procedure was lowered by 100 °C from 1100 °C to 1000 °C. This produced films with a TiN rich surface (Figure 48), with crystallites of Ti_2N submerged a significant depth below (Figure 48). This is shown by the higher incident angle scans showing more Ti_2N. At higher incident angles, the X-ray photons will penetrate deeper into the sample surface before being diffracted from the sample towards the detector. So, if a species is visible at higher incident angles and not or less visible at lower angles then it is present only below the surface within the penetration depth of the incident beam at the steepest incident angle. No peaks from the base metals were seen, suggesting that they were significantly below the surface and below the penetration depth of the incident X-ray beam.

The knowledge gained from the preparation of TiN electrodes was used to inform the preparation of VN electrodes, and the temperature that the electrodes were heated to was lowered to 900 °C from 1000 °C used for TiN.[78] This produced films that showed VN on the surface and present to a significant depth below this surface (Figure 48, lower two patterns).

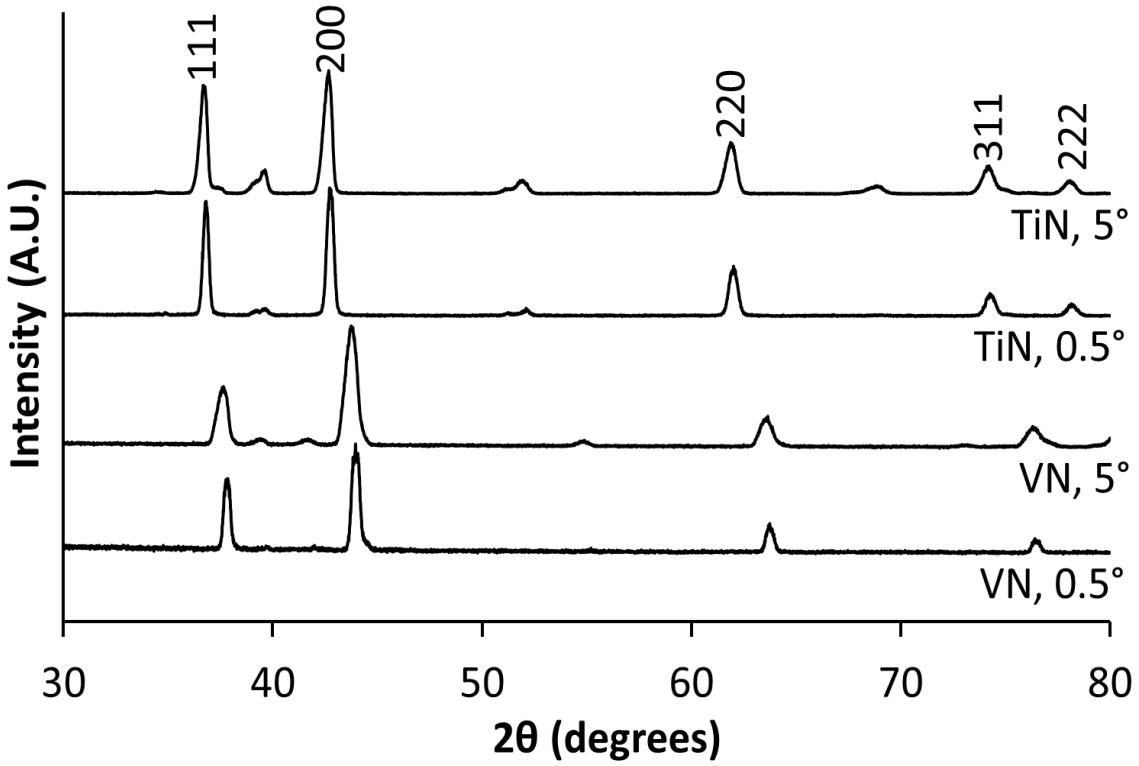

Figure 48: Grazing incidence XRD of TiN_x electrodes at 5° (top) and 0.5° (upper middle) incident angles, heated to 1000 °C under flowing ammonia for 10 hours and VN_x electrodes at 5° (lower middle) and 0.5° (bottom) incident angles, heated to 900 °C under flowing ammonia.

The most intense peaks (labelled as their Miller indices for TiN 5°) correspond to TiN and VN on the respective traces.[65] The smaller, unlabelled peaks correspond to Ti_2N and V_2N. No peaks originating from the base metals were seen.

5.4 X-ray photoelectron spectroscopy.

As explained in section 2.3.7 above, XPS is a very surface selective technique capable, with a significant degree of interpretation, of showing the full range of base chemical environments in the top few nanometers of a surface. When combined with chemical knowledge of the processes that potentially may be occurring at the electrode surface, this can be highly informative as to what processes are occurring. This knowledge can then, be used to monitor alterations to the surface and achieve a higher specific capacitance.

Nitrides can form a passivated oxide surface layer on exposure to air.[42] This oxide layer can provide a more redox active surface for interaction with the

electrolyte. Owing to the surface specific nature of this layer, surface sensitive techniques are invaluable for investigating the chemical composition of the active layer. X-ray photoelectron spectroscopy provides this surface selective analysis of chemical environments. The macroporous nature of the desired films means that directly imaging the films is useful for assessing the degree of long range order of both the templates and the inverse opal structures produced from them. The surface roughness can also be assessed by directly imaging the surfaces. This will be done using scanning electron microscopy. As the films produced will be of the order of microns thick with only a fraction of that being crystalline material due to the structure, conventional powder X-ray techniques in symmetrical geometry will give a significant contribution from the sample substrate, which may mask the intensity of the desired peaks. This means that asymmetric, grazing incidence angle techniques will be preferable.

A variety of approaches have been utilised by others[120-123] in an attempt to find the best method to model XPS data acquired from TiN samples. The explanations for these approaches range from those based on the quantum nature of the energy levels to 'because it seems to work'. Various rules can be derived from the quantised nature of the possible energy levels around an atom from which photoelectrons can be emitted. These include relationships between peak areas (indicating the total number of electrons from the corresponding energy level) and the full width half maximum (FWHM) values that pairs of peaks should have. For example photoelectrons emitting from the 2p energy level can be from one of three different orbitals, two bonding and one anti-bonding. This implies that the number of photoelectrons will be in a 4:2 ratio relationship as they will have an equal chance of being ejected from the sample surface; four electrons will be at the bonding level and two will be at the anti-bonding. This is commonly simplified to a 2:1 ratio. This is sometimes tweaked to improve the fit of the model to the collected data and this 2:1 ratio is typically not adhered to absolutely.

The first stage of collecting any data from a sample consists of a low resolution scan of the entire energy range available from the spectrometer to see what elements are on the surface of the sample, known as a survey scan (Figure 49). This allows for higher resolution scans to be conducted over a selection of much narrower energy ranges to investigate the environments of those elements.

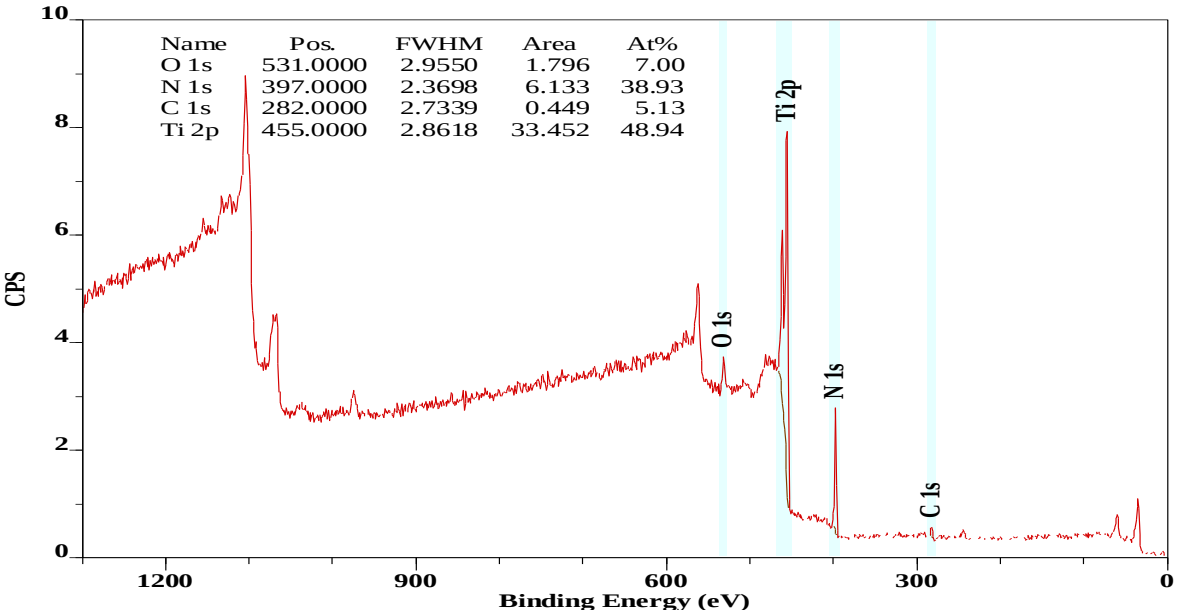

Figure 49: A survey scan of a TiN surface, with the O 2s, Ti 2p, N 1s and C 1s photoelectron emission regions highlighted.

Owing to the sensitivity of the technique, it is possible to see trace contaminants on the samples very easily. These can be from a variety of sources. Carbon species are encountered most frequently as a contaminant from the vacuum pumps used to generate the ultra-high vacuum necessary for the technique to be used. Carbon containing species can also be transferred to the sample surface from incorrect handling, as well as, in the case of these nitride samples, from carbon incorporated into the structure of the nitride as 'carbonitride' species. Fortunately, the distinction between hydrocarbon grease (formally C^{4+} to C^{0}) and carbide (formally C^{4-}) is clear as there is an easily resolvable energy difference between the numerical values for these peak binding energies. Carbide was not present at the surface of the samples upon which XPS was conducted and was unobserved in the XRD patterns. The XPS spectra collected are subject to a whole range of factors that affect the Fermi

level in the machine at any given time, especially the charging of non-conductive samples. This means that the absolute values for the elemental peaks can 'wander' over a small eV range. As a result of this, a reference point is chosen that represents the same elemental environment. For non-etched samples, this environment was chosen as the one from the carbon in the hydrocarbon species in the pump oil. It was universally present in all the samples and displayed the same observed peak height and shape, so the peak value was set as 284.9 eV.[120] On the etched samples this contaminant peak either, was not visible or easily identified. As a result of this, the samples that were etched were referenced to the $2p_{3/2}$ Ar peak at 248.4 eV,[124] resulting from Ar ions being incorporated into the sample surface during the etching process.

5.4.1 X-ray photoelectron spectroscopy of TiN and oxidised TiN surfaces.

The observable Ti 2p environments found on the surface of TiN species are shown for all four surface treatments in Table 6 below.

The development of a model that would fit the spectra started with the analysis of a TiN sample etched to remove as much oxide as possible. This was chosen as it is a far simpler system to deconvolute than analysing a spectra containing a larger number of environments, that arise from the variety of Ti-O, TiN and Ti(O,N) species that might be present. The spectra with the model developed can be seen in Figure 50.

From Table 6, it is clear to see that the potential step oxidation of the surfaces gave the highest percentage of oxide species on the surface of the electrode, with cyclic, thermal and native oxidations giving oxidation levels in descending order. This correlates with the obtained specific capacitances of the electrodes (also in Table 6) and with the 'As Prepared' samples giving the highest capacity.

Table 6: The surface proportions of different Ti 2p environments by XPS and the specific capacitances from each surface treatment when cycled in 1M KOH at 100 mVs^{-1}.

The specific capacitance values shown are from the 3rd cycle of each set.

Surface species percentages by XPS (%)					
Sample	TiN	Ti(N,O)	TiO_2	TiN shake-up	Specific Capacitance at 1 mV s^{-1} (μF / cm^{-2})
TiN	38	26	33	3	362
TiN pot. step	3	8	89	-	293
TiN CV	3	10	87	-	14
TiN thermal	21	37	42	-	235
TiN etched	82	3	0	15	-

To understand why the 'as prepared' electrode provides the highest specific capacitance, a detailed analysis of the oxide and Ti environments present at the electrode surface was conducted. The model generated to fit the data fits with a residual standard deviation or 'R' value of 0.96 indicating that the model fits the data with a high level of accuracy. Whilst it was possible to build a model that fit the data very slightly better (R = 0.966), this involved breaking a few rules of the quantum nature of the atom. The $2p_{1/3}$ and $2p_{2/3}$ peak pairs needed to no longer obey their 2:1 ratio relationship for a higher R value fit. This suggests that the model used is accurate and sensible in terms of the allowed physics of a metal centre.

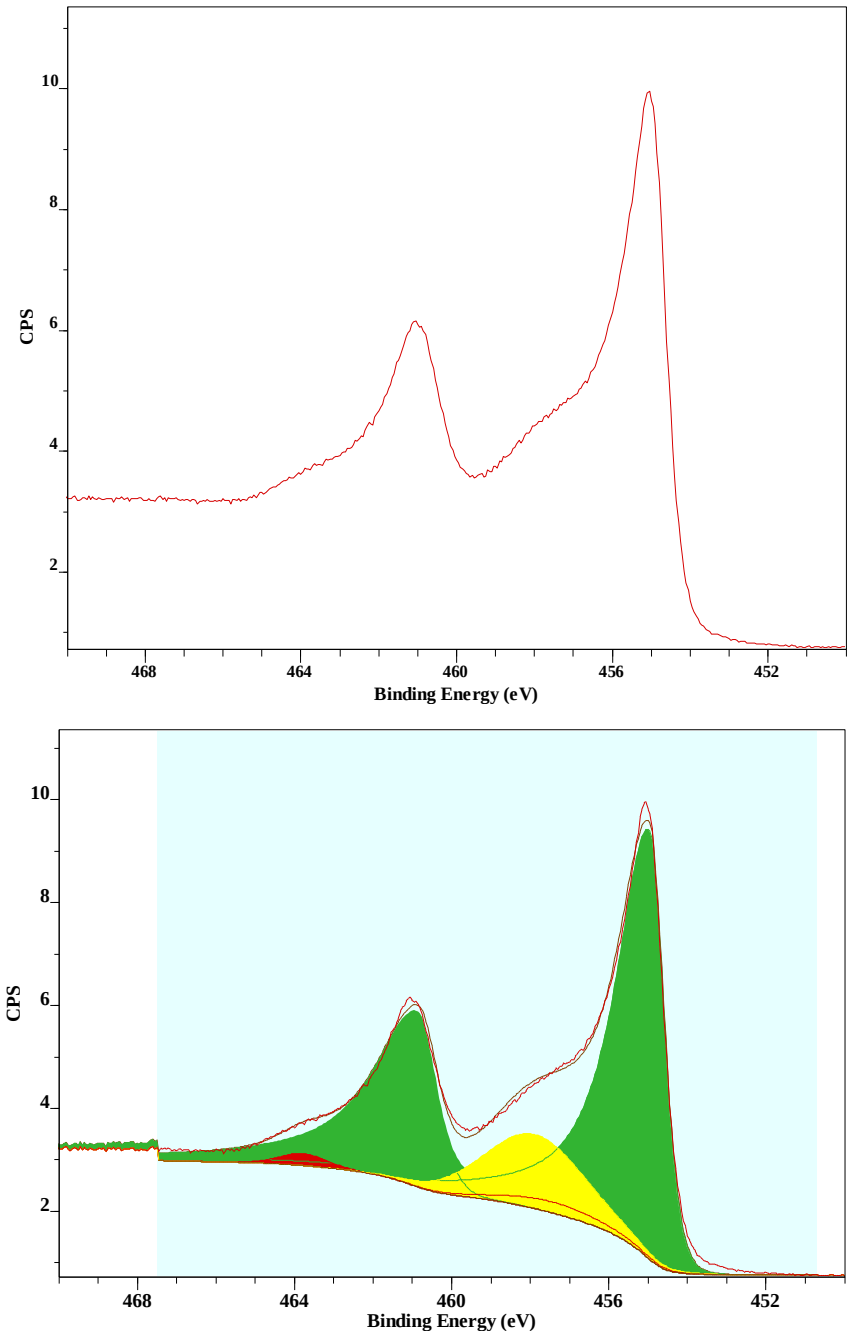

Figure 50: Raw data (top) and deconvoluted XPS (bottom) spectra of the Ti 2p region, showing a heavily etched TiN surface.

The X axis corresponds to an arbitrary count measurement, the Y axis to the binding energy of the electrons to the metal surface (eV). The surface was etched by argon ion bombardment for 40 minutes at 4 keV to remove as much surface oxide as possible.

The green area corresponds to photoelectron emission from Ti atoms in a Ti^{3+} environment most likely TiN, the yellow corresponds to a plasmon shake up peak derived from the TiN peak, due to the unpaired electron from the Ti^{3+} centre. The red corresponds to the trace Ti(O,N) species remaining on the surface that proved impossible to remove under the conditions employed.

The spectra of the etched sample that this model was developed upon can be seen in Figure 50. It consists of an asymmetric doublet from Ti^{3+} at 455.1 eV for the $2p_{3/2}$ excitation and at 461.1 eV for the $2p_{1/2}$, the $2p_{3/2}$ peak has a 'shake-up' peak at slightly higher energy 458.7 eV (the yellow peak in Figure 50). These are all assigned to Ti environments associated with TiN.

In unetched samples, this shake up peak at 458.7 eV is coincident with a broad, symmetrical doublet spanning the energy range expected from Ti^{3+} to Ti^{4+}, from the variety of Ti(N,O) environments.[120] Initial etching reduced the relative intensity of this Ti(N,O) environment from 26% to 3% and a reduction of surface TiO_2 from 33% to an undetectable amount, along with a reduction in the surface oxygen percentage from 38% down to 7% of the total. This suggests that the majority of the oxygen on the sample is present as a thin surface layer of passivated material.

Angle resolved measurements, where the angle of the sample is tilted relative to the incident X-ray beam and electron analyser, support this (Figure 51). Attempts to completely remove the surface oxygen by further etching did not result in a lowering of the surface oxygen concentration or the complete removal of the Ti(O,N) peak (Figure 51). This suggests that the oxygen is, either, present all the way through the sample or that the reactive sites left by the etching of the surface react with the removed oxygen before it can diffuse away into the vacuum of the instrument.

This model suggests that there are a wide range of oxide environments around the metal atoms irrespective of the surface treatment methodology employed. These fall into the energy ranges associated with TiO_x, Ti(O,N) and TiN environments.

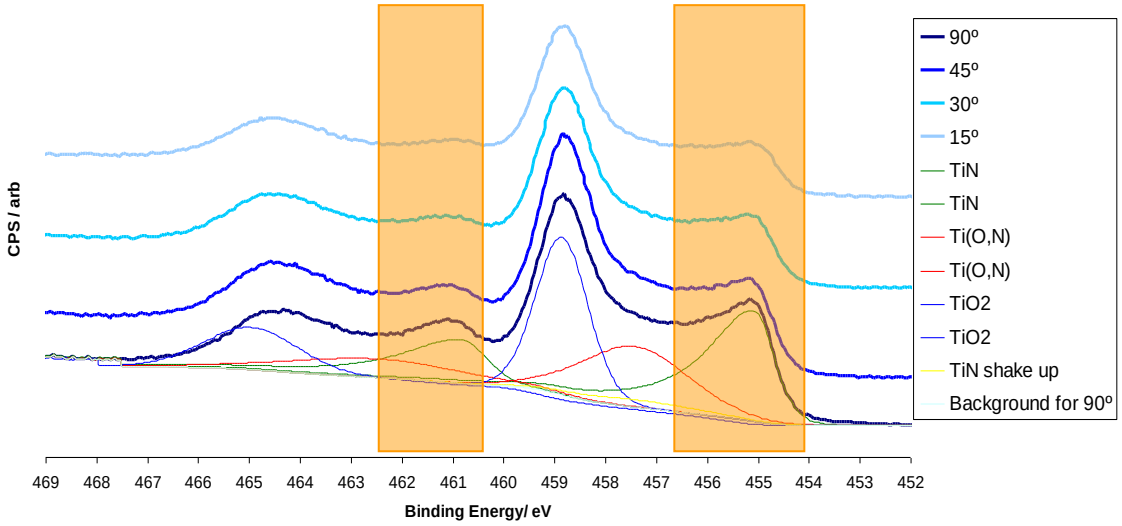

Figure 51: A stack plot showing angle resolved XPS spectra on a TiN surface at 90º, 45º, 30º and 15º to the incident X-ray beam.

The peak for the TiN 2p emission at 455 eV and 461 eV becomes much less defined as the angle is reduced (highlighted in orange), suggesting that it is present deeper down in the sample surface than the TiO_2 component (at 459 eV and 464.5 eV) of the spectra. The X axis units are arbitrary, the shape and height of the peaks should be compared with one another.

With the potential step oxidation surface treatment, it can be theorised that the oxidation was conducted at a potential that allowed a variety of environments to be generated at the surface, rather than creating a more unique species as was intended. However, the majority of the atoms at the surface are of a Ti^{4+} species and concurrent with the energy range and peak shape associated with TiO_2.

A similar trend was observed with the thermally oxidised sample. A range of oxide environments were formed leading to a change of the specific capacitance. However, a much higher surface percentage (Table 6) of Ti^{4+} species were present, accompanied by an increased level of surface oxide species. This, in conjunction with the energy ranges these peaks are across, implies that a higher percentage of the surface atoms are TiO_2. This suggests that the less conductive nature of the oxide species is restricting the flow of electrons to or from the surface of the sample and, as a result, restricting the amount of charge that can be compensated for, leading to the observed drop in specific capacitance when compared to the 'as prepared' and potential step oxidised samples.

The cyclic voltammetry oxidised electrode surface displays a similar level of oxidation to the potential step oxidised surface with only a 2% difference between the two surfaces in the amount of Ti^{4+}/TiO_2 environments. These minor differences correspond to a significant change in the specific capacitance delivered by the two surfaces. The major difference between them is in the surface areas of the electrodes created by the two oxidation methods. This can be seen from the AFM study conducted on the set of samples (See section 5.5 below).

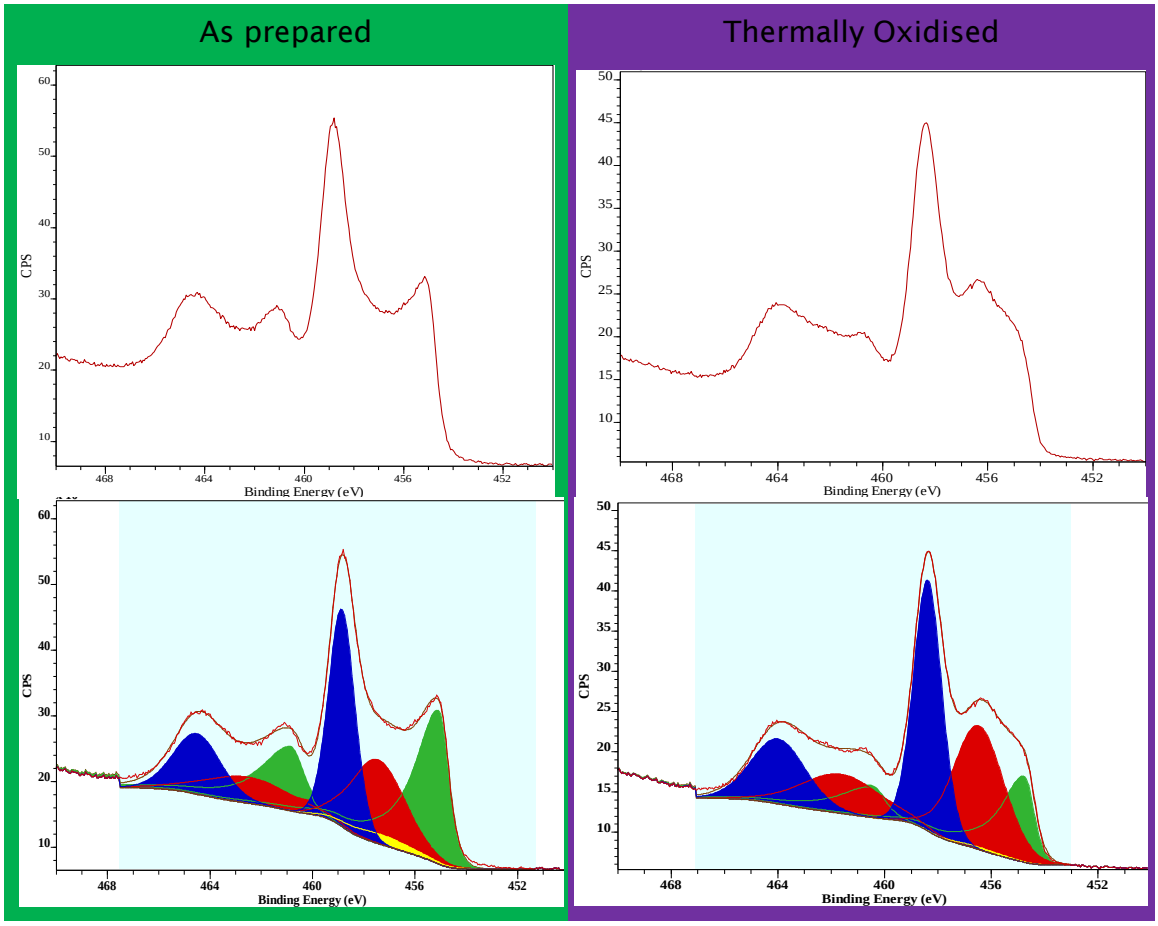

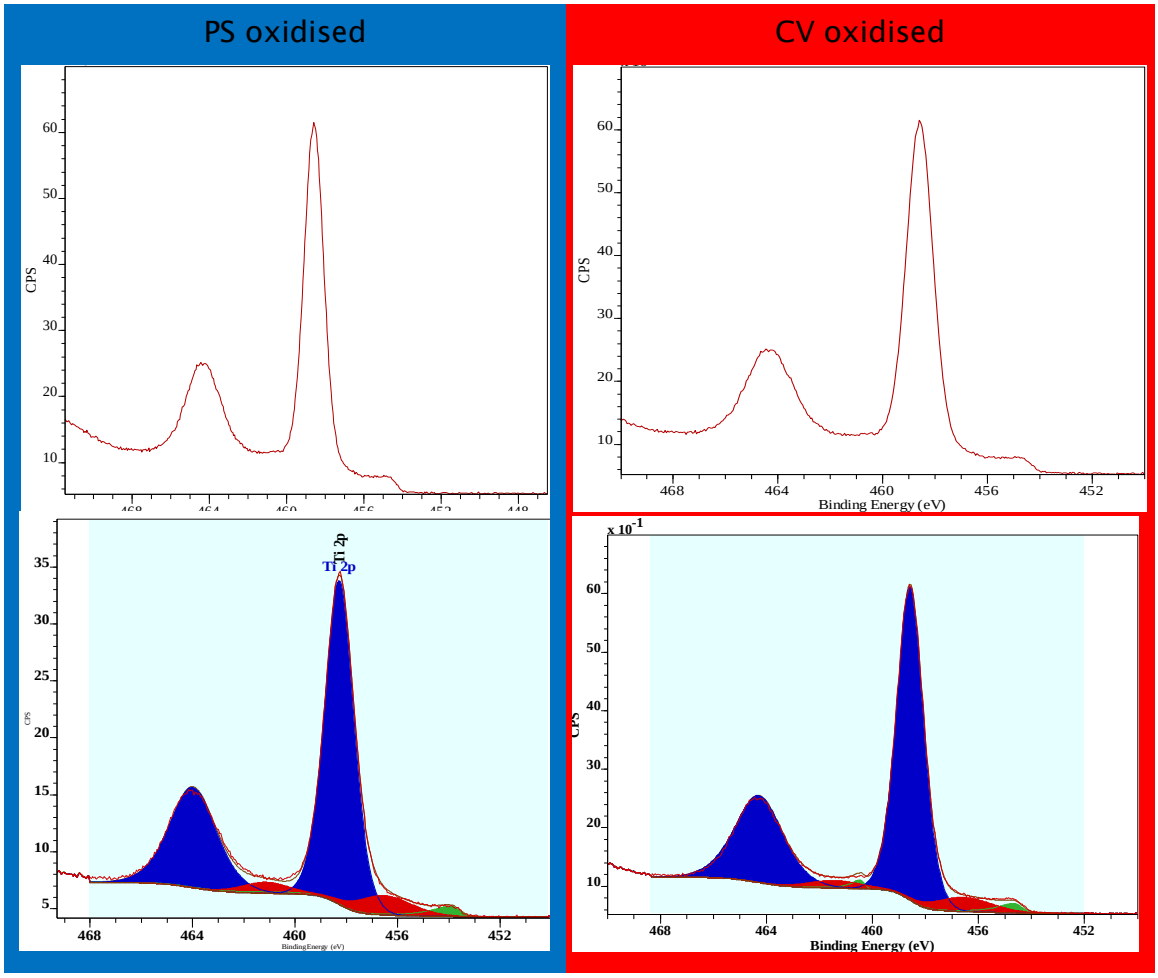

Figure 52: XPS spectra of the Ti 2p energy range on each of the four treated TiN electrodes showing raw and fitted data for each surface.

The energy range is from 468 eV to 452 ev along the X axis. Green peaks correspond to photoelectrons from TiN, blue peaks correspond to emissions from TiO_2 environments, red peaks correspond to 'Ti(O,N)' species. The yellow peaks correspond to the TiN 'shake up peak' and is coincident with the Ti(O,N) peak. The back ground colours for each spectra correspond with the colours used for CV's and AFM images further on in this chapter. The concentrations of each of the environments can be found in Table 6.

The 'as prepared' surface, the surface that had been passivated only by exposure to the atmosphere, showed the highest specific capacitance and the lowest level of surface oxides (Table 6). This suggests that air exposure generated surface oxide can provide a significant increase in the specific capacitance of TiN surfaces. This benefit does, however, only occur under certain conditions. These are certain speciation combinations present at the

surface or levels of oxidation, as demonstrated by the differing specific capacitances achieved from the differing surface treatments. Whilst this study has demonstrated that the simplest oxidation procedure can produce a significant percentage increase in specific capacitance (Table 6), it has not isolated the exact reason for this increase.

5.4.2 X-ray photoelectron spectroscopy of VN and oxidised VN surfaces.

GI XRD measurements on the nitrided vanadium foils showed that, similar to the nitrided Ti foils, a thick surface of VN was produced with crystallites of V_2N protruding into it from below. At 0.5 º incident angle the XRD spectrum shows only VN, a sharper incident angle of 5 º shows a V_2N phase in addition to VN (Figure 48).

Whilst there is literature available for fitting V systems,[120] it is mainly based on VO_x species. This literature was a valuable source of information, however, it is less than ideal as there exist a significant number of differences between the O^{2-} and N^{3-} anions, such as the coulombic charge associated with each. The same rules as apply to Ti centres can be applied to V centres to develop a suitable model for the data.

The survey scan of a VN surface showed V, N, O, C the majority of the surface is composed of vanadium, nitrogen and oxygen, with carbon present as a trace element from the vacuum system of the instrument.

The V 2p spectrum (Figure 53) for an 'as prepared' and atmosphere exposed VN surface consists of two doublets, representing V^{III} at ~514 eV and V^{V} at ~517 eV. A further peak appears at 515 eV, which corresponds with the reported position for V^{IV} $2p_{3/2}$ species, however, a matching $2p_{1/2}$ peak could not be fitted with good confidence. It is possible that this peak corresponds to a 'shake up' peak for V^{III} in a similar manner observed for TiN. The $2p_{3/2}$ and $2p_{1/2}$ peaks are separated by 7.5 eV and 7.3 eV, respectively. Additionally, included into the background region are the O 1s peaks at around 530 eV, as these are close enough to have an effect on the background contribution for the V 2p region. Etching of this surface resulted in the majority of the surface being reduced to vanadium metal (Figure 54). This is as a result of the conditions employed to etch the samples.

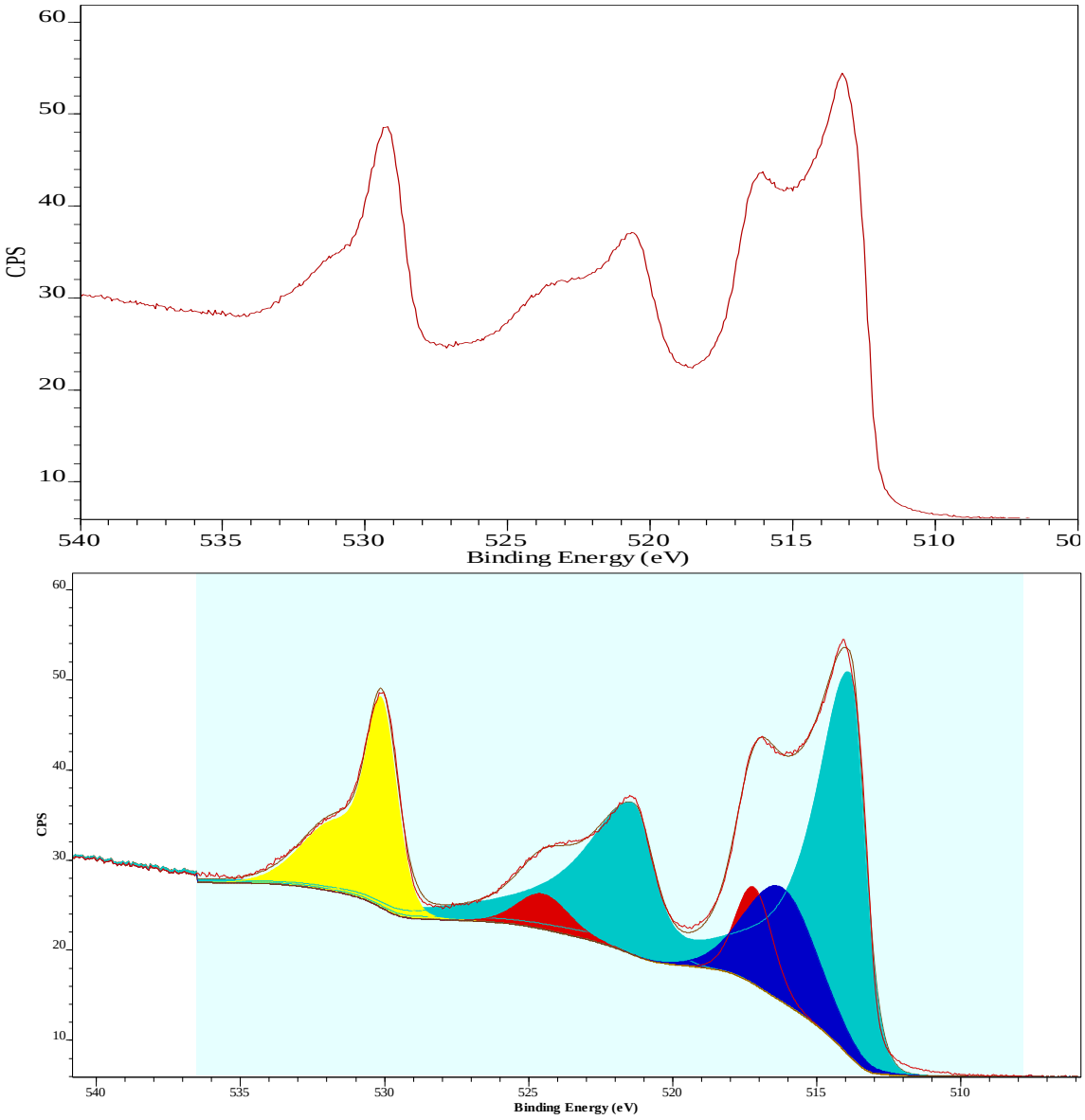

Figure 53: A high resolution XPS spectrum showing the V2p and O1s regions both without (top) and with (bottom) synthetic components fitted.

The light blue peaks correspond to VN, red peaks correspond to a V^{V} species most likely an oxide or oxynitride. The dark blue peak is most likely a shake-up peak from the V^{3+} (VN) environment, its position corresponds with literature values for V^{IV} species, however, it is missing its $2p_{1/2}$ component. The yellow peak corresponds to O 1s emissions from the surface oxide layer on the sample.

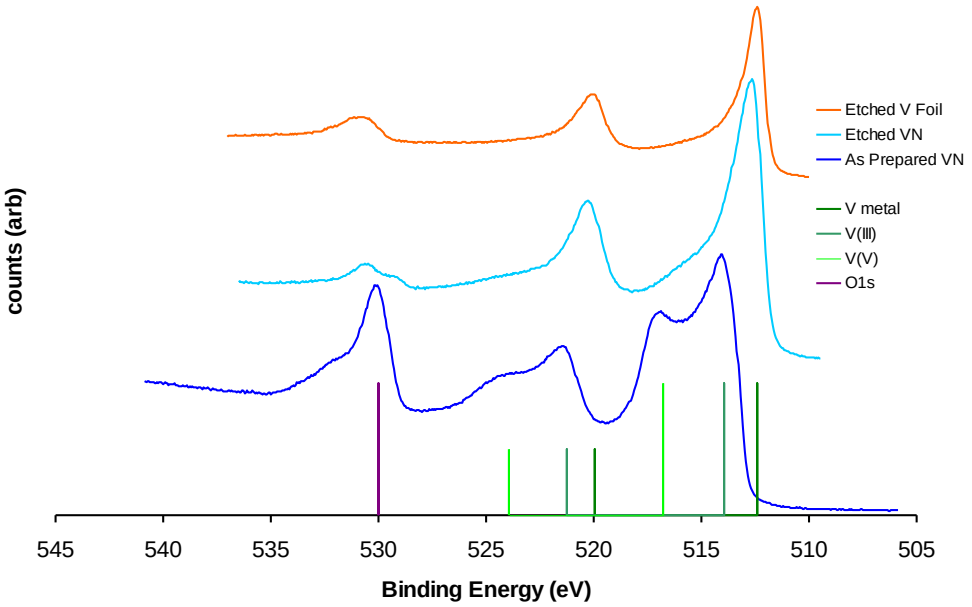

Figure 54: A stack plot showing a series of high resolution scans of the V 2p and O 1s photo electron emission region.

The dark blue spectrum shows the as prepared, atmosphere exposed VN surface prior to etching. The light blue shows the same surface after 20 minutes etching with 4 keV Ar^+ ions, which lead to the majority of the surface being reduced to vanadium metal with traces of V^{III} and V^{V} left on the surface. The orange spectrum shows an un-nitrided piece of vanadium metal after etching under the same conditions to remove most of the surface oxide layer.

Thermal treatment of the VN surface in air caused the foils to turn from metallic grey to having a purple sheen on the surface (Figure 58). The binding energy of the largest emission suggests that this is a V^{V} species as the surface of these samples is almost entirely (95%) V^{V}. In conjunction with the relative proportion of oxygen on the surface this suggests that there is a thin film of V^{V} oxide at the surface of this sample (Figure 55).

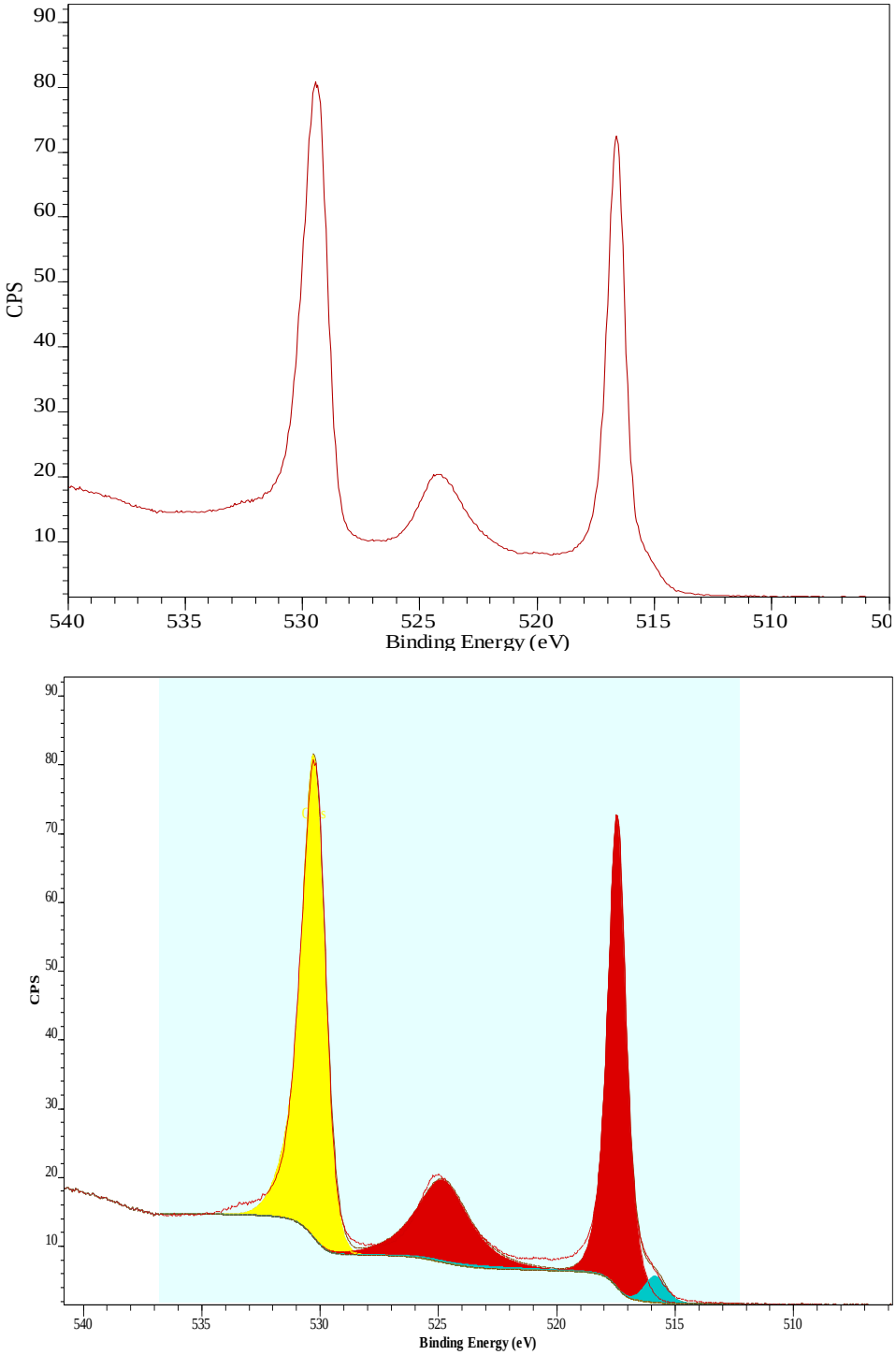

Figure 55: A high resolution XPS spectrum showing the V 2p and O 1s regions with (bottom) and without (top) synthetic components fitted for a thermally oxidised VN surface.

The peak colours are the same as for Figure 53. Thermal treatment of this surface has produced a thin layer of V^{V} species, accounting for 95% of the vanadium in the sample surface.

Potential step and cyclic oxidation of the surfaces in 6M KOH has, either, reduced the surfaces back towards V^{III} or dissolved any V^{V} species produced from the surface into the electrolyte. The proportion of the surface present as V^{III} species remains approximately constant. However, the proportion of V^{IV} species increases from 16% to 25% (CV) and 27% (PS) with the detected concentration of V^{V} species being 0% and 2% respectively. (Figure 56 and Figure 57).

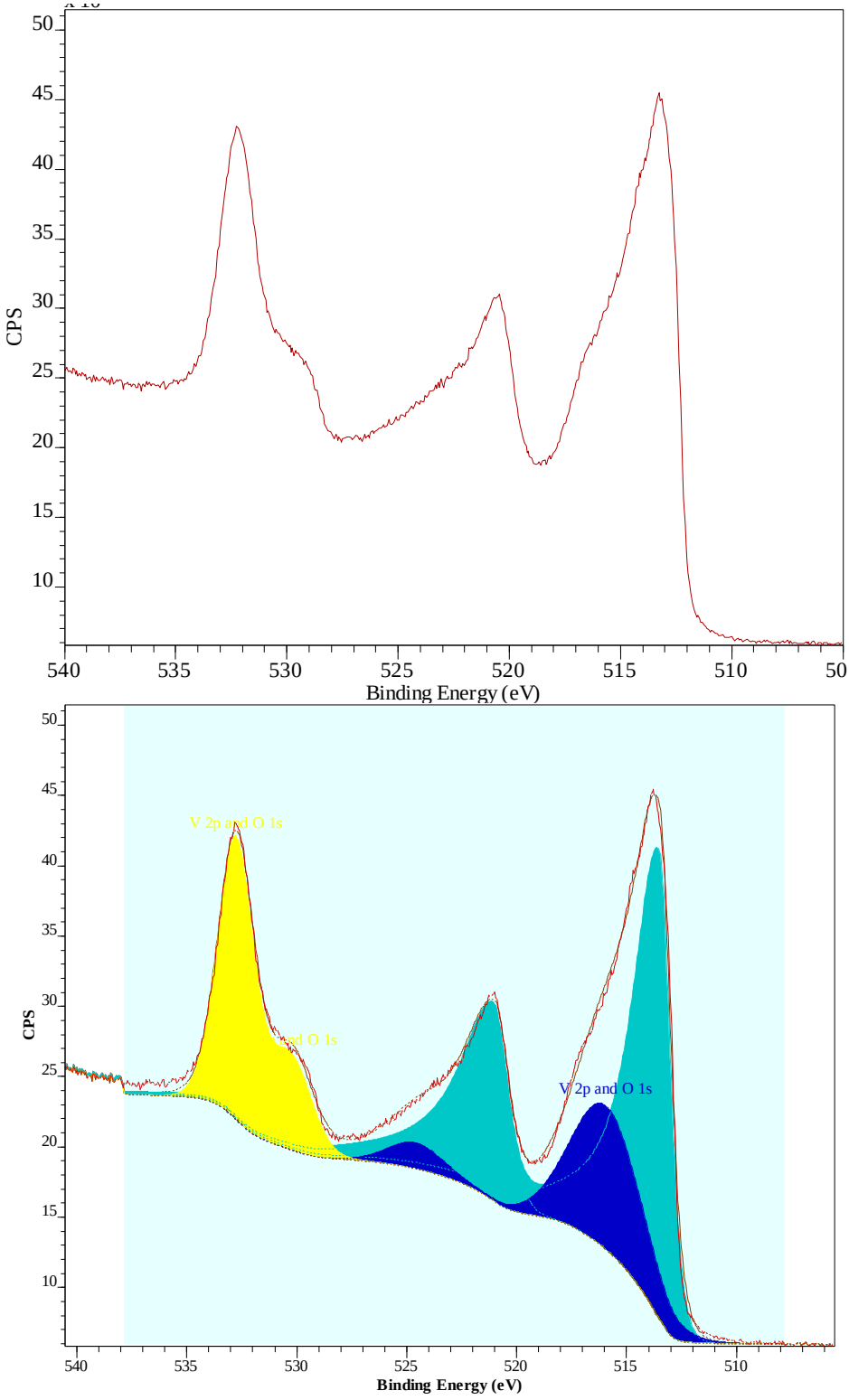

Figure 56: A high resolution XPS spectrum showing the V 2p and O 1s regions with (bottom) and without (top) synthetic components fitted for a cyclically oxidised VN surface.

The peak colours are the same as for Figure 53. CV treatment of this surface has stripped the V^{V} species from the sample.

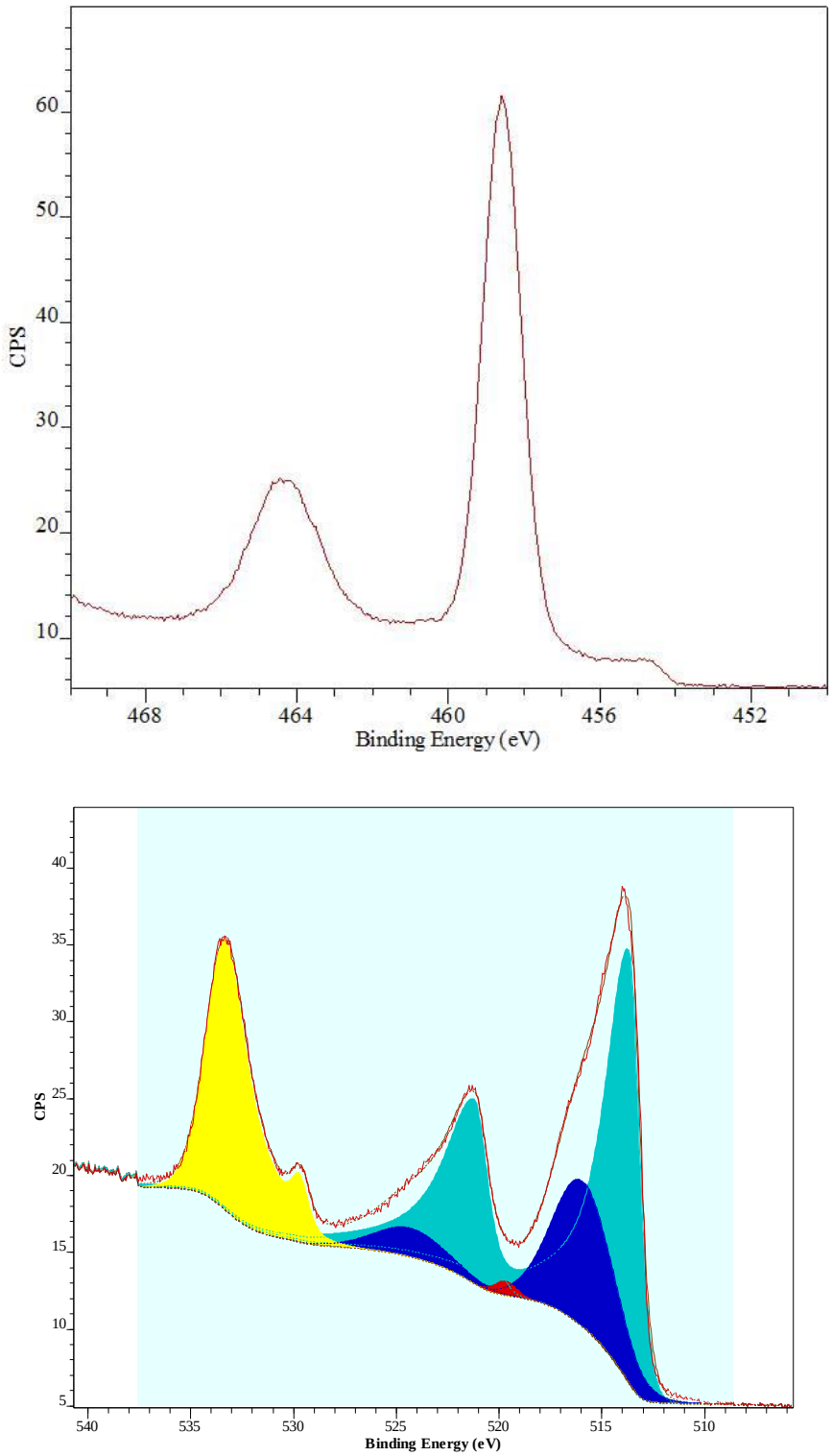

Figure 57 High resolution XPS spectra showing the V 2p and O 1s regions with (bottom) and without (top) synthetic components fitted for a potential step oxidised VN surface.

The peak colours are the same as for Figure 53. In a similar manner to the CV treated surface, potential step treatment of this surface has stripped the V^{V} species from the sample.

Table 7: A table summarising the surface concentrations of vanadium environments from the four different post synthesis treatments with the specific capacitances from the 4th cycle of 10 being cycled in 1M KOH at 1mV s^{-1}.

The surface percentages were measured from the 2p emission regions by XPS.

	Surface percentages by XPS (%)			Specific capacitance at 1 mV s^{-1}
Sample	VN	V^{IV}	V^{V}	(μF cm^{-2})
VN as prepared	73	16	11	48.2
VN pot. step	71	27	2	46.3
VN CV	75	25	-	57.06
VN thermal	5	-	95	63.0

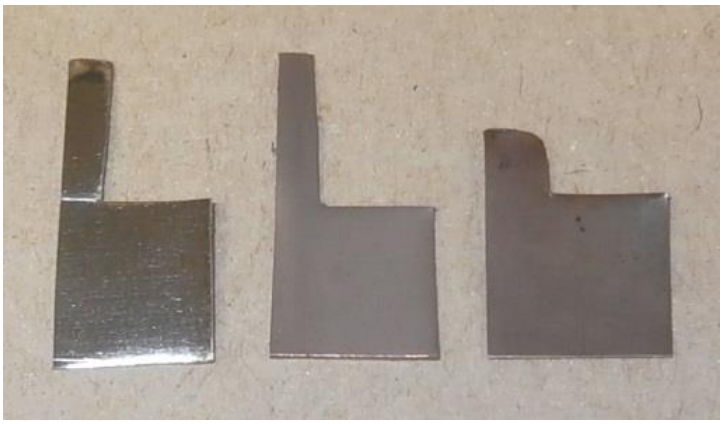

Figure 58: A photograph of vanadium based electrodes, showing vanadium metal (left), VN (middle), and thermally oxidised VN (left).

Notice the slight purple sheen of the thermally oxidised VN sample. This was more apparent on some samples but dissolved from the surface on cycling.

5.5 Surface morphology of electrodes.

As the XPS results could not conclusively prove what was causing the increase in specific capacitance of the electrodes, imaging of the surfaces was

undertaken to try and understand what could be occurring. SEM was undertaken, revealing (as can be seen in

Figure 60) a variety of surface features visible on the ‘as prepared’ VN surfaces. Knowing that these features could have a significant effect on the surface area of the electrode, AFM (

Table 8) and WLI were undertaken so that an accurate surface area could be calculated.

5.5.1 TiN.

SEM of the TiN electrodes revealed that the surfaces were much rougher than the simple geometric surface area of the foil suggested (Figure 59).

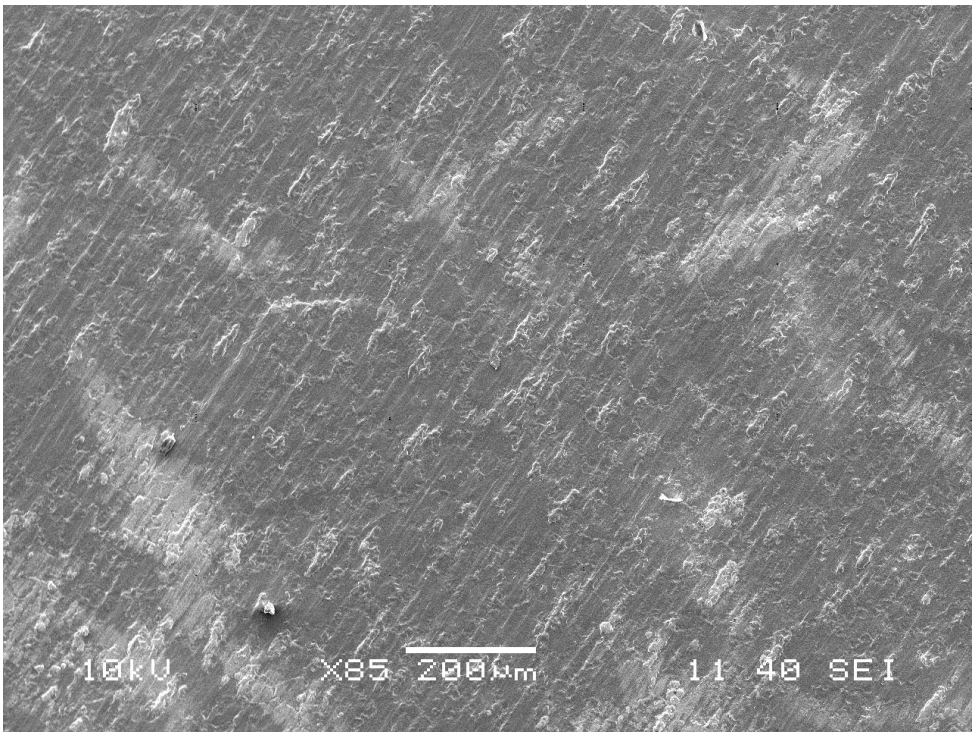

Figure 59: An SEM of an as prepared TiN electrode surface.

Clearly visible are the minor deviations on the surface that generate a rougher than geometric surface area.

AFM of the four different surfaces revealed that the surface areas were fairly similar between the 'as prepared', 'PS' and 'thermally' oxidised surfaces. However, the CV oxidised surface showed a much higher surface area by AFM (Table 9).

Table 8: AFM micrographs of the oxidised TiN and VN surfaces, examples of which are shown in Figure 46 (right image).

Each image shows 1 μm^2 of the surface of each electrode. The colour scale shows the height variation of the surface, darker shades indicate that the AFM tip had to travel 'deeper' to encounter resistance.

	TiN	VN
As prepared	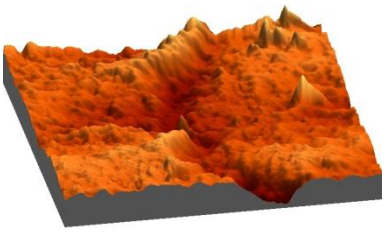	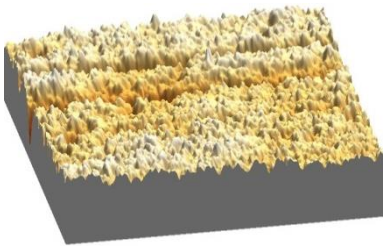
Cyclically oxidised	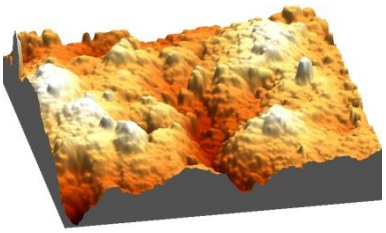	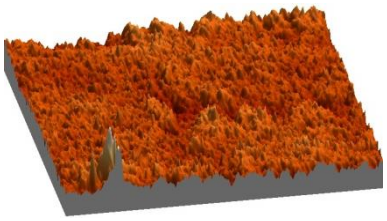
Potential step oxidised	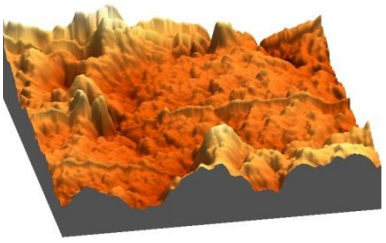	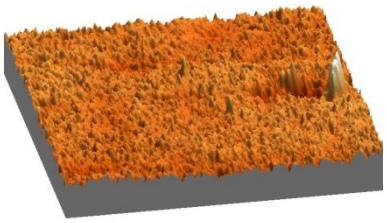
Thermally oxidised	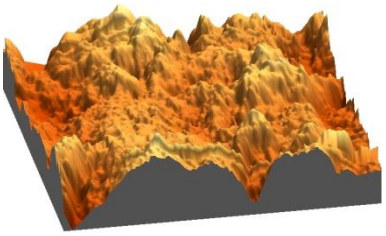	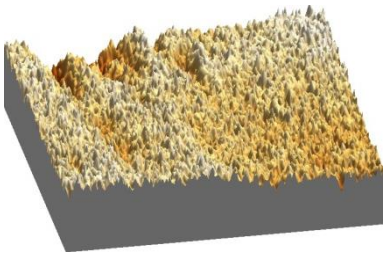

Table 9: The surface areas of the oxidised electrodes calculated from the AFM data.

The surface area was calculated from the per μm^2 surface area value given by the AFM and scaled up to per cm^2, before that value is multiplied by two as the electrode has two sides.

The WLI surface roughness value is the sum of the differences (in nm) in surface height from a nominal zero height on the generated spectra, the rougher the surface the higher the number. It gives an idea of how flat the surface is.

These values were combined to give a 'total surface area value' by squaring the WLI roughness value and averaging it with the surface area value from the AFM measurements.

Sample	AFM Surface Area μm^2 / μm^2	WLI surface roughness (nm)	Total Surface Area cm^2 / cm^2
TiN As prep	7.0	360.1	14.0
TiN CV Ox	17.2	408.1	18.7
TiN PS Ox	5.1	318	10.2
TiN Thermal Ox	4.8	376.5	9.6
VN As prep	9.4	81	18.8
VN CV Ox	9.9	145.9	19.8
VN PS Ox	8.8	98.0	17.6
VN Thermal Ox	9.8	181.7	19.5

The value for the surface area for the CV oxidised TiN sample by AFM (Table 9) was 34.49 cm^{-2} and is twice the surface area value seen for the other surfaces. This high value from the CV oxidised TiN is also the highest surface roughness given in the WLI data, but not to the same degree. This had the effect of reducing the specific capacitance of the CV oxidised TiN foils considerably when measuring the surface area.

As this was having a disproportionate effect on the specific capacitance value of the CV oxidised TiN samples, an average value, calculated from the surface

area values from the WLI and AFM data, was used. This was thought to be acceptable as variation over the total surface of the electrode may not be accurately representing the whole sample if a region with a tool mark had been chosen for the AFM analysis. If this was the case, then the scaling up operation employed in the total surface area calculation would give the impression of a surface far rougher than it was. For example, if the AFM data acquisition (carried out over 1μm^2) was conducted on an area of the surface that had a tool mark from handling or processing the metal foil, then any surface area deviance caused by the processing would be amplified by 10 orders of magnitude when scaled up to 1 cm^2. As the WLI data was collected from one entire face of the sample, any surface variation caused by these defects from processing would be less influential on the surface area value as a whole. The average total surface area from the two methods still gave the CV oxidised sample the highest surface area and this value was used to calculate the specific capacitance values seen in Table 9.

5.5.2 VN.

Initial SEM of the VN surfaces showed star like features across the surface of the foil, supporting the decision to investigate the surface area in more depth. These star-like features could lead to an increase in the solvent accessible surface area of the foil increasing the surface area of the foil and the specific capacity of the material if not accounted for. However, AFM of the VN surfaces (

Table 8 and Table 9) suggested that although the surface was rougher than the simple geometric surface area suggested, the features seen on the SEM did not provide a huge difference in the surface area of the electrodes.

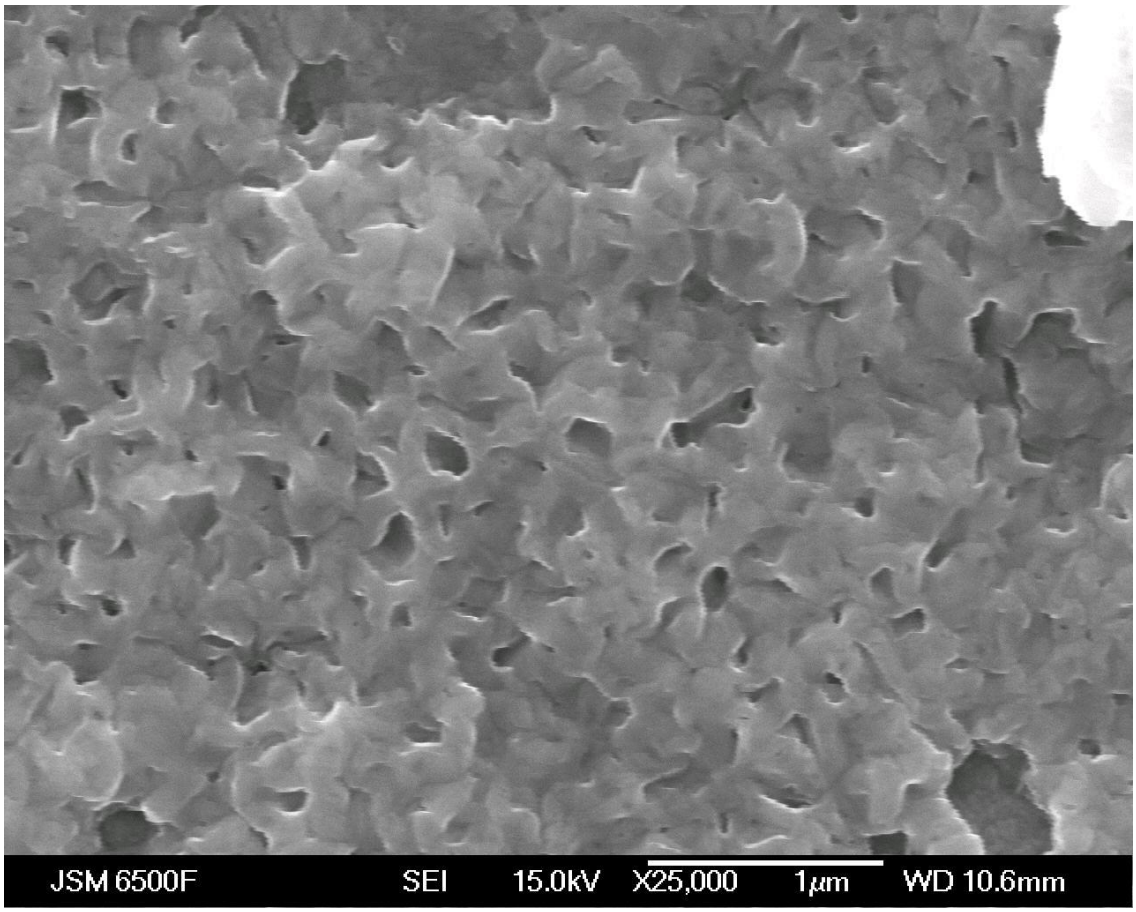

Figure 60: An electron micrograph showing the star like features on the surface of one of the nitrided VN foils. These features will increase the surface area of the electrode.

AFM of the VN surfaces (

Table 8 and Table 9) showed that all four surface preparation methods had produced surfaces with similar surface areas. The variance in the relative colour values on the AFM images is an artefact of sample alignment. Whilst every effort was made to minimise this, some small error in the alignment between the samples was obviously present. The major difference between the VN and TiN surfaces is that the TiN surfaces show a much greater variation in the visible features, whereas the VN surface just looks rough. The difference in the length scales that the AFM and SEM were conducted over, 1 μm^2 and 5 μm x 3 μm respectively, has, unfortunately led to the star like features seen on the SEM being lost on the AFM as they are bigger than the area analysed.

5.6 Electrochemistry of TiN and VN and their treated surfaces.

Capacitors will ideally give a rectangular cyclic voltammetry response. Deviations from this will be due to a small number of rate limiting factors or from resistance causing the 'rectangle' to become a 'parallelogram', displaying an increase in current as the voltage is increased owing to uncompensated resistance in the circuit. These limiting factors can manifest themselves as features such as an IR drop across the whole scan coming from resistance in the circuit. A curve can be seen on the returning corner of the idealised rectangle (Figure 61) as the ions in the electrolyte or electrons in the material surface rearrange to fully compensate for the change in polarity. This movement is limited by the rate of diffusion and the resistance of the material and as a result takes time, leading to the rounded corners. With electrochemically active capacitors, this rectangle has redox peaks attached to the basic shape from the charge storing reactions between the electrolyte and the electrode.

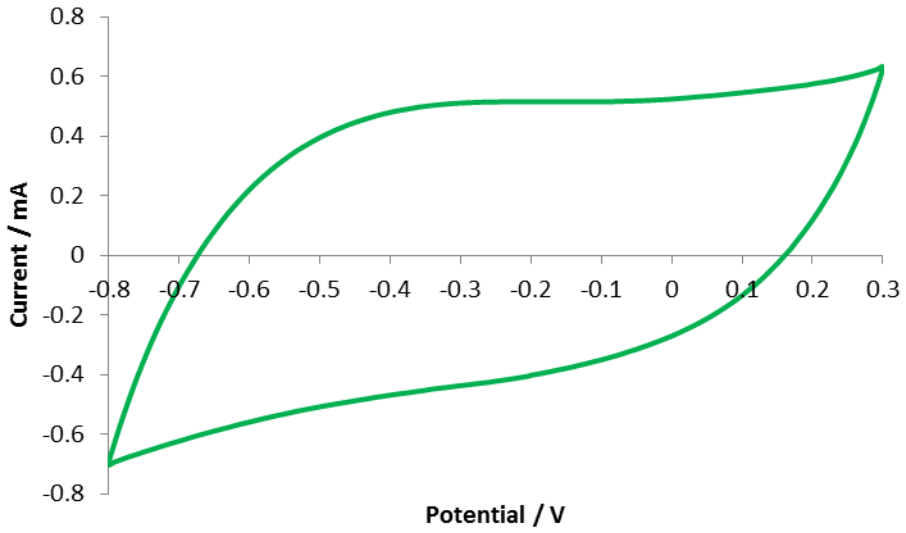

Figure 61: A cyclovoltamagram of an 'as prepared' TiN surface at 1000 mV s^{-1} scan rate in 1M $KOH_{(aq)}$ vs Hg/HgO, showing the rounded corners and rectangular shape exhibited by a double layer capacitor.

Even with all these distortions to the basic 'capacitor response' shape, a capacitance for the electrode can still be calculated from the area inside the CV curve. When combined with, either, the weight of the material used or the surface area of material exposed, this capacitance can be used to calculate a specific capacitance for the material (the specific capacitances for the materials analysed can be seen in Table 6 and Table 7). Since in this work, the electrode surface was the focus and was a small proportion of the mass, it has been convenient to normalise the capacitance values to electrode area (F cm^{-2}) rather than mass (F g^{-1}) as is more common.

Cycling was conducted at a range of scan rates, starting with a fast 1000 mV s^{-1} rate before dropping to 1 mV s^{-1} and increasing in a logarithmic pattern (5, 10, 50, 100…) back to 1000 mV s^{-1}. The specific capacitance vs cycle number plots below are presented with the specific capacitance values (Y axis) on a logarithmic scale.

The oxide layer grown on the MN foil electrodes had a noticeable effect upon the specific capacitance of the MN materials, with a percentage increase of between 2500% (VN Thermally oxidised) and 13% (TiN Thermally oxidised).

5.6.1 TiN.

All TiN electrodes showed no visible chances on cycling.

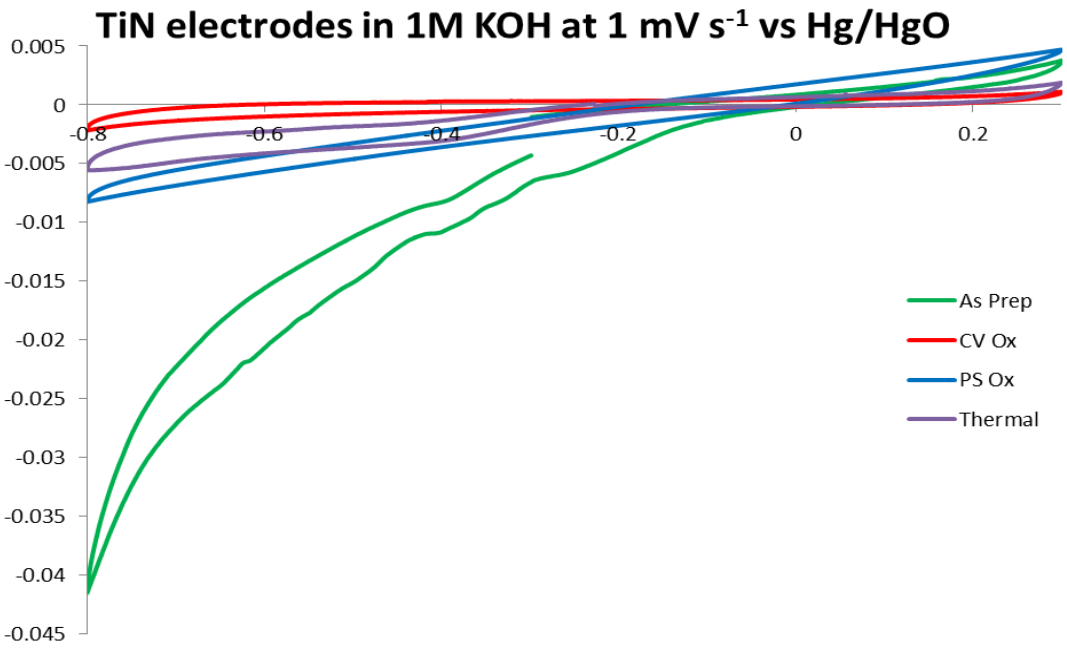

Figure 62: Example CV's from the TiN surfaces in 1 M $KOH_{(aq)}$ at 1 mVs^{-1} scan rate vs Hg/HgO.

All scans shown are the third cycle of ten.

Over the course of these slow scans the area contained within the curve and the capacitance of all the surfaces change quite drastically as illustrated in the second series on Figure 64, Figure 66, Figure 67 and Figure 69. This will be discussed in the relevant sections below.

5.6.1.1 As prepared.

The 'As prepared' sample of TiN exhibited an electrochemical response to cycling reminiscent, at higher rates, to that of a typical capacitor, manifesting as an approximate rectangle with two of the corners rounded (as can be seen in Figure 61). This suggests that TiN stores charge electrochemically, as double layer charging would produce a much sharper, less rounded response, in addition to charge being stored in a double layer fashion. The rounded corners result from a rate limitation to one of the charge compensation processes, either, from the supply of electrons to the electrode surface or more likely as a result of the rate of diffusion of ions from the bulk to the reaction zone in the electrolyte solution.

Another feature observable on the CV scans is an asymmetry between the positive and negative sweeps of the scan. The positive, oxidising, half of the

sweep exhibits a rectangular shape typical of a capacitor. However, the negative, reducing portion of the cycle exhibits a more triangular shape. This suggest that charge is stored as a Ti^{4+} species, which by nature of having no unbonded electrons in its d orbitals, is less conductive than the Ti^{3+} it originated from (TiN). This leads to more charge being passed at the lower potential range than at the higher potential end during the sweep (V=IR) as the surface atoms of the electrode are reduced (This can be seen clearly in Figure 63).

The specific capacitance values for TiN show a massive increase during the set of 1 mV s^{-1} scans. Over the course of 10 scans the specific capacitance for the electrode increased from 361 to 1532 µF cm^{-1} (+ 423 %). A similar, but not so dramatic, increasing trend is observed in the 1000 mV s^{-1} scans recorded immediately beforehand (20 to 30 µF cm^{-1}, + 50 %), yet is not observed in the following sets. The 5 mV s^{-1} set shows a small drop in capacitance over the set (313 to 298 µF cm^{-1}, - 5 %). This steady drop is observed over the remaining series in the experiment. A possible explanation for this could be that one of the 'passivated' oxynitride species present at the surface is reacting with the electrolyte above a certain potential, but this is not apparent on the CV scans. At the lowest potential (> -0.5 V vs Hg/HgO) on the sets of scans with increasing specific capacitance, this can be seen as a region where more charge is passed on the oxidising portion of the scan without a corresponding peak/increase in area on the reductive half of the scan (Figure 63 and Figure 68), suggesting an oxidative (Ti^{3+} to Ti^{4+} reaction is occurring). After a certain point or amount of time above this over-potential threshold, this species is irreversibly consumed from the solvent accessible surface. Once this has occurred, the specific capacitance of the surface stabilises and such huge jumps in capacitance are no longer observed.

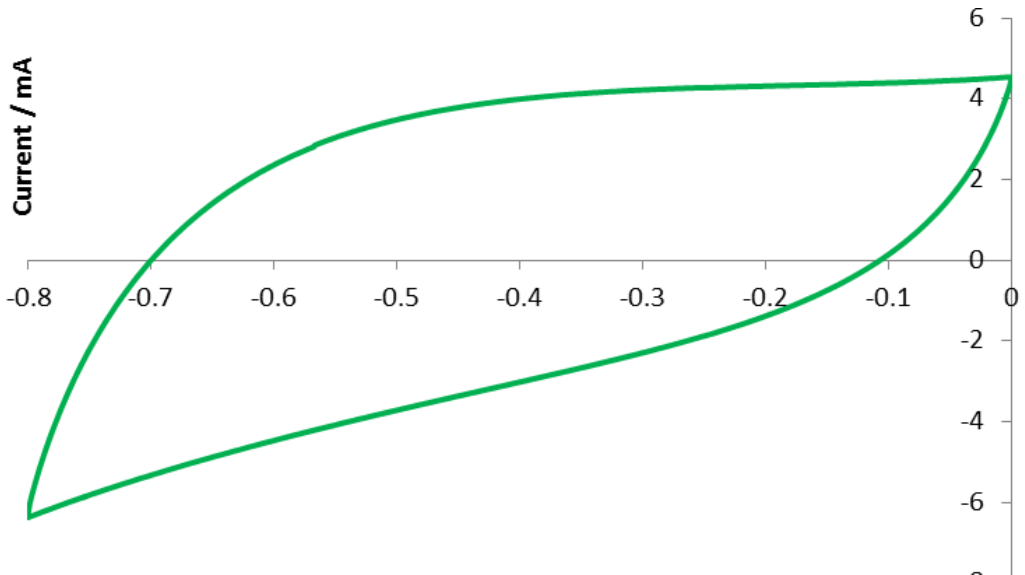

Figure 63: A cyclovoltamagram of an 'as prepared' TiN electrode at 1000 mV s^{-1} in 1M $KOH_{(aq)}$ vs Hg/HgO.

The area within the sweep shows that more current was passed in the negative (oxidative) half of the sweep, suggesting that a reductive process was occurring.

The overall change in the amount of charge stored by the electrode over the 90 cycles used in this experiment was an increase of 68%. This supports the theory that an oxidised surface over a conductive support will increase the capacitance.

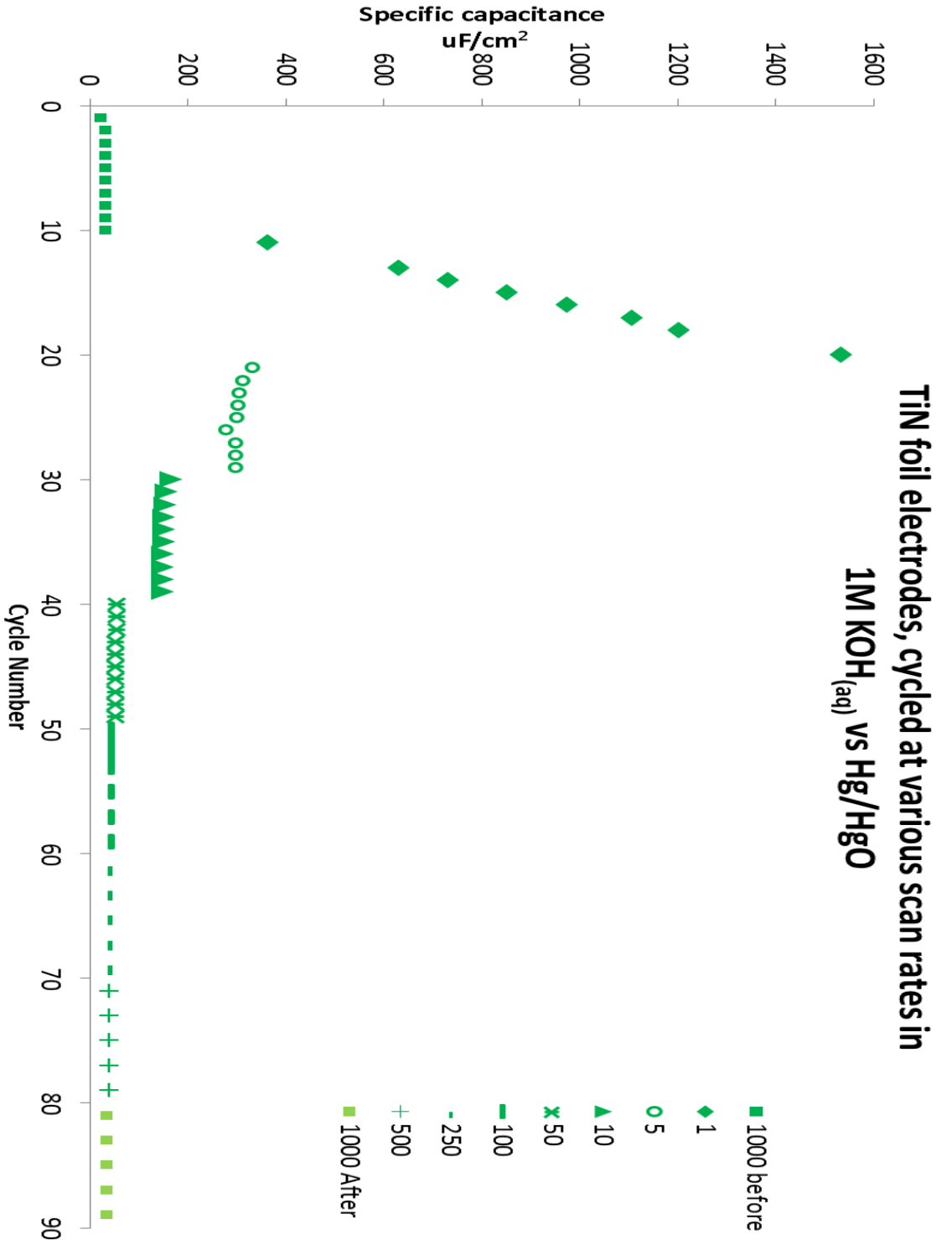

Figure 64: A graph of the specific capacitance of as prepared TiN, cycled in 1M $KOH_{(aq)}$ vs Hg/HgO.

The scan rates in (mV s^{-1}) for each group of cycles are shown in the key.

Of note are the general trends of the first two series, the first shows a drastic increase in specific capacitance as the series progresses, which is reversed as the scan rate increases. This is discussed above.

5.6.1.2 Potential step oxidised.

A similar trend is observed on the potential step oxidised samples, with the first series showing a rise in the specific capacitance of the surface but not such a large increase as the 'as prepared' surface (+ 0.8 %, Figure 66). This supports the theory that an electrochemically active surface species is reacting and generating charge before being consumed, as this species would be consumed during the potential step oxidation of the electrode surface.

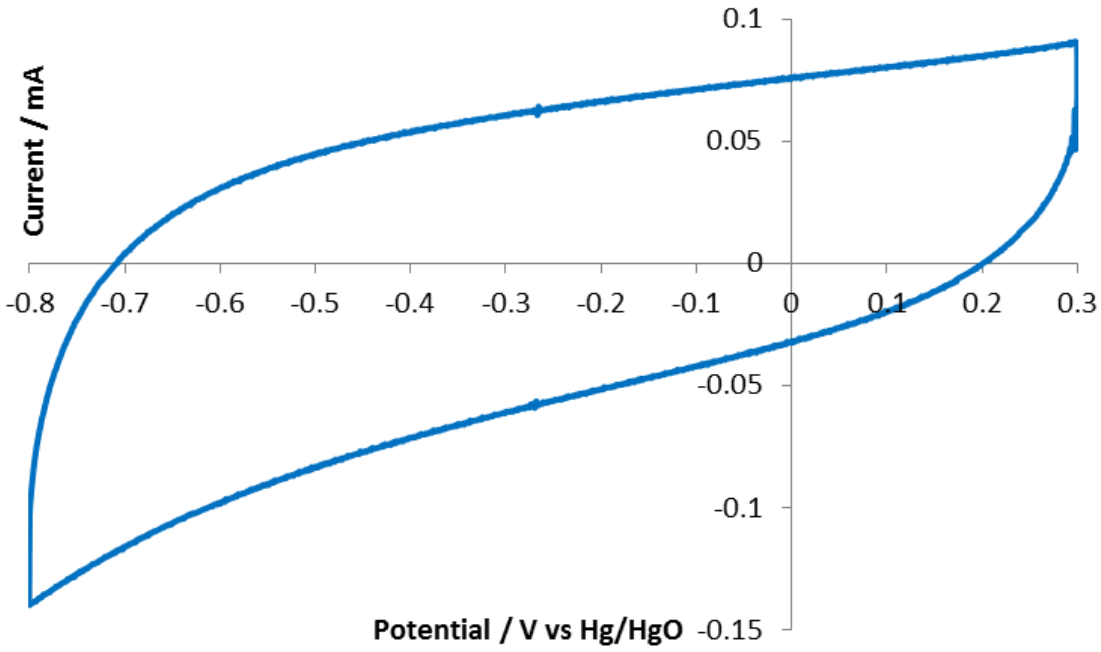

Figure 65: Cyclic voltammetry of a potential step oxidised TiN surface at 500 mV s^{-1}.

The specific capacitance values for this electrode were much lower than that found for the 'as prepared' surface. This could be due to a comparatively thick surface layer of fully oxidised species being formed across the surface during the treatment which restricts the supply of electrons to the surface/electrolyte interface, reducing the amount of charge the surface is able to balance and so reducing the specific capacitance.

The overall change in the specific capacitance during this experiment was an increase of 0.4%.

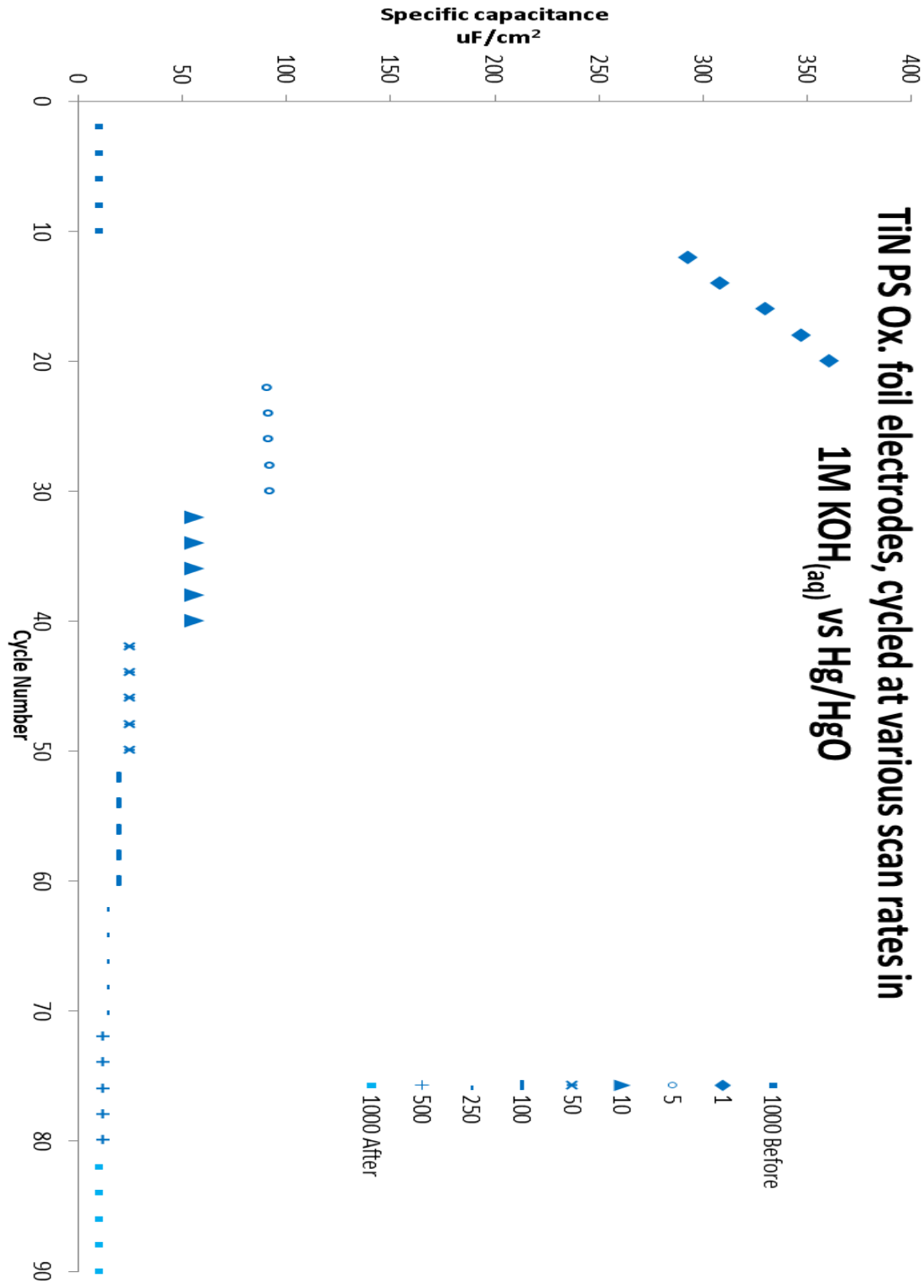

Figure 66: A graph showing the specific capacitance of the potential step oxidised TiN surface at various scan rates.

A similar trend to that observed in the 'as prepared' sample (Figure 64) in that the specific capacitance increases over the 1 mV s^{-1} scans and decreases thereafter. However, this effect is not as pronounced.

5.6.1.3 CV oxidised.

The cyclic voltammetry oxidised (CV) sample shows a specific capacitance increase in the first three sets of cycling (Figure 67). This supports the idea of a non-reversible reaction occurring at the surface of the electrode on cycling. The increasing trend in capacitance is observed over a larger number of cycles compared to the PS oxidised sample. This arises as the CV oxidised sample will have spent a shorter period of time above the potential required to generate this species, so logically will have less of this species present at its surface.

As stated the slowest scan rates of the CV TiN electrode showed an increasing trend in the specific capacitance, again not so large an increase as the 'as prepared' sample, showing an increase of +146 % at 1 mV s^{-1} and +5 % at 5 mV s^{-1}. The 10 mV s^{-1} scans show a negligible increase in the specific capacitance (0.006%), suggesting that the material causing this increase has been consumed by this point.

Over the course of the experiment, totalling 90 cycles, the CV sample showed a 9% drop in the amount of charge it was able to store.

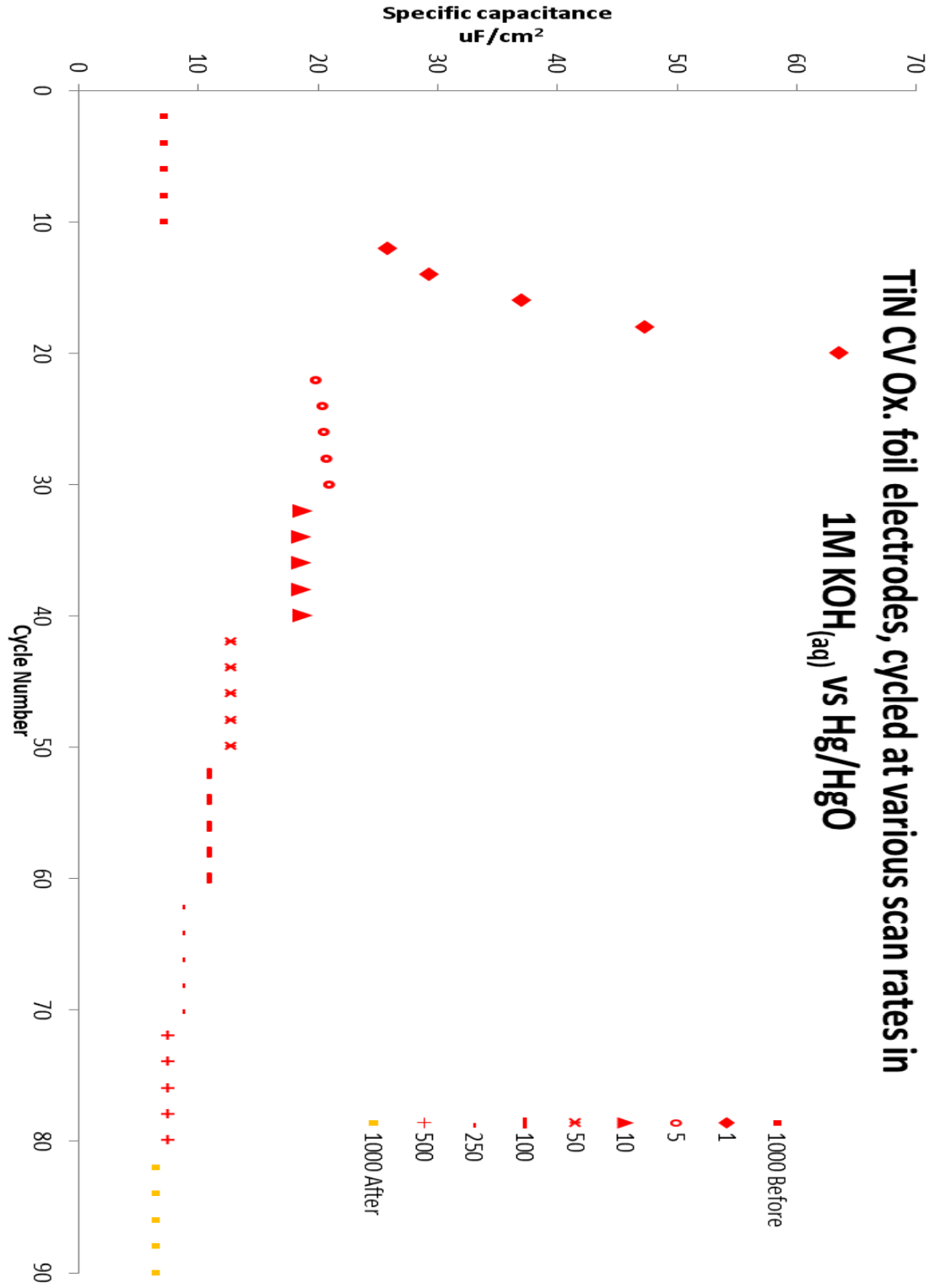

Figure 67: A graph showing the specific capacitance of the cyclically oxidised TiN surface at various scan rates.

A similar trend to that observed in the 'as prepared' sample (Figure 64) in that the specific capacitance increases over the slower scan rates and decreases slightly thereafter.

5.6.1.4 Thermally oxidised.

The thermally oxidised surface is the only surface that shows a negative trend in the specific capacitance throughout the slowest scan rate (Figure 69), losing 75 % of its charge storage ability over the ten scans at 1 mV s^{-1} (235 to 59 μF cm^{-2}).

After this point the specific capacitance rises slightly until the 250 mV s^{-1} scans before dropping again. Over the course of the experiment, the electrode was able to store 12 % more charge. The increase in charge storage on cycling in KOH, above that exhibited by the original thermally oxidised surface, suggests that a hydrated oxide layer produced electrochemically is better able to store charge under the conditions employed. This could be because the TiO_2 species produced by electrochemical methods is protonated, whereas thermally generated TiO_2 will be more or less aprotic. Protons are near impossible to observe by XPS owing to their being only a single electron associated with the atom and only a single emission observable. Their presence has to be inferred from the subtle effects that they have on other species.

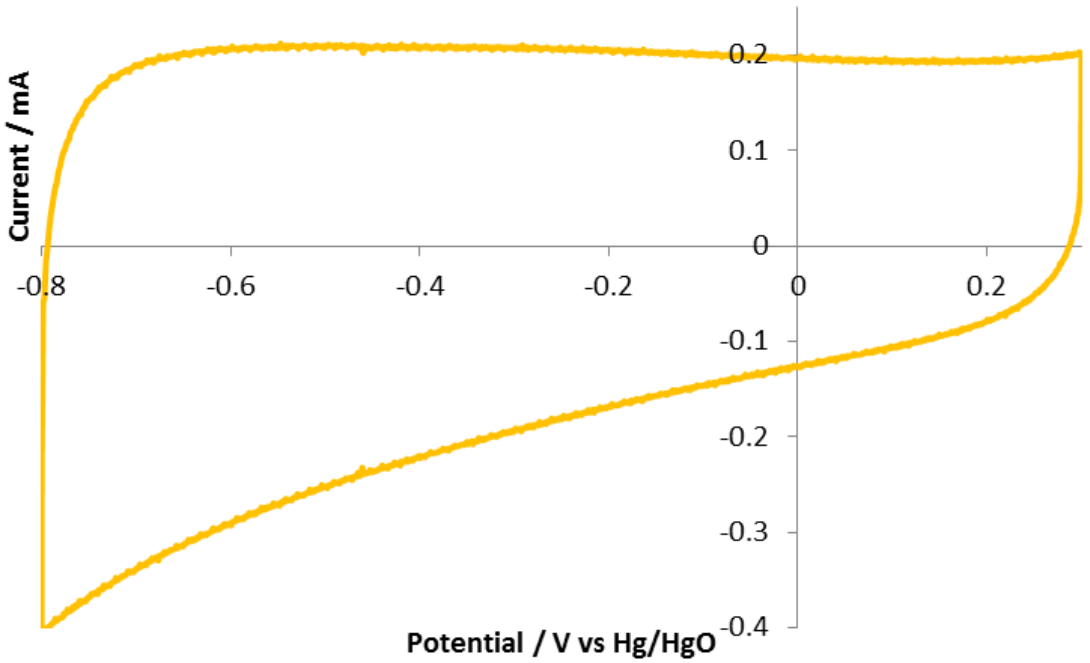

Figure 68: A cyclic voltammogram of a thermally oxidised TiN electrode at 500mV s^{-1}.

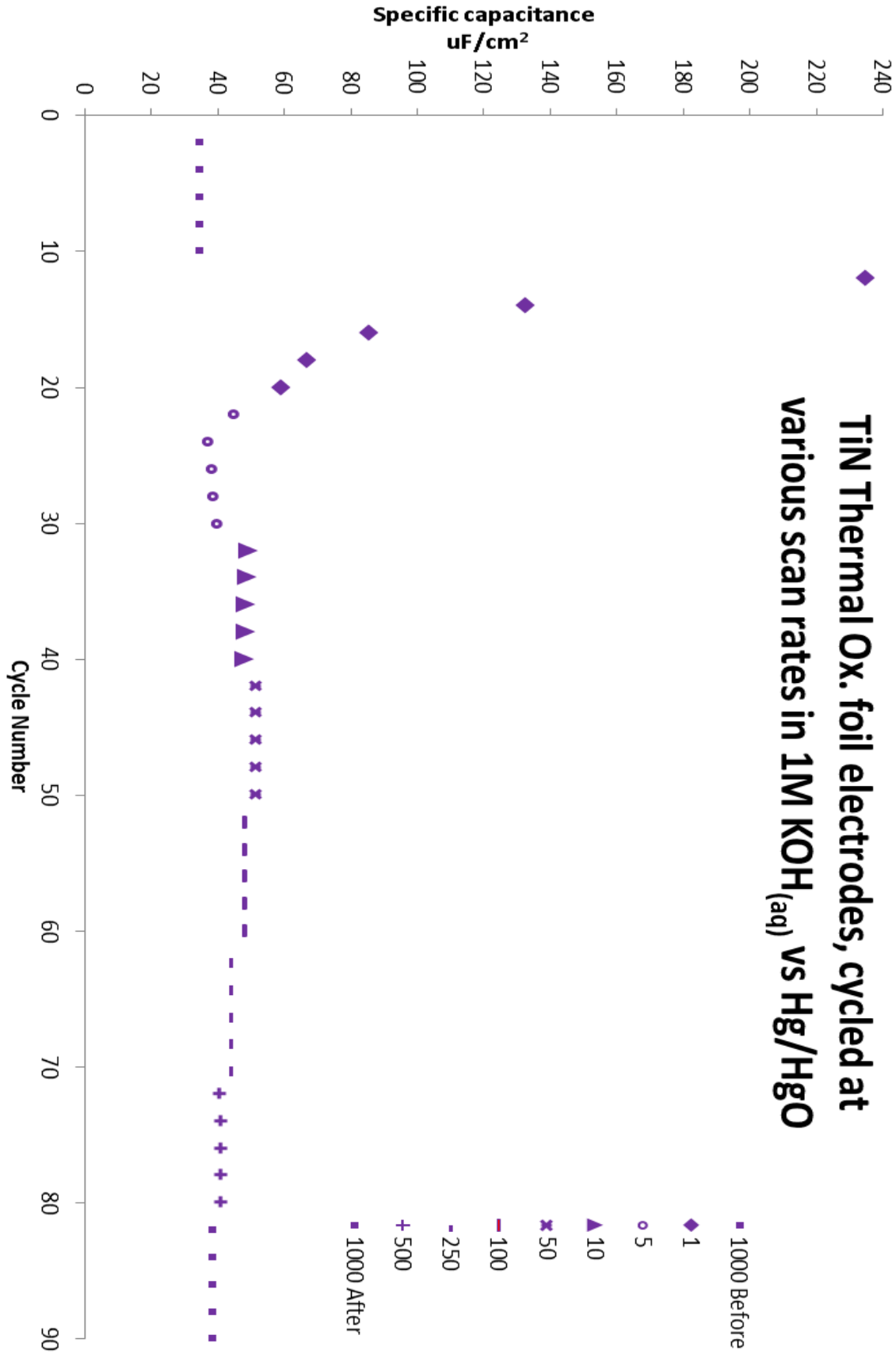

Figure 69: A graph showing the specific capacitance of the thermally oxidised TiN surface at various scan rates.

5.6.2 VN.

Aqueous cycling of VN (Figure 70 and

Table 7) shows that the 'as prepared' surface has the highest specific capacitance, followed by the cyclically oxidised, thermally oxidised potential step oxidised. This suggests that it is predominantly a surface roughness effect, rather than the chemical environment at the surface, which is dominating the capacitance of the surfaces as, with the exception of a very small amount of V^{v} species on the CV surface, the two electrochemically oxidised surfaces are practically identical. A study by Kumta with VN powders[42] cycling in 1M $KOH_{(aq)}$ has shown that VN can achieve capacitances of 1340 μF g^{-1} (3.45 μF cm^{-2}) at 2 mV s^{-1}. In this study, the VN particles are observed as having their surface oxide layer stripped as the material is cycled, with vanadium containing species being detected in the electrolyte at hundreds of ppm levels post cycling. In addition, XPS and IR exhibits a change on the surface of the cycled VN powder in that an oxide layer is grown on the surface during cycling. As this layer grows, it becomes more stable to the electrolyte, stabilising the specific capacitance value of the surface.

On cycling the VN electrodes showed little visual change with the exception of the thermally oxidised samples. This will be further discussed in 5.6.2.4.

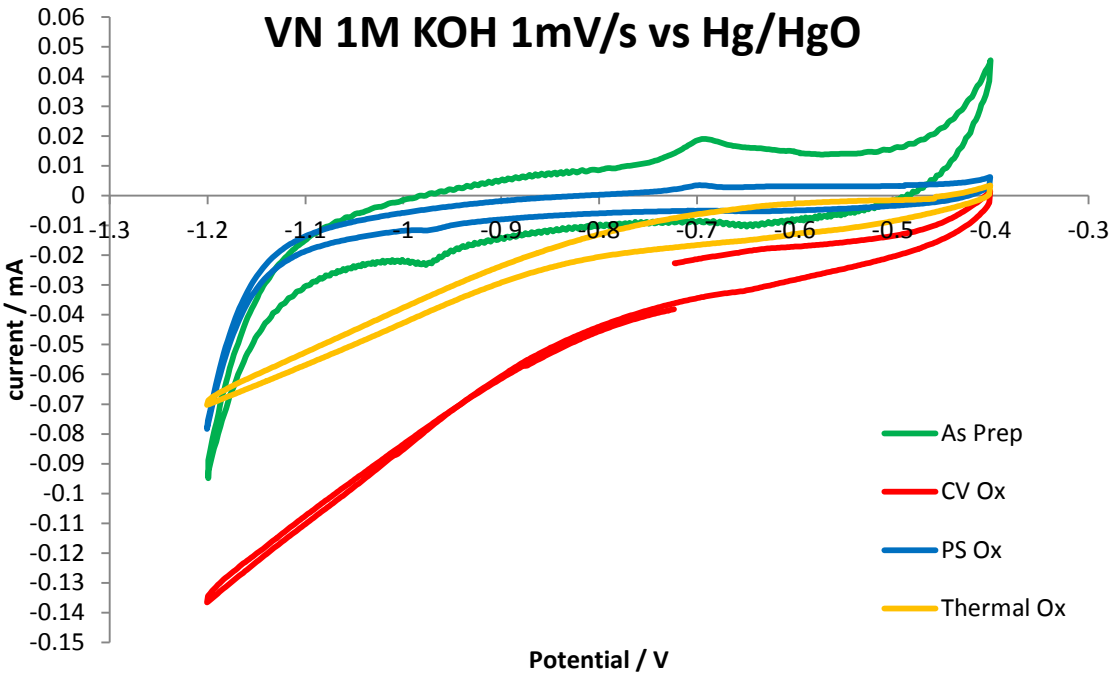

Figure 70: Cyclic voltammetry performed on VN electrodes oxidised by various methods in 1M KOH at 1mV s^{-1} vs Hg/HgO reference electrode.

The 'as prepared' VN (green line) displayed the highest capacitance. The cyclically oxidised electrode (red line) showed the lowest capacitance. Thermally oxidised (yellow line) and potential step oxidised VN (blue line) have capacitances between these. The sweeps shown are from the 3rd cycle of 10 at 1 mV s^{-1} for each system.

The majority of the current passed by the CV Ox, PS Ox and Thermal Ox electrodes is cathodic (Figure 70), suggesting that the electrode is drawing current from the circuit and either reducing the electrolyte solvent (in this case water) or being irreversibly reduced by some process. This could be the reduction of the V^{V} and V^{IV} species at the surface towards a predominantly VN like or V^{III}. The XPS supports this, showing that prior to cycling the surfaces of the electrodes were rich in V^{IV} and V^{V} environments.

5.6.2.1 As prepared.

The 'as prepared' VN sample showed an electrochemical response that was typical for materials behaving like a double layer capacitor; no redox peaks were discernible on the scans at any scan rate. The observed response is asymmetric in a similar manner to those seen for the TiN but in reverse, the oxidative (potential moving to more negative voltages) half of the cycle is

systematically larger than the opposite half of the spectrum. Owing to an IR drop present in the data, the magnitude of this asymmetry is uncertain, but it is only very slightly larger.

The highest specific capacitance observed for the 'as prepared' VN was at 50.97 μF cm^{-2} at 1 mV s^{-1} (Figure 71). This is a large difference compared to the value reported by Kumta[42] of 554 μF g^{-1} at 2 mV s^{-2}. Converting from F g^{-1} to F cm^{-2} the specific capacitance observed is significantly larger at 3.45 μF cm^{-2}.

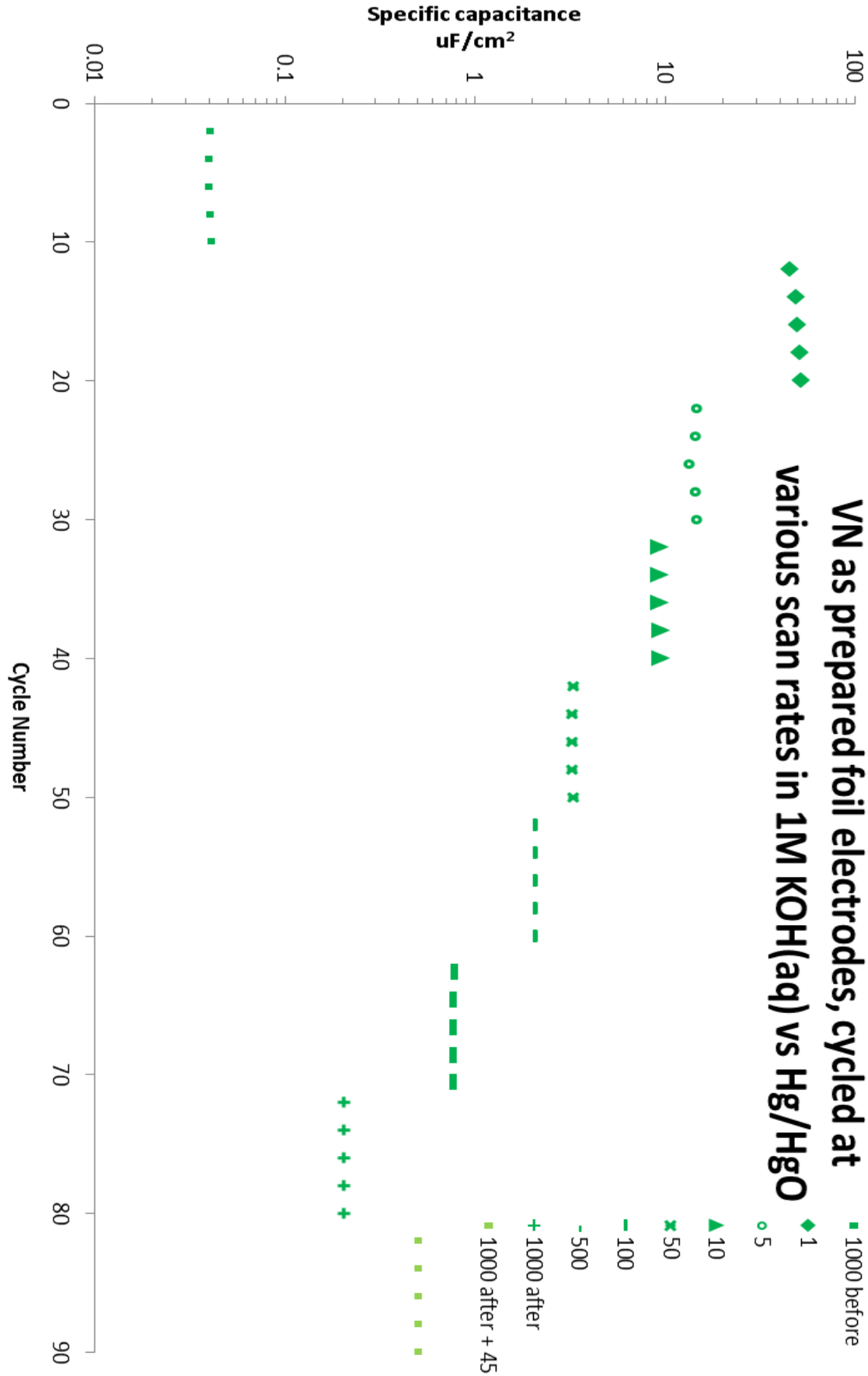

Figure 71: The specific capacitances of the as prepared VN surface.

5.6.2.2 Potential step oxidised.

Unfortunately the data for the PS oxidised VN is incomplete due to problems during its collection. Of the four VN surfaces tested, potential step oxidised VN shows the lowest specific capacitance at all scan rates where the data is available (Figure 72).

One possible reason for the lowered capacitance is the densely formed layer of VO_x species present on the surface of these electrodes. This layer will have lower conductivity compared to VN, so could be dramatically reducing the capacitance of the electrode surface.

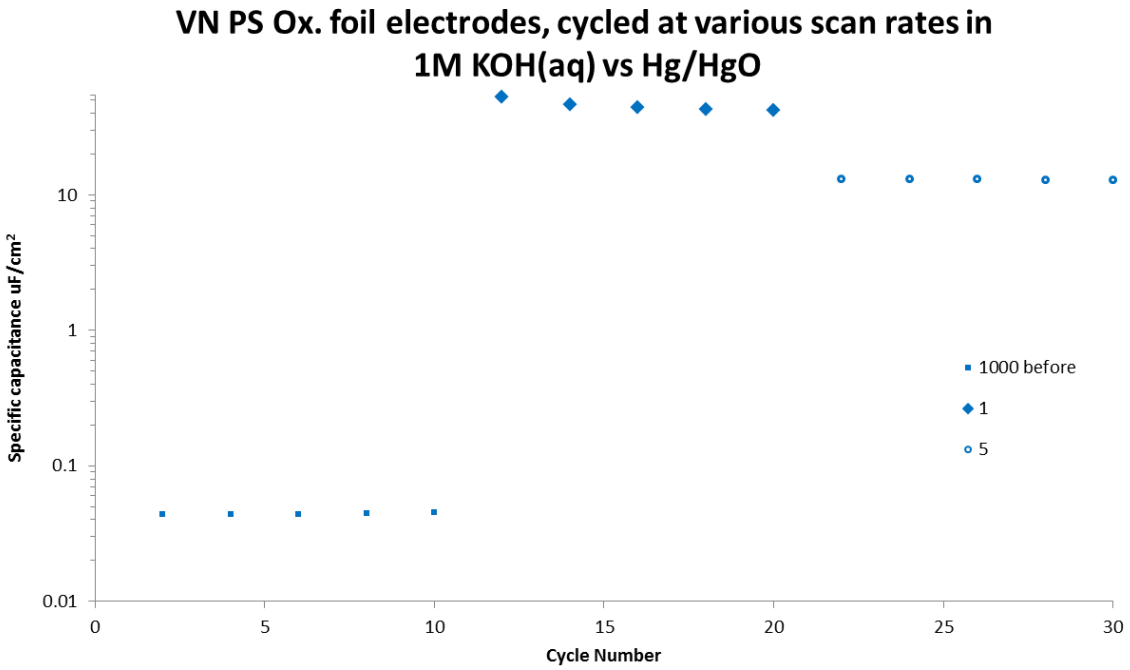

Figure 72: The specific capacitance of potential step oxidised VN at various scan rates.

5.6.2.3 Cyclically oxidised.

The initial 1 V s^{-1} series shows a large (92 %) drop in capacity over the course of the series, with the majority of this loss observed between cycles six and eight.

The highest observed specific capacitance for cyclically oxidised VN was 72.5 µF cm^{-2} (Figure 73). This was observed during the first 1 mV s^{-1} scan. During this series, there is a noticeable decreasing trend in the observed specific capacitances. After this series, the specific capacitances become more stable,

dropping with scan rate. This surface shows an increasing trend with cycling, displaying a 1.9 % increase between the first of the 100 cycles and the 45th.

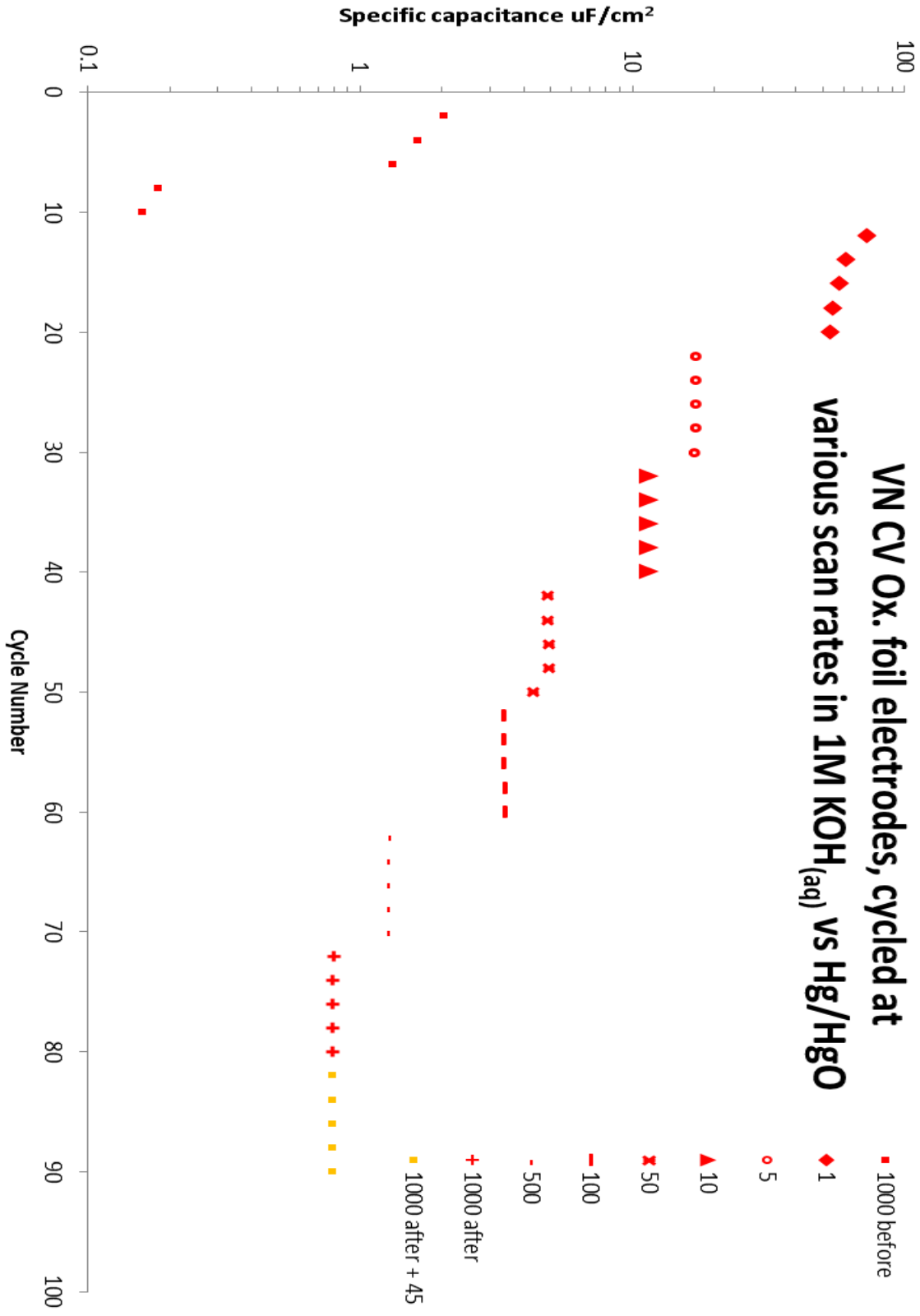

Figure 73: The specific capacitances of cyclically oxidised VN at various scan rates.

5.6.2.4 Thermally oxidised.

The thermally oxidised sample displays behaviour, in terms of its specific capacitance, atypical of the rest of the VN samples (Figure 75). A large increase is observed during the 50 mV s^{-1} scans showing a 3 to 137 µF cm^{-2} jump and the reasons for this are unclear. One possible explanation is that the thermal treatment generated a very slightly soluble, in 1M $KOH_{(aq)}$, layer that dissolved from the surface of the electrode during the cycling to reveal a much more electroactive species with a much higher specific capacitance. This can be seen during the middle of the 50 mV s^{-1} scans (Figure 74).

A possible explanation for this jump in capacity could be that the non-conductive VO_x species formed on the electrode surface had dissolved into the electrolyte in the six hours the electrode had spent submerged in the electrolyte before these cycles were collected. This is supported in the literature.[42]

The surface was less stable than expected, exhibiting a 4.8 % drop in specific capacity over the extended cycling. The faint purple patina visible on the thermally oxidised electrodes surfaces appeared to be removed on cycling, leaving a similar appearance to the other VN electrodes. This change could be because the patina dissolved into the electrolyte

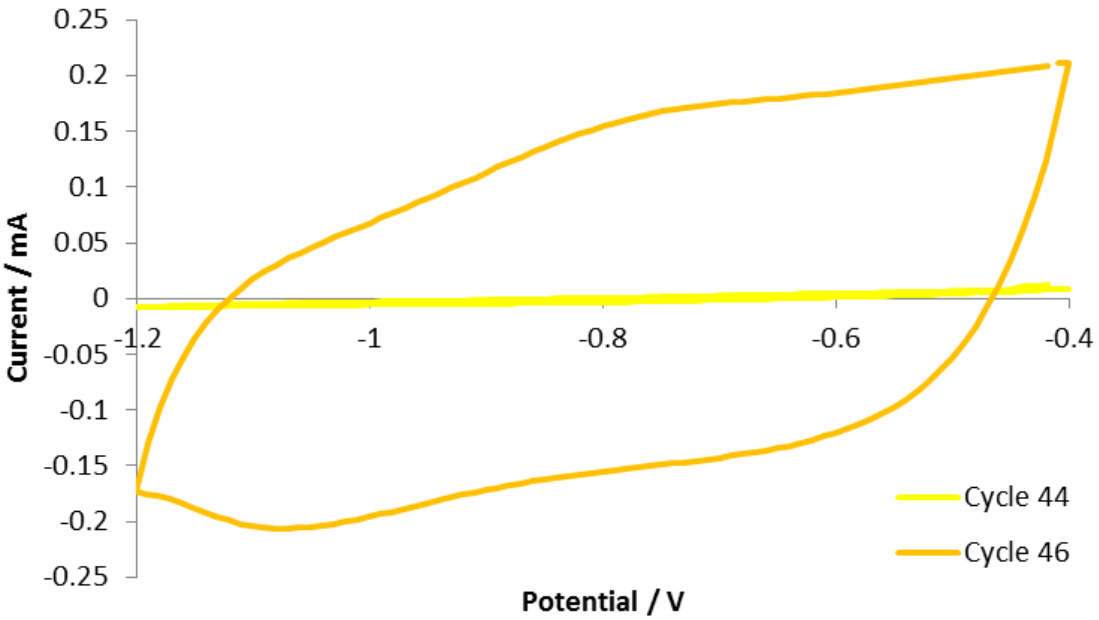

Figure 74: Cyclic voltammetry showing cycles 44 and 46 from the thermally oxidised VN testing. A massive increase in the current passed between the two cycles can quite clearly be seen.

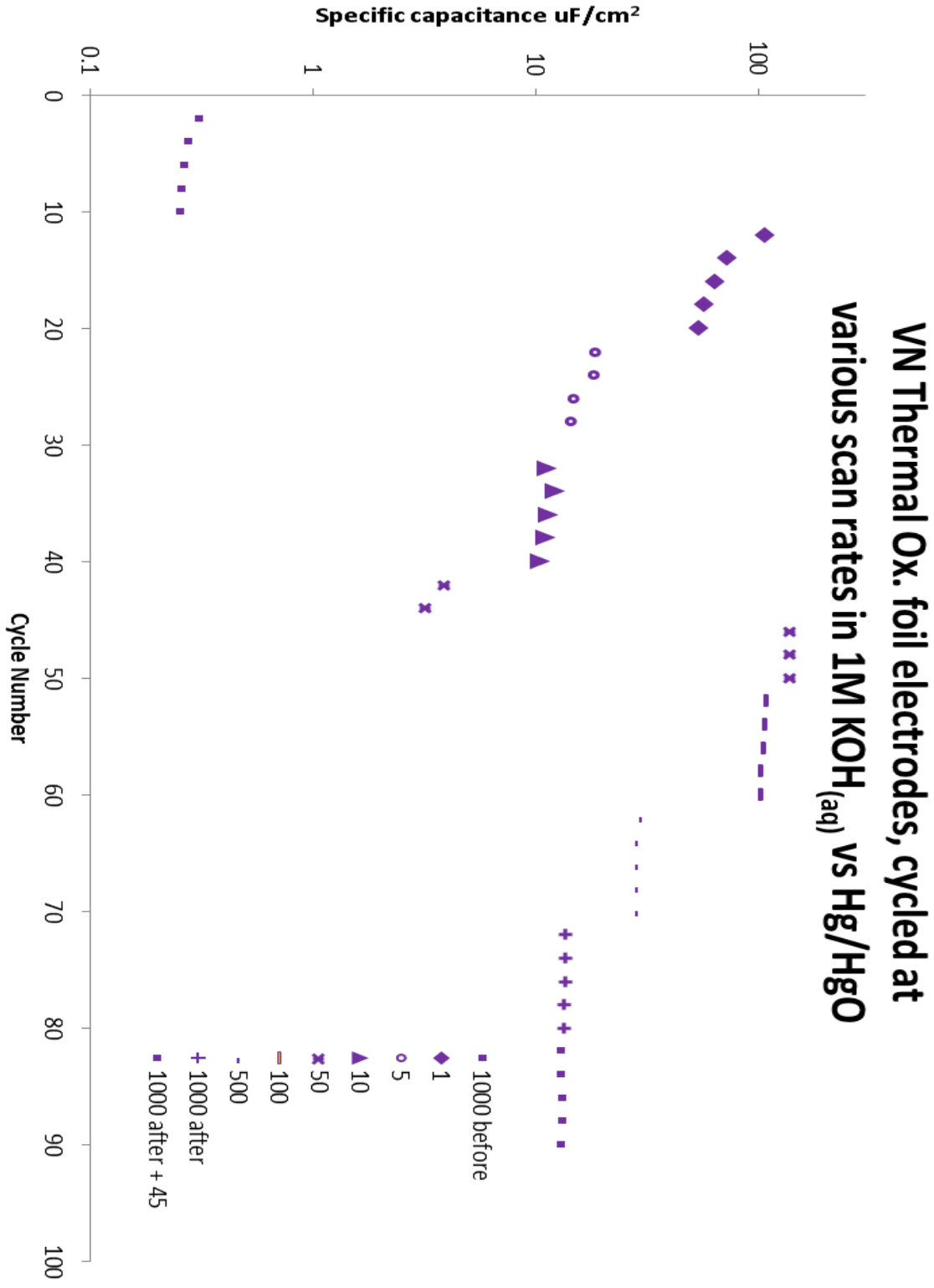

Figure 75: The specific capacitances of thermally oxidised VN at various scan rates.

5.7 Conclusions and further work.

RuO_2 used in a supercapacitors[118] has been demonstrated with specific capacitances of 7750 μF cm^{-2} using thin films of RuO_2 in an acidic electrolyte. This value is higher than has been demonstrated from metal nitrides in this work. Studies on VN by others[42] on powdered samples achieved a value of 3.5 μF cm^{-2} and work with powdered TiN[39] shows a highest capacity of 184.9 μF cm^{-2}. Both of these values (in μF cm^{-2}) are from scans conducted at slow scan rates where the nitride material has been suspended into a conductive matrix ('Super P' and PVDF). The observed capacities for the foil electrodes reported in this chapter, compared to these published results, support the idea that having a complete conduction pathway between the current collector and the electro active surface region is important for optimising the capacitance.

The largest specific capacitance of 1546 μF cm^{-2} was observed in the 'as prepared' TiN sample. This was not a stable specific capacitance and decreased on every subsequent scan on that sample. This is a comparable value to those observed per cm^2 of hydrated RuO_2.[125] This demonstrates that with the correct tuning, nitride materials could provide suitable power levels for commercial application. This 'tuning' would need to first identify, then stabilise, the transitory species or process responsible for the observed 423 % capacity increase at slow cycling rates. If this process is irreversible then this may not be possible. A further issue with TiN and VN is that these high specific capacitances are only observed at low scan rates. This would make TiN and VN less useful for automotive and portable electronic applications, where a faster cycling rate would be required. They may still be of interest to load levelling applications, either, on a domestic scale or a regional one.

The fast scan rates with TiN electrodes showed that the surface was stable to cycling with specific capacities ranging from 53 μF cm^{-2} at 50 mV s^{-1} to 33 μF cm^{-2} at 1000 mV s^{-1}. The values for the specific capacities are very difficult to compare at higher scan rates as they are not usually quoted in the literature. These specific capacitances were all ± 2% of each other at their respective scan rates, with this deviation growing smaller as the scan rate dropped and the exposure time to the electrolyte increased. The smallest deviation was 0.41%. This suggests that, after passivation, a surface that is stable to cycling in terms of charge storage is produced.

The most stable TiN surface was the potential step oxidised sample, showing a minor increase (+ 0.4 %) in the specific capacitance of the surface between the first 1 V s^{-1} set and the last. The greatest deviation was, again, on the slowest scan rate (1 mV s^{-1}) but was comparably small at a 23% increase. At faster scan rates, this capacity variance drops to less than ± 0.45 % at all scan rates from 5 mV s^{-1} back up to 1000 mV s^{-1}.

VN is not as promising a material as was once thought, as suggested by a number of papers in recent years.[126-128] However, the best way to treat it post synthesis to improve its capacity is to thermally oxidise the surface of the material post synthesis before cycling it over its stable range in 1M $KOH_{(aq)}$ slowly for 2-3 hours. A major issue with using VN is its relatively rapid, when compared to TiN, loss of performance (1.5% vs 0.5 %).

The procedure for generating the electrochemically oxidised foils requires further refinement as the similarity observed between the CV and PS oxidised samples suggests that the potentials used for the oxidation electrochemical treatments were too harsh for the intended purpose. The potential should have been lowered slightly in order to give the desired result.

A possible approach to this question might be to grow a range of TiO_x layers onto TiN surfaces utilising controlled potential step oxidation. Then characterise these layers and evaluate their specific capacitances. Providing the speciation of the grown layers can be adequately controlled to give a suitable range of surface environments, both in terms of TiO_2 and Ti(O,N) speciation, it could be possible to derive a satisfactory answer to resolve this issue.

A further issue with the analysis of the surface, was the need for etching to produce as close as possible to an 'oxide free' surface, required to produce an effective model for the TiN environments. An ideal method to overcome this would require a TiN sample to be produced, which completely avoids contact with an oxygenated environment prior to data collection. This is possible but would require a suitable glove box to be set up with access to the entry airlock for the XPS spectrometer.

Similar to the effect on the TiN surfaces, the VN showed the highest specific capacitance increase on a thermally oxidised surface, showing a 2494 %

increase at high scan rates over 125 cycles. . This supports the theory that combining Ti and V nitrides may provide a stable, high capacity surface. Areas for further investigation are what proportion of Ti and V should be present and how this mixed binary nitride should be treated, post synthesis, to give to highest specific capacity.

Chapter 6: Conclusions and further work.

V^{IV} amides are more sensitive that their corresponding Ti^{IV} amides and require considerable care to synthesise. They undergo similar sol gel reactions to those established for the corresponding Ti amide. Nitride solid solutions formed from the ammonolysis of various stoichiometry's of these metal amides showed that the highest capacity was observed for a similarly prepared sample of VN. At fast scan rates the highest specific capacity of the solid solutions was observed from a sample of $V_{0.4}Ti_{0.6}N$, at slower scan rates $V_{0.8}Ti_{0.8}N$ gave the highest specific capacity.

TiN inverse opals showed a high specific capacity on cycling. Other materials in this morphology should be tested to see if a similar improvement in specific capacitance is observed when compared to powdered morphologies.

To expand upon the work in this study, the continued assessment of the suitability of TMN materials towards supercapacitor applications should be undertaken. Whilst this work has covered a small area in detail, there is further potential for studies involving metal nitrides still to explore and consider with this application in mind. When the correct metal nitride to investigate has been identified, the correct morphology, surface treatment regimen (if required) and production methodology will need to be established in order to make this class of materials into an industrially viable alternative to Ru oxides. With respect to the surface treatment, initial assessment conducted here suggests that a surface oxide generated by thermal means can provide large increases in specific capacitance. Whilst some aspects of this would be best passed onto those in related fields, for example, chemical engineering for the production methodology and scaling up the process from laboratory to production plant size, a large amount of investigative work needs to be done by chemists first. Areas of investigation should include the exact temperature and duration of heating for the surface oxide layer to be produced under, and which specific species or combination of species produces the largest percentage increase in the specific capacity. In theory, the surface species present can be tuned by adjusting the conditions employed; the temperature, the duration and the atmosphere used will all have an impact on the surface environment and species grown by these processes.

An assessment should be made of the TMN materials for potential as Li cell electrode applications. The basic rocksalt structure exhibited by a range of early transition metal nitrides is not well suited to the intercalation chemistry employed by many current battery materials for charge storage with Li, for example $LiCoO_2$. The metal oxides generated on the surface of the TMN substrate in this work demonstrate a remarkable increase in the Li charge storage potential of the TMNs. This requires further study as a new class of Li charge storage materials may be discovered.

An investigation could be made into the feasibility of templating mixed metal binary nitrides, like the (Ti,V)N materials prepared, into polymeric templates. This should be feasible as both the VN and TiN precursor sols behave similarly, reacting in a similar time frame and to similar degrees. If a mixed binary nitride of (Ti,V)N proves to be the most electrochemically efficient and a derivation of the inverse opal structure provides the highest energy density for the device, then knowledge as to whether the composition of the nitride produced varies as a result of infiltration will be vital in producing components that will perform as advertised.

There is potential for the investigation of alloying Ti with other metals to form a wider range of mixed binary nitrides for supercapacitor and other electrochemical applications. Whilst TiVN has been studied in this project, and CrTiN has been reported in the literature,[74] Mn might be interesting due to its wide range of redox environments. This, or combination with other metals, may lead to a synergistic effect, enhancing the performance of the material for electrochemical or catalytic applications.

It is possible to template a range of MN compounds into inverse opal morphologies, with the major limitation on the long range order of the structures produced being the quality of the template providing the correct heating and cooling regimen is employed. The ideal ratio of primary amine to metal amide for this infiltration process is a minor excess of half the number of amide groups around the metal centre. The specific capacitance of nitride materials in an inverse opal morphology is very high. An interesting expansion to the synthesis of the template opals would be to improve their structural integrity even further on heating. This could be achieved by the addition of functional groups to enable ‘click’ chemistry to the exterior of the beads.[129]

Post synthesis, the beads are exposed to the correct photowave length for the functional groups to react, bonding the beads together chemically. This would allow the beads to survive higher temperatures during ammonolysis, theoretically increasing the level of sintering that templates around them.

Whilst the method employed to synthesise and infiltrate the sols and templates is acceptable on a laboratory scale with one exceedingly dedicated individual, for this to become an industrially viable process a great deal of very careful consideration would need to be undertaken to scale up the process suitably, and to make it more economical. The preparation of these compounds is possible on an industrial scale, SAFC Hitech list $Ti(NMe_2)_4$ and a small range of other metal amides in their products catalogue.[130] However, I expect that this is manufactured on a scaled up version of the laboratory procedure, which is effectively a batch process. In order to make these compounds most economically a flow type process would be desirable, where the variety of temperatures and pressures required are contained in individual vessels and the reaction solution is transferred from vessel to vessel. This transferring process could be simply moving the solution from flask to flask or a part of the procedure, such as a filtration of a solid LiCl by-product from the dissolved amide. The real challenge for a more industrially applicable process is the infiltration of the templates. Whilst I am sure this is feasible, it is beyond my limited engineering knowledge as to how this would be possible for a non-air sensitive sol, a process that would be severely complicated by the reactivity of the amide sol. Production of the $V(NMe_2)_4$ starting material should be refined in order to make the process more economical in terms of reagents and yield. Whilst the procedure detailed here works to produce the desired amide, it is inefficient as indicated by the yields obtained. Another disadvantage is that it utilises and produces a range of harmful and hazardous compounds, either as the starting materials, the products, by-products or the solvents. In order to make it a more desirable process for industry, the volume of these chemicals being used and the amount of energy needed to remove them would need to be reduced to the absolute minimum. This can be achieved by studying the preparative procedure for the metal amide in greater depth and fine tuning the reaction conditions towards using a minimal amount of solvent to give the highest yield. One possible alteration might be to omit the filtration step for the removal of LiCl altogether and sublime the $V(NMe_2)_4$ straight from the

reaction solution after reducing its volume. This would remove a process where a large amount of surface absorption may occur. From personal experience, it is possible to increase the yields from the reactions simply by increasing the scale on which the amide is synthesised, presumably because a passivation reaction occurs between the reaction solution and the reaction vessels. At a larger scale, larger glassware is used, which will, have a lower internal surface area to volume ratio. This will mean that the fraction of the reactive species in the reaction consumed by the passivation will be lower, thus increasing the yield. Larger yields and improving the atomic efficiency of the process for synthesising metal amides is clearly desirable.

Other applications for inverse opal nitrides should also be investigated. The structures inherent open-ness leading to an inherent ability to facilitate diffusion should prove beneficial to supported solids for gas and liquid phase catalysis. The chemical resistance of a range of nitride materials could prove useful for the production of more aggressive compounds.[131] The ability to incorporate low loadings of other metal centres into these structures, may be extremely beneficial for catalytic purposes. Owing to the difficulty of making the inverse opal structures, initial investigations should be conducted on powders, before an optimised material composition is templated and assessed.

VN has the potential to be a suitable more economical counterpart to the Ru-oxides currently employed for commercial supercapacitor applications. The expense, both in monetary and environmental terms, of producing VN vs RuO_2 is much lower, even with the extra precautions employment of the inert atmosphere techniques required as a result of the hazardous nature of many of the starting materials in this project.

An oxidised film produced on the surface by thermal oxidation of a TiN electrode surface provided a specific capacitance increase of 13 % as did a surface oxidised layer produced by potential step oxidation of VN. This suggests that modification of the surface by oxidation can provide significant enhancements to a devices capacity.

The electro-deposition of -$[M(NR)_x]$- materials into a template should also be explored. This would require the design and production of a suitable cell to make an -$[M(NR)_x]$- sol in, and to generate ammonia/a primary amine at a controlled rate in a non-aqueous environment. It would require a conductive

substrate to be used. Whilst these are not inconsiderable obstacles to overcome, it should be possible to achieve. This could be used to create a core-shell structure of a TiN substrate with a VN, or other nitride of interest, shell deposited over this conductive core. In addition to this, a further area of research should be towards the electrodeposition of a very thin, defect free layer of a suitable electroactive species onto a MN framework. The methods employed in this project to generate a thin layer of oxide species at the surface are simple in nature and offer very limited control of the variety and uniformity of the surface oxide layer generated. Electrodeposition offers considerable control over the species deposited by the fine tuning of the deposition solution and conditions and the depth to which the surface is covered by monitoring the amount of current to or from the deposition surface. This could be combined with the prior suggestion to electrodeposit both the nitride support, followed by the oxide redox active surface layer. This has been shown to be possible with Li-ion conductive polymer membranes over a carbon foam[132] and so tweaking the procedure used for this could produce some very interesting results.

References.

1. J. R. Miller and A. F. Burke, *Interface*, 2008, **17**, 53.
2. D. Pletcher, *First course in electrode processes*, RSC publishing, 2009.
3. X. Zhao, B. M. Sanchez, P. J. Dobson and P. S. Grant, *Nanoscale*, 2011, **3**, 839-855.
4. C. Arbizzani, M. Mastragostino and F. Soavi, *Journal of Power Sources*, 2001, **100**, 164-170.
5. A. Jaafar, B. Sareni, X. Roboam and M. Thiounn-Guermeur, in *Vehicle Power and Propulsion Conference (VPPC), 2010 IEEE*, 2010, pp. 1-6.
6. M. Wohlfahrt-Mehrens, J. Schenk, P. M. Wilde, E. Abdelmula, P. Axmann and J. Garche, *Journal of Power Sources*, 2002, **105**, 182-188.
7. H. H. H and L. G. R, Google Patents, 1959.
8. W. Sugimoto, H. Iwata, Y. Yasunaga, Y. Murakami and Y. Takasu, *Angewandte Chemie International Edition*, 2003, **42**, 4092-4096.
9. W.-C. Fang, O. Chyan, C.-L. Sun, C.-T. Wu, C.-P. Chen, K.-H. Chen, L.-C. Chen and J.-H. Huang, *Electrochemistry Communications*, 2007, **9**, 239-244.
10. C.-C. Hu, K.-H. Chang, M.-C. Lin and Y.-T. Wu, *Nano Letters*, 2006, **6**, 2690-2695.
11. Y. Liu, W. Zhao and X. Zhang, *Electrochim. Acta*, 2008, **53**, 3296-3304.
12. H. Chen, X. Dong, J. Shi, J. Zhao, Z. Hua, J. Gao, M. Ruan and D. Yan, *Journal of Materials Chemistry*, 2007, **17**, 855-860.
13. F. A. Cotton, G. Wilkinson, C. A. Murillo, M. Bochmann and R. Grimes, *Advanced inorganic chemistry*, Wiley New York, 1999.
14. V. Khomenko, E. Frackowiak and F. Béguin, *Electrochim. Acta*, 2005, **50**, 2499-2506.
15. M. Jayalakshmi, N. Venugopal, K. P. Raja and M. M. Rao, *Journal of Power Sources*, 2006, **158**, 1538-1543.
16. E. M. Sorensen, S. J. Barry, H.-K. Jung, J. M. Rondinelli, J. T. Vaughey and K. R. Poeppelmeier, *Chemistry of Materials*, 2005, **18**, 482-489.
17. T. Kudo, Y. Ikeda, T. Watanabe, M. Hibino, M. Miyayama, H. Abe and K. Kajita, *Solid State Ionics*, 2002, **152-153**, 833-841.
18. W. Yong-gang and Z. Xiao-gang, *Electrochim. Acta*, 2004, **49**, 1957-1962.
19. L. E. Toth, *Transition Metal Carbides and Nitrides*, Academic Press, New York, 1971.
20. A.-M. Alexander and J. S. J. Hargreaves, *Chemical Society Reviews*, 2010, **39**, 4388-4401.
21. A. L. Hector and W. Levason, *Coordination Chemistry Reviews*, 2013, **257**, 1945.
22. A. Kafizas, C. J. Carmalt and I. P. Parkin, *Coordination Chemistry Reviews*, 2013, **257**, 2073-2119.
23. P. K. Ajikumar, M. Kamruddin, R. Nithya, P. Shankar, S. Dash, A. K. Tyagi and B. Raj, *Scripta Materialia*, 2004, **51**, 361-366.
24. S. J. Clarke, C. W. Michie and M. J. Rosseinsky, *Chemistry of Materials*, 2000, **12**, 863-865.
25. B. M. Gray, S. Hassan, A. L. Hector, A. Kalaji and B. Mazumder, *Chemistry of Materials*, 2009, **21**, 4210-4215.
26. Q. Sun and Z.-W. Fu, *Electrochim. Acta*, 2008, **54**, 403-409.
27. A. M. Glushenkov, D. Hulicova-Jurcakova, D. Llewellyn, G. Q. Lu and Y. Chen, *Chemistry of Materials*, 2009.

28. G.-A. Nazri and G. Pistoia, *Lithium Batteries: Science and Technology*, Springer, 2009.
29. G. Cui, L. Gu, A. Thomas, L. Fu, P. A. van Aken, M. Antonietti and J. Maier, *ChemPhysChem*, 2010, **11**, 3219-3223.
30. B. Das, M. V. Reddy, P. Malar, T. Osipowicz, G. V. Subba Rao and B. V. R. Chowdari, *Solid State Ionics*, 2009, **180**, 1061-1068.
31. Q. Sun and Z.-W. Fu, *Electrochemical and Solid-State Letters*, 2007, **10**, A189-A193.
32. X. Li, M. M. Hasan, A. L. Hector and J. R. Owen, *Journal of Materials Chemistry A*, 2013, **1**, 6441-6445.
33. J. Cabana, L. Monconduit, D. Larcher and M. R. Palacín, *Advanced Materials*, 2010, **22**, E170-E192.
34. Y. Wang, Z.-W. Fu, X.-L. Yue and Q.-Z. Qin, *Journal of The Electrochemical Society*, 2004, **151**, E162-E167.
35. T. P. Ma, *Electron Devices, IEEE Transactions on*, 1998, **45**, 680-690.
36. S. I. U. Shah, A. L. Hector and J. R. Owen, *Journal of Power Sources*, 2014, **266**, 456-463.
37. K.-H. Lee, Y.-W. Lee, A. R. Ko, G. Cao and K.-W. Park, *Journal of the American Ceramic Society*, 2013, **96**, 37-39.
38. C. Chen, D. Zhao, D. Xu and X. Wang, *Materials Chemistry and Physics*, 2006, **95**, 84-88.
39. D. Choi and P. N. Kumta, *Journal of the Electrochemical Society*, 2006, **153**, A2298-A2303.
40. X. Zhou, C. Shang, L. Gu, S. Dong, X. Chen, P. Han, L. Li, J. Yao, Z. Liu, H. Xu, Y. Zhu and G. Cui, *ACS Applied Materials & Interfaces*, 2011, **3**, 3058-3063.
41. S. Dong, X. Chen, L. Gu, X. Zhou, H. Wang, Z. Liu, P. Han, J. Yao, L. Wang, G. Cui and L. Chen, *Materials Research Bulletin*, 2011, **46**, 835-839.
42. D. Choi, G. E. Blomgren and P. N. Kumta, *Advanced Materials*, 2006, **18**, 1178-1182.
43. A. L. Hector, *Chemical Society Reviews*, 2007, **36**, 1745-1753.
44. M. E. Abdelsalam, P. N. Bartlett, J. J. Baumberg, S. Cintra, T. A. Kelf and A. E. Russell, *Electrochemistry Communications*, 2005, **7**, 740-744.
45. A. W. Jackson and A. L. Hector, *Journal of Materials Chemistry*, 2007, **17**, 1016-1022.
46. A. W. Jackson, O. Shebanova, A. L. Hector and P. F. McMillan, *Journal of Solid State Chemistry*, 2006, **179**, 1383-1393.
47. O. Barbieri, M. Hahn, A. Herzog and R. Kötz, *Carbon*, 2005, **43**, 1303-1310.
48. J. H. Moon and S. Yang, *Chemical Reviews*, 2010, **110**, 547-574.
49. I. Zein, D. W. Hutmacher, K. C. Tan and S. H. Teoh, *Biomaterials*, 2002, **23**, 1169-1185.
50. A. Chelnokov, K. Wang, S. Rowson, P. Garoche and J. M. Lourtioz, *Appl. Phys. Lett.*, 2000, **77**, 2943-2945.
51. A. C. Edrington, A. M. Urbas, P. DeRege, C. X. Chen, T. M. Swager, N. Hadjichristidis, M. Xenidou, L. J. Fetters, J. D. Joannopoulos, Y. Fink and E. L. Thomas, *Advanced Materials*, 2001, **13**, 421-425.
52. M. A. McLachlan, N. P. Johnson, R. M. D. L. Rue and D. W. McComb, *Journal of Materials Chemistry*, 2004, **14**, 144-150.
53. M. A. McLachlan, N. P. Johnson, R. M. D. L. Rue and D. W. McComb, *Journal of Materials Chemistry*, 2005, **15**, 369-371.

54. C. Jin, M. A. McLachlan, D. W. McComb, R. M. De La Rue and N. P. Johnson, *Nano Letters*, 2005, **5**, 2646-2650.
55. N. R. Thomson, M. A. McLachlan, C. L. Bower and D. W. McComb, *Langmuir*, 2009, **25**, 11344-11350.
56. A. Rugge, J. S. Becker, R. G. Gordon and S. H. Tolbert, *Nano Letters*, 2003, **3**, 1293-1297.
57. D. Cook, P. N. Bartlett, W. Zhang, W. Levason, G. Reid, J. Ke, W. Su, M. W. George, J. Wilson, D. Smith, K. Mallik, E. Barrett and P. Sazio, *Physical Chemistry Chemical Physics*, 2010, **12**, 11744-11752.
58. J. Hu, M. Abdelsalam, P. Bartlett, R. Cole, Y. Sugawara, J. Baumberg, S. Mahajan and G. Denuault, *Journal of Materials Chemistry*, 2009, **19**, 3855-3858.
59. B. Hatton, L. Mishchenko, S. Davis, K. H. Sandhage and J. Aizenberg, *Proceedings of the National Academy of Sciences*, 2010, **107**, 10354-10359.
60. C. F. Mallinson, B. M. Gray, A. L. Hector, M. A. McLachlan and J. R. Owen, *Inorganic chemistry*, 2013, **52**, 9994-9999.
61. D. C. Bradley and M. H. Gitlitz, *Journal of the Chemical Society A: Inorganic, Physical, Theoretical* 1969, 5.
62. J. Goldstein, D. E. Newbury, P. Echlin, D. C. Joy, A. D. Romig Jr, C. E. Lyman, C. Fiori and E. Lifshin, *Scanning electron microscopy and X-ray microanalysis: a text for biologists, materials scientists, and geologists*, Springer Science & Business Media, 2012.
63. S. Hüfner, Springer, Berlin, 2003.
64. J. C. Fitzmaurice, A. L. Hector and I. P. Parkin, *Journal of the Chemical Society, Dalton Transactions*, 1993, 2435-2438.
65. , International Centre for Diffraction Data, Swarthmore, PA, 2003.
66. L. Hultman, *Vacuum*, 2000, **57**, 1-30.
67. M. Wixom, I. SONG, C. Peiter, J. White and L. Thompson, Electrochemical Society, 1998, pp. 627-638.
68. B. Mazumder and A. L. Hector, *Journal of Materials Chemistry*, 2009, **19**, 4673-4686.
69. N. Iwamoto, Y. Makino and Y. Murakami, *ISPC-B*, 1987, 1166-1171.
70. J. Lau, E. Alain, B. Arkles and A. Paranipe, *Journal of the Electrochemical Society*, 1997, **144**, 1002-1008.
71. S. Tang, S. Gao, S. Wang, J. Wang, Q. Zhu, Y. Chen and X. Li, *Surface and Coatings Technology*, 2014, **258**, 1060-1067.
72. S. J. Henderson and A. L. Hector, *Journal of Solid State Chemistry*, 2006, **179**, 3518-3524.
73. H. Yamamura, M. Yamamoto and K. Kakinuma, *Journal of the Ceramic Society of Japan*, 2005, **113**, 458-461.
74. W. Zhao and F. J. DiSalvo, *Chemical Communications*, 2015, **51**, 4876-4879.
75. U. Schubert and N. Hüsing, *Synthesis of inorganic materials*, John Wiley & Sons, 2012.
76. D. Bradley and E. Torrible, *Canadian Journal of Chemistry*, 1963, **41**, 134-138.
77. G. M. Brown and L. Maya, *Journal of the American Ceramic Society*, 1988, **71**, 78-82.
78. D. V. Baxter, M. H. Chisholm, G. J. Gama, V. F. DiStasi, A. L. Hector and I. P. Parkin, *Chemistry of materials*, 1996, **8**, 1222-1228.
79. J. L. Mohanan, I. U. Arachchige and S. L. Brock, *Science*, 2005, **307**, 397-400.

80. B. Mazumder, P. Chirico and A. L. Hector, *Inorganic Chemistry*, 2008, **47**, 9684-9690.
81. S. I. U. Shah, A. L. Hector, X. Li and J. R. Owen, *Journal of Materials Chemistry A*, 2015, **3**, 3612-3619.
82. D. C. Bradley and I. M. Thomas, *Journal of the Chemical Society (Resumed)*, 1960, 3857-3861.
83. A. W. Jackson and A. L. Hector, *Solid-State Chemistry of Inorganic Materials V*, 2005, **848**, 63-67.
84. A. Haaland, K. Rypdal, H. Volden and R. Andersen, *Journal of the Chemical Society, Dalton Transactions*, 1992, **1992**, 891-895.
85. B. M. Gray, A. L. Hector, W. Levason, G. Reid, M. Webster, W. Zhang and M. Jura, *Polyhedron*, 2010, **29**, 1630-1638.
86. S. Hassan, A. L. Hector, J. R. Hyde, A. Kalaji and D. C. Smith, *Chemical Communications*, 2008, 5304-5306.
87. T. Deeleard, A. Buranawong, A. Choeysuppaket, N. Witit-anun, S. Chaiyakun and P. Limsuwan, *Procedia Engineering*, 2012, **32**, 1000-1005.
88. U. M. Patil, S. B. Kulkarni, V. S. Jamadade and C. D. Lokhande, *Journal of Alloys and Compounds*, 2011, **509**, 1677-1682.
89. C. F. Mallinson, B. M. Gray, A. L. Hector, M. A. McLachlan and J. R. Owen, *Inorg Chem*, 2013, **52**, 9994-9999.
90. B. Mazumder and A. L. Hector, *Topics in Catalysis*, 2009, **52**, 1472-1481.
91. P. Krawiec and S. Kaskel, *Topics in Catalysis*, 2009, **52**, 1549-1558.
92. Z. Zhang, J. B. M. Goodall, D. J. Morgan, S. Brown, R. J. H. Clark, J. C. Knowles, N. J. Mordan, J. R. G. Evans, A. F. Carley, M. Bowker and J. A. Darr, *Journal of the European Ceramic Society*, 2009, **29**, 2343-2353.
93. L. Yuliati, J.-H. Yang, X. Wang, K. Maeda, T. Takata, M. Antonietti and K. Domen, *Journal of Materials Chemistry*, 2010, **20**, 4295-4298.
94. Y. Moriya, T. Takata and K. Domen, *Coordination Chemistry Reviews*, 2013, **257**, 1957-1969.
95. C. M. Fang, E. Orhan, G. A. de Wijs, H. T. Hintzen, R. A. de Groot, R. Marchand, J. Y. Saillard and G. de With, *Journal of Materials Chemistry*, 2001, **11**, 1248-1252.
96. J. Head and J. Turner, *Journal Name: Journal of Undergraduate Research; Journal Volume: 7*, 2007, 26-31.
97. Y. Paz, Z. Luo, L. Rabenberg and A. Heller, *Journal of Materials Research*, 1995, **10**, 2842-2848.
98. A. J. Bard and M. A. Fox, *Accounts of Chemical Research*, 1995, **28**, 141-145.
99. A. Ishikawa, T. Takata, J. N. Kondo, M. Hara and K. Domen, *The Journal of Physical Chemistry B*, 2004, **108**, 11049-11053.
100. M. Tabata, K. Maeda, M. Higashi, D. Lu, T. Takata, R. Abe and K. Domen, *Langmuir*, 2010, **26**, 9161-9165.
101. X. Feng, T. J. LaTempa, J. I. Basham, G. K. Mor, O. K. Varghese and C. A. Grimes, *Nano Letters*, 2010, **10**, 948-952.
102. D.-k. Kim, H. Lee, D. Kim and Y. Keun Kim, *Journal of Crystal Growth*, 2005, **283**, 404-408.
103. D. Bradley and I. Thomas, *Canadian Journal of Chemistry*, 1962, **40**, 1355-1360.
104. A. Salamat, K. Woodhead, S. I. U. Shah, A. L. Hector and P. F. McMillan, *Chemical Communications*, 2014, **50**, 10041-10044.

105. J. C. F. Windisch, J. W. Virden, S. H. Elder, J. Liu and M. H. Engelhard, *Journal of the Electrochemical Society*, 1998, **145**, 1211-1218.
106. K. H. Reiman, K. M. Brace, T. J. Gordon-Smith, I. Nandhakumar, G. S. Attard and J. R. Owen, *Electrochemistry Communications*, 2006, **8**, 517-522.
107. C. D. E. Lakeman and D. A. Payne, *Materials Chemistry and Physics*, 1994, **38**, 19.
108. H. Y. Lee and J. B. Goodenough, *Journal of Solid State Chemistry*, 1999, **148**, 4.
109. T. Elangovan, P. Kuppusami, R. Thirumurugesan, V. Ganesan, E. Mohandas and D. Mangalaraj, *Materials Science and Engineering: B*, 2010, **167**, 17-25.
110. F. Gillot, J. Oro-Sole and M. R. Palacin, *Journal of Materials Chemistry*, 2011, **21**, 9997-10002.
111. M. D. Lyutaya and A.B.Goncharuk, *Soviet Powder Metallurgy and Metal Ceramics*, 1997, **16**, 4.
112. K. Naoi and P. Simon, *Interface*, 2008, **17**, 34.
113. R. N. Reddy and R. G. Reddy, *Journal of Power Sources*, 2004, **132**, 315-320.
114. R. N. Reddy and R. G. Reddy, *Journal of Power Sources*, 2006, **156**, 700-704.
115. SAFC, Molecular sieves product information, Accessed 26/03/2014.
116. R. C. Weast, D. R. Lide and M. J. Astle, *CRC Handbook of Chemistry and Physics: 1989-1990 ; a Ready-reference Book of Chemical and Physical Data*, CRC Press, 1989.
117. F. Cheng, C. He, D. Shu, H. Chen, J. Zhang, S. Tang and D. E. Finlow, *Materials Chemistry and Physics*, 2011.
118. V. D. Patake and C. D. Lokhande, *Applied Surface Science*, 2008, **254**, 2820-2824.
119. C. Robertson, R. Beanland, S. A. Boden, A. L. Hector, R. J. Kashtiban, J. Sloan, D. C. Smith and A. Walcarius, *Physical Chemistry Chemical Physics*, 2015, **17**, 4763-4770.
120. M. C. Biesinger, L. W. M. Lau, A. R. Gerson and R. S. C. Smart, *Applied Surface Science*, 2010, **257**, 887-898.
121. C. N. Kirchner, K. H. Hallmeier, R. Szargan, T. Raschke, C. Radehaus and G. Wittstock, *Electroanalysis*, 2007, **19**, 1023-1031.
122. A. Trenczek-Zajac, M. Radecka, K. Zakrzewska, A. Brudnik, E. Kusior, S. Bourgeois, M. C. M. de Lucas and L. Imhoff, *Journal of Power Sources*, 2009, **194**, 93-103.
123. F. N., *CasaXPS Manual 2.3.15 Spectroscopy*, Casa Software Ltd, 2009.
124. G. P. Williams, *X-ray Data Booklet*, 2009.
125. C. Zhang, Y. Xie, M. Zhao, A. E. Pentecost, Z. Ling, J. Wang, D. Long, L. Ling and W. Qiao, *ACS Applied Materials & Interfaces*, 2014, **6**, 9751-9759.
126. A. Morel, S. Bouhtiyya, J.-F. Pierson, T. Brousse and D. Bélanger, in *Meeting Abstracts*, The Electrochemical Society, 2014, pp. 2247-2247.
127. A. Morel, T. Brousse and D. Bélanger, in *Meeting Abstracts*, The Electrochemical Society, 2014, pp. 198-198.
128. R. Lucio-Porto, S. Bouhtiyya, J. F. Pierson, A. Morel, F. Capon, P. Boulet and T. Brousse, *Electrochim. Acta*, 2014, **141**, 203-211.
129. G. C. Tron, T. Pirali, R. A. Billington, P. L. Canonico, G. Sorba and A. A. Genazzani, *Medicinal Research Reviews*, 2008, **28**, 278-308.

Chapter 6:

130. S. Hitech, Electronic grade metal amides, http://www.sigmaaldrich.com/content/dam/sigma-aldrich/docs/Sigma-Aldrich/General_Information/safc-hitech-electronic-grade-metal-amides.pdf

Accessed 29/07/2015, 2015.
131. J. S. J. Hargreaves, *Coordination Chemistry Reviews*, 2013, **257**, 2015-2031.
132. M. J. Lacey, in *Chemistry*, University of Southampton, UoS e-prints, 2012, p. 239.